Printed RFID Humidity Sensor Tags for Flexible Smart Systems

YI FENG

Doctoral Thesis
Electronic and Computer Systems
School of Information and Communication Technology
KTH Royal Institute of Technology
Stockholm, Sweden 2015

TRITA-ICT/ECS AVH 15:03
ISSN 1653-6363
ISRN KTH/ICT/ECS/AVH-15/03-SE
ISBN 978-91-7595-474-5

KTH School of Information and
Communication Technology
SE-164 40 Stockholm-Kista
SWEDEN

Akademisk avhandling som med tillstånd av Kungl Tekniska högskolan framlägges till offentlig granskning för avläggande av teknologie doktorsexamen i Elektronik och Datorsystem fredagen den 17 april 2015 klockan 10.00 i Sal B, Electrum, Kungl Tekniska högskolan, Kista 164 40, Stockholm.

Tryck: Universitetsservice US AB

Abstract

Radio frequency identification (RFID) and sensing are two key technologies enabling the Internet of Things (IoT). Development of RFID tags augmented with sensing capabilities (RFID sensor tags) would allow a variety of new applications, leading to a new paradigm of the IoT. Chipless RFID sensor technology offers a low-cost solution by eliminating the need of an integrated circuit (IC) chip, and is hence highly desired for many applications. On the other hand, printing technologies have revolutionized the world of electronics, enabling cost-effective manufacturing of large-area and flexible electronics. By means of printing technologies, chipless RFID sensor tags could be made flexible and lightweight at a very low cost, lending themselves to the realization of ubiquitous intelligence in the IoT era.

This thesis investigated three construction methods of printable chipless RFID humidity sensor tags, with focus on the incorporation of the sensing function. In the first method, wireless sensing based on backscatter modulation was separately realized by loading an antenna with a humidity-sensing resistor. An RFID sensor tag could then be constructed by combining the wireless sensor with a chipless RFID tag. In the second method, a chipless RFID sensor tag was built up by introducing a delay line between the antenna and the resistor. Based on time-domain reflectometry (TDR), the tag encoded ID in the delay time between its structural-mode and antenna-mode scattering pulse, and performed the sensing function by modulating the amplitude of the antenna-mode pulse.

In both of the above methods, a resistive-type humidity-sensing material was required. Multi-walled carbon nanotubes (MWCNTs) presented themselves as promising candidate due to their outstanding electrical, structural and mechanical properties. MWCNTs functionalized (f-MWCNTs) by acid treatment demonstrated high sensitivity and fast response to relative humidity (RH), owing to the presence of carboxylic acid groups. The f-MWCNTs also exhibited superior mechanical flexibility, as their resistance and sensitivity remained almost stable under either tensile or compressive stress. Moreover, an inkjet printing process was developed for the f-MWCNTs starting from ink formulation to device fabrication. By applying the f-MWCNTs, a flexible humidity sensor based on backscatter modulation was thereby presented. The operating frequency range of the sensor was significantly enhanced by adjusting the parasitic capacitance in the f-MWCNTs resistor. A fully-printed time-coded chipless RFID humidity sensor tag was also demonstrated. In addition, a multi-parameter sensor based on TDR was proposed. The sensor concept was verified by theoretical analysis and circuit simulation.

In the third method, frequency-spectrum signature was utilized considering its advantages such as coding capacity, miniaturization, and immunity to noise. As signal collision problem is inherently challenging in chipless RFID sensor systems, short-range identification and sensing applications are believed to embody the core values of the chipless RFID sensor technology. Therefore a chipless RFID humidity sensor tag based on near-field inductive coupling was proposed. The tag was composed of two planar inductor-capacitor (LC) resonators, one for identification, and the other one for sensing.

Moreover, paper was proposed to serve as humidity-sensing substrate for the sensor resonator on accounts of its porous and absorptive features.

Both inkjet paper and ordinary packaging paper were studied. A commercial UV-coated packaging paper was proven to be a viable and more robust alternative to expensive inkjet paper as substrate for inkjet-printed metal conductors. The LC resonators printed on paper substrates showed excellent sensitivity and reasonable response time to humidity in terms of resonant frequency. Particularly, the resonator printed on the UV-coated packaging paper exhibited the largest sensitivity from 20% to 70% RH, demonstrating the possibilities of directly printing the sensor tag on traditional packages to realize intelligent packaging at an ultra-low cost.

Keywords: Intelligent packaging, humidity sensor, wireless sensor, chipless RFID, multi-walled carbon nanotube, inkjet printing, LC resonator, paper electronics, flexible electronics.

Acknowledgements

First and foremost, I would like to express my sincere gratitude and respect to my supervisors: Adj. Prof. Werner Zapka, Prof. Li-Rong Zheng and Dr. Qiang Chen. I am profoundly thankful to Werner, whose vast industrial experience and sound knowledge of inkjet printing technology benefitted my PhD experience considerably. I deeply appreciate his professional guidance on our project work as well as the writing of manuscripts, especially this thesis. I am heartily grateful to Li-Rong for providing me the opportunity to study in KTH and research in this intriguing and challenging field of printed electronics. His broad knowledge and prospective insights are always impressive and inspiring to me. I am also very grateful to Qiang for sharing his rich knowledge and offering valuable advice to both my research work and my personal life.

I am indebted to Dr. Julius Hållstedt for his guidance and support at the start of my PhD studies. I would also like to express my deep gratitude to Assist. Prof. Zhi-Bin Zhang who guided me into the area of carbon nanotube electronics. Zhi-Bin was my project leader and became more of a mentor and friend to me. His careful supervision and continuous encouragement enabled me to research independently at a later stage.

I would like to thank my colleagues and friends working with printed and flexible devices: Dr. Botao Shao, Dr. Yasar Amin and Dr. Zhiying Liu for sharing their knowledge and offering useful suggestions. A special acknowledgement goes to Dr. Ana Lopez Cabezas who taught me the material preparation technique and gave me great help and useful advice on material characterization. Special thanks are also given to Dr. Li Xie for her great collaboration, as well as for proofreading my thesis. Their warm friendship was an invaluable support to me during the rough time in my PhD studies. I am also very thankful to Assist. Prof. Matti Mäntysalo for his professional collaboration and all the insightful discussion we had during his stay in iPack Center as well as afterwards. My sincere appreciation is also extended to Dr. Jiantong Li for sharing his hard-earned knowledge of carbon nanotubes and proofreading part of my thesis.

I gratefully acknowledge my colleagues at Xaar, Ingo Reinhold, Wolfgang Voit and Maik Müller, as well as the former colleagues there, Matthias Müller and Jens Liebeskind for their collaboration, perceptive scientific discussion, and the nice after work get-togethers. Many thanks are due to Ingo for taking the time to proofread my thesis.

I would also like to thank all the other past and present colleagues in iPack center. Many thanks go to Dr. Fredrik Jonsson for his patient help on the programming of the humidity sensor card, to Dr. Jian Chen and Dr. Liang Rong for helping me with the generation of UWB pulses, to David S. Mendoza for teaching me how to use the PCB prototyping machine, to Dr. Zhuo Zou, Peng Wang, Qin Zhou and Jia Ma for their helpful discussion on UWB technology, to Dr. Geng Yang and Dr. Zhi Zhang for sharing their knowledge, to Jue Shen for her collaboration on sensor integration, and to Ning Ma, Dr. Huimin She, Jie Gao, Chuanying Zhai, Qiansu Wan and Awet Weldezion for their warmhearted help outside of work. I am also obliged to the administrative staff in iPack center and in the Department of Electronic Systems for their excellent management and kind assistance.

I am obliged to Prof. Ahmed Hemani for performing quality review to my thesis. My sincere thanks are also given to Prof. Donald Lupo (TUT) for taking his time to be my opponent, and to Prof. Bengt Oelmann (Mid Sweden University), Assoc. Prof. Cristina Rusu (Acreo) and Prof. Shaofang Gong (LiU) for taking their time to be committee members.

I would like to extend my sincere thanks to my friends at KTH, Terrance Burks, Dr. Benedetto Buono, Dr. Mohsin Saleemi, Yichen Zhao, Dr. Xiaodi Wang, Dr. Ying Ma, Dr. Xi Chen, Dr. Luigia Lanni, Dr. Fei Ye, especially Miao Zhang and Qin Zhou (again) for all the pleasant time we had at lunch time and after work.

Last but not least, I wish to express my heartfelt thanks to my family: to my beloved husband Yuzhe for his love, understanding and support all along, and to my lovely son, Xiaoyuan, for bringing me another dimension of happiness and fullness. I must also offer my profound gratitude to my beloved parents for their unconditional love and support.

Yi Feng
March 2015, Stockholm

List of Publications

Papers appended in this thesis:

I **Flexible UHF resistive humidity sensors based on carbon nanotubes**
Yi Feng, Ana Lopez Cabezas, Qiang Chen, Li-Rong Zheng and Zhi-Bin Zhang, *IEEE Sensors Journal*, vol. 12, no. 9, pp. 2844-2850, Sept. 2012.

II **Low-cost printed chipless RFID humidity sensor tag for intelligent packaging**
Yi Feng, Li Xie, Qiang Chen and Li-Rong Zheng, accepted for publication in *IEEE Sensors Journal*.

III **Electrical and humidity-sensing characterization of inkjet-printed multi-walled carbon nanotubes for smart packaging**
Yi Feng, Li Xie, Matti Mäntysalo, Qiang Chen and Li-Rong Zheng, *Proceedings of IEEE Sensors 2013*, pp. 1-4, Nov. 2013.

IV **Electrical performance and reliability evaluation of inkjet-printed Ag interconnections on paper substrates**
Li Xie, Matti Mäntysalo, Ana Lopez Cabezas, Yi Feng, Fredrik Jonsson and Li-Rong Zheng, *Materials Letters*, vol. 88, pp. 68-72, Dec. 2012.

V **Integration of f-MWCNT sensor and printed circuits on paper substrate**
Li Xie, Yi Feng, Matti Mäntysalo, Qiang Chen and Li-Rong Zheng, *IEEE Sensors Journal*, vol. 13, no. 10, pp. 3948-3956, Oct. 2013.

VI **Development and experimental verification of analytical models for printable interdigital capacitor sensors on paperboard**
Yi Feng, Julius Hållstedt, Qiang Chen, Yiping Huang and Li-Rong Zheng, *Proceedings of IEEE Sensors 2009*, pp. 1034-1039, Oct. 2009.

VII **Fabrication and performance evaluation of ultralow-cost inkjet-printed chipless RFID tags**
Yi Feng, Li Xie, Maik Müller, Ana Lopez Cabezas, Matti Mäntysalo, Fredrik Forsberg, Qiang Chen, Li-Rong Zheng and Werner Zapka, *Proceedings of LOPE-C 2012*, pp. 257-260, June 2012.

VIII **Design of a printable multi-functional sensor for remote monitoring**
Yi Feng, Qiang Chen and Li-Rong Zheng, *Proceedings of IEEE Sensors 2011*, pp. 675-678, Oct. 2011.

Related papers not appended in this thesis:

IX **Thermal aging of electrical conductivity in carbon nanotube/ polyaniline composite films**
Ana Lopez Cabezas, Yi Feng, Li-Rong Zheng and Zhi-Bin Zhang, *Carbon*, vol. 59, no. 9, pp. 270-277, Aug. 2013.

X **RFID antenna humidity sensor co/design for USN applications**
Yasar Amin, Yi Feng, Qiang Chen, Li-Rong Zheng and Hannu Tenhunen, *IEICE Electronics Express*, vol. 10, no. 4, pp. 20130003, 2013.

XI **System integration of smart packages using printed electronics**
Matti Mäntysalo, Li Xie, Fredrik Jonsson, Yi Feng, Ana Lopez Cabezas and Li-Rong Zheng, *Proceedings of IEEE 62st Electronic Components and Technology Conference (ECTC)*, pp. 997-1002, May. 2012.

XII **Ink-jet printed thin-film transistors with carbon nanotube channels shaped in long strip**
Jiantong Li, Tomas Unander, Ana Lopez Cabezas, Botao Shao, Zhiying Liu, Yi Feng, Esteban Bernales Forsberg, Zhi-Bin Zhang, Indrek Jõgi, Xindong Gao, Mats Boman, Li-Rong Zheng, Mikael Östling, Hans-Erik Nilsson and Shi-Li Zhang, *Journal of Applied Physics*, vol. 109, pp. 084915, Dec. 2011.

XIII **Characterization of inkjet printed coplanar waveguides for flexible electronics**
Yi Feng, Matthias Müller, Jens Liebeskind, Qiang Chen, Li-Rong Zheng, Wolfgang Schmidt and Werner Zapka, *Proceedings of Digital Fabrication 2011*, pp. 454-457, Oct. 2011.

XIV **A 180nm-CMOS ssymmetric UWB-RFID tag for real-time remote-monitored ECG-sensing**
Jue Shen, Jia Mao, Geng Yang, Li Xie, Yi Feng, Majid Nejad, Zhuo Zou, Hannu Tenhunen and Li-Rong Zheng, *Proceedings of International Joint Conference on Biomedical Engineering Systems and Technologies (BIOSTEC) 2015*, pp. 210-215, Jan. 2015

XV **Wireless interconnections for paper electronics**
Li Xie, Yi Feng, Geng Yang, Botao Shao, Qiang Chen and Li-Rong Zheng, *in manuscript.*

XVI **Water dispersible carbon nanotube/polyaniline composite: study of the morphology and electrical conductivity**

Ana Lopez Cabezas, Yi Feng, Li-Rong Zheng and Zhi-Bin Zhang, *in manuscript*.

Other conference presentations:

XVII **Applications with low-cost conductive inks**
Yi Feng, Li Xie, Botao Shao, Yasar Amin, Qiang Chen and Li-Rong Zheng, oral presentation in *Workshop - Future of Conductive Printing*, Nov. 2012.

XVIII **Inkjet printed UWB impulse-based wireless sensor for flexible electronics**
Yi Feng, Qiang Chen, Matthias Müller, Werner Zapka and Li-Rong Zheng, abstract and oral presentation in *Gigahertz Symposium*, March 2012.

XIX **Inkjet printing in system integration - Printed humidity sensor-box**
Li Xie, Matti Mäntysalo, Fredrik Jonsson, Yi Feng, Ana Lopez Cabezas and Li-Rong Zheng, abstract and oral presentation in *11th Flexible Electronics and Displays Conference (FlexTech)*, Jan. 2012.

Summary of Appended Paper and Author's Contribution

- **Paper I. Flexible UHF resistive humidity sensors based on carbon nanotubes**

  This paper investigated the resistive humidity-sensing properties of multi-walled carbon nanotubes (MWCNTs). MWCNTs functionalized by acid treatment (f-MWCNTs) exhibited excellent sensitivity and fast response towards humidity. It was found that the high sensitivity of the f-MWCNTs was attributed to the presence of carboxylic acid groups which were introduced by the acid treatment. A flexible humidity sensor based on backscatter modulation was demonstrated for ultra-high frequency (UHF) RFID applications by integrating an f-MWCNTs resistor.

  Author's contribution: The author came up with the idea, planned and performed the main parts of the experiments, analyzed the results and wrote the main parts of the manuscript.

- **Paper II. Low-cost printed chipless RFID humidity sensor tag for intelligent packaging**

  This paper presented a fully-printed chipless RFID humidity sensor tag based on near-field inductive coupling for short-range identification and humidity sensing applications. In addition, paper was proposed to serve as substrate as well as capacitive sensing material. The sensing performance of paper substrates including ordinary packaging paper was studied, demonstrating the great potential of the packaging paper for printed and flexible humidity sensor applications.

  Author's contribution: The author came up with the idea, planned and performed all the experiments, analyzed the results and wrote the main parts of the manuscript.

- **Paper III.Electrical and humidity-sensing characterization of inkjet-printed multi-walled carbon nanotubes for smart packaging**

  This paper developed an inkjet printing process of f-MWCNTs and evaluated the influence of annealing temperature on the electrical and humidity-sensing properties of printed f-MWCNTs films.

Author's contribution: The author came up with the idea, planned and performed the main parts of experiments, analyzed the results and wrote the main parts of the manuscript.

- **Paper IV. Electrical performance and reliability evaluation of inkjet-printed Ag interconnections on paper substrates**

  This paper investigated the surface morphology and electrical performance of inkjet-printed silver conductors on six different paper substrates. The electrical reliability of the printed conductors on paper substrates against environmental variation were also evaluated. Ordinary packaging paper was studied and proven to be a cheap and robust alternative to inkjet paper as substrate of printed electronics for many applications.

  Author's contribution: The author performed parts of the experiments and wrote parts of the manuscript.

- **Paper V. Integration of f-MWCNT sensor and printed circuits on paper substrate**

  This paper studied the mechanical flexibility of inkjet-printed silver conductors and f-MWCNTs-based humidity sensors on paper substrates. A paper-carried flexible heterogeneous sensor system, consisting of silicon-based and printed electronics, was demonstrated for intelligent packaging.

  Author's contribution: The author participated in the idea initialization, prepared the sensor samples, performed the main parts of the measurements including SEM characterization, and wrote parts of the manuscript.

- **Paper VI. Development and experimental verification of analytical models for printable interdigital capacitor sensors on paperboard**

  This paper reviewed the existing analytical models of interdigital capacitors (IDCs), and adapted two promising models for evaluating printed IDCs on paper substrates; one model was proposed by Gevorgian et al., and another by Igrejia et al.. In the modification, paper substrates were treated as non-infinite thick, and the printed metal thickness was also taken into consideration. The modified Gevorgian model provided a closer estimation of the capacitance to the experimental data.

  Author's contribution: The author came up with the idea, developed the analytical models, planned and performed all the experiments, analyzed the results and wrote the manuscript.

- **Paper VII. Fabrication and performance evaluation of ultralow-cost inkjet-printed chipless RFID tags**

  This paper evaluated the performances of inkjet-printed chipless RFID tags based on inductor-capacitor resonators. A sandwiching process was proposed for the tag fabrication to match the cost-effective roll-to-roll processing. Two

detection methods using one antenna and two antennas, respectively, were also established and compared.

Author's contribution: The author participated in the idea initialization, planned the experiments, prepared the sandwich-structured tag samples, analyzed the results and wrote the main parts of the manuscript.

- **Paper VIII. Design of a printable multi-functional sensor for remote monitoring**

  This paper proposed a printable wireless sensor design based on time-domain reflectometry for monitoring multiple parameters at the same time. The sensor was theoretically analyzed, and an algorithm for processing the received data was introduced and verified by circuit simulation. An inkjet-printed sensor prototype was presented to prove the design concept.

  Author's contribution: The author came up with the idea, planned and performed all the work of simulation, theoretical calculation and experiments, and wrote the manuscript.

List of Abbreviations and Acronyms

ADS	Advanced Design System
CIJ	Continuous Inkjet Printing
CNT	Carbon Nanotube
CWP	Coplanar Waveguide
DC	Direct Current
DGA	Derivative Thermogravimetic Analysis
DOD	Drop-On-Demand
EG	Ethylene Glycol
EM	Electromagnetic
f-MWCNT	Functionalized Multi-Walled Carbon Nanotube
FTIR	Fourier Transform Infrared Spectroscopy
HF	High Frequency
HRSEM	High Resolution Scanning Electron Microscopy
FET	Field Effect Transistor
IC	Integrated Circuits
ID	Identification
IDC	Interdigital Capacitor
IDE	Interdigital Electrode
IDT	Interdigital Transducer
LF	Low Frequency
IoT	Internet of Things
IP	Intelligent Packaging
LC	Inductor-Capacitor
MWCNT	Multi-Walled Carbon Nanotube
PCB	Printed Circuit Board
PE	Polyethylene
PET	Polyethylene Terephthalate
PI	Polyimide
PPE	Polyphenylene Ether
RE	Rectangular Electrode
RFID	Radio Frequency Identification
RH	Relative Humidity
R2R	Roll-to-Roll
SAW	Surface Acoustic Wave
SMD	Surface Mount Device

SWCNT	Single-Walled Carbon Nanotube
TDR	Time Domain Reflectometry
TGA	Thermogravimetic Analysis
UHF	Ultra-High Frequency
UV	Ultraviolet
VNA	Vector Network Analyzer
UWB	Ultra-Wide Band

Contents

Chapter 1

Introduction

1.1 Background

With the advance of information and communication technology, our society is entering the Internet of Things (IoT) era: a world of interconnected objects that are capable of making sense of their local situations and interacting with each other as well as human users [1,2], as illustrated in Fig. 1.1. These objects, termed as smart objects, range from wearable devices, to home appliances, medical equipment, automobiles, and manufacturing equipment [3,4]. The potential applications enabled by the IoT cover transportation and logistics, medical and healthcare, smart environment, personal and social domains. These applications will not only bring convenience and economies to private users as well as business users, but also have huge impact on both personal lifestyle and business models [1].

Intelligent packaging (IP) is an important application field of the IoT [5]. Package innovation is constantly driven by stricter requirements on product quality and safety as well as greater demands for worldwide, efficient and cost-effective distribution [6]. Since the beginning of the current century, intensive innovation activ-

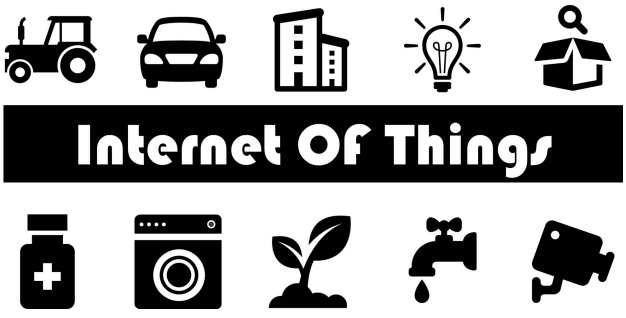

Figure 1.1: The vision of an era of Internet of Things.

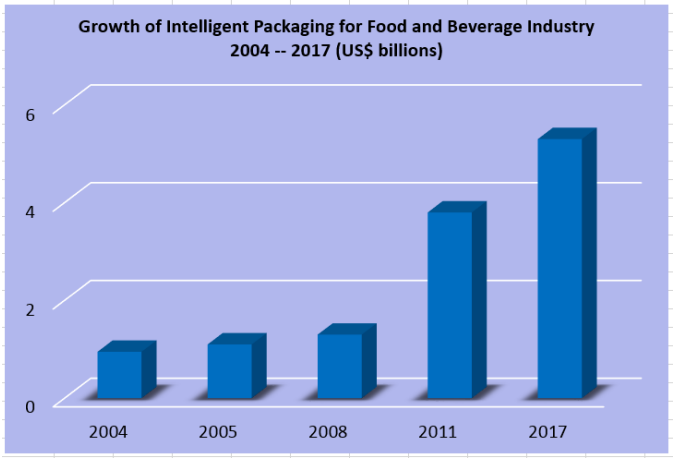

Figure 1.2: Growth of intelligent packaging for the food and beverage industry 2004-2017 [8, 9].

ities have been devoted to the development of IP, aiming to improve and extend traditional packaging functionalities by adding capabilities of sensing, recording, tracing and communicating the conditions of the packed product or its environment throughout the whole supply chain. The employment of IP will facilitate decision-making and action-taking to enhance the product quality/safety as well as the management convenience [7].

The application market for the IP technology includes food, beverages, pharmaceutical, beauty and other segments. Currently, food and beverages hold the largest market share due to their vulnerability to environmental changes and microbial attack [8]. The global market for IP for the food and beverage industry has experienced significant growth during the past decade. As shown in Fig. 1.2, the market sales of IP have risen from $1 billion in 2004 to nearly $3.8 billion in 2011, and are expected to reach $5.3 billion 2017 [8, 9]. The pharmaceuticals nevertheless are anticipated to be the fastest growing market for IP through 2017 due to the increased aging population and prevalence of chronic diseases and infectious diseases [10].

As indispensable building blocks of the IoT, the smart objects are mostly realized by embedding electronic systems [11]. The embedded systems must be light-weight and mechanically flexible in order to bestow intelligence on everyday objects, for example, the aforementioned packages, furniture, paper documents and human bodies [12–15]. Moreover, considering the huge number of the connected objects, the embedded systems have to be of low cost and low environmental impact [11]. Printed electronics are considered as a revolutionary technology to enable the cost-effective manufacturing of such flexible electronics systems [16]. In addition, the use of printed electronics will ease the integration of electronic systems onto the

Table 1.1: Typical parameters of the main printing technologies [26–28]

Parameters	Gravure	Offset	Flexo	Screen	Inkjet	Aerosol-jet
Lateral Resolution (μm)	>20	>20	>30	>100	>20	>10
Max print speed (m/s)	15	15	8	1	0.5	0.1
Wet film thickness (μm)	0.1-5	0.5-2	0.5-8	3-25	0.3-20	0.1-2
Ink viscosity (Pa·s)	0.01-0.2	30-100	0.05-0.5	1-100	0.001-0.04	0.001-1
Process postion	Contact	Contact	Contact	Contact	Non-contact	Non-contact

objects if the electronics can be directly printed onto the objects [17, 18].

Printing technologies were originally invented and developed for producing images and text on paper or other substrates. Nowadays, they are adopted as low-cost, high-volume and high-throughput processes to manufacture a variety of electronic devices on flexible substrates, such as diodes, transistors, displays, batteries, organic photovoltaics, antennas, and sensors [19–25]. Nearly all the industrial printing equipment have been employed for printed electronics, including gravure, offset, flexography, screen, inkjet, and aerosol-jet printing. Typical process parameters of these printing technologies are listed in Table 1.1 [26–28]. Each printing technology has its advantages and disadvantages which need to be weighted when deciding on the most suitable processing technique for a specific application.

1.2 Motivation and Challenges

The embedded systems in the smart objects are built upon one or several technologies, including radio frequency identification (RFID), sensors, actuators, memory, displays, energy harvesting and so on [11]. RFID and sensors are two key enablers to the IoT [29, 30]. RFID tags store and transmit the identity of the object for automatical identifying and tracking using electromagnetic (EM) fields. Sensors detect the status of the object or its surroundings and provide a corresponding output, generally as an electrical signal. Recently, the integration of RFID and sensor technologies has gained intensive attention in both academia and industry as it will open up a broad range of new applications and create more business opportunities [29–31]. Taking the IP application as an example, the acceptance of IP by product/service suppliers is still an issue that limits the diffusion of IP, especially in the European market [32]. The food suppliers, for instance, are not willing to introduce a system that could inform the customers that their products are not fresh [17]. Thus incorporating sensing function into RFID tags is particularly at-

tractive to the suppliers as they will benefit from the convenient and efficient control of the product quality through all the supply chain [17, 18].

On the other hand, humidity measurement plays an important role in agriculture, horticulture, industrial process control, environmental control and many other fields [33]. Humidity monitoring is also vital for the IP application, because the effect of humidity causes degradation to many products, like food and pharmaceuticals [34]. Identification and humidity monitoring of consumer products, especially low-value commodity products, require inexpensive RFID sensors tags.

Based on the above considerations, this thesis aims to explore low-cost, printable and flexible RFID humidity sensor solutions. The main challenges reside in three aspects. Firstly, conventional humidity sensing materials cannot fulfil all the requirements of the new applications. New sensing materials are requested. They should not only be highly sensitive, stable and reliable, but also be inexpensive and flexible. They should also be low-temperature processable due to the low heat resistance of most flexible substrates (mainly plastics and paper) [35]. Secondly, considering the costly manufacturing, testing and assembling of silicon-based RFID chips, printable chipless RFID encoding techniques are favored by many applications as they enable the tag fabrication at a very low cost [36]. The incorporation methods of the sensing function to the chipless RFID tags need to be investigated. Thirdly, the use of new manufacturing technologies, the printing technologies, would present challenges in the device fabrication such as ink formulation and choice of substrates. Inkjet printing has gained enormous attention on account of additive, mask-less, non-contact features. The direct writing process of inkjet printing also facilitates rapid prototyping and design optimization [37]. Therefore, this thesis employed inkjet printing as the main fabrication technique.

1.3 Thesis Contribution and Organization

This thesis studied three construction methods of fully-printable RFID humidity sensor tags, and provided multidisciplinary research results covering material characterization, development and evaluation of inkjet printing technique, RF design and optimization.

Backscatter modulation and time-domain reflectometry (TDR) were utilized to realize wireless sensing in the first two construction methods, respectively. Both methods involved impedance mismatch and hence required a resistive-type sensing material. Multi-walled carbon nanotubes (MWCNTs) were studied as promising candidate considering their outstanding properties. Firstly, it was demonstrated that MWCNTs functionalized through acid treatment (f-MWCNTs) possess significant sensitivity and rapid response to humidity, as well as superior mechanical flexibility. Comparative studies with untreated MWCNTs revealed that the humidity sensitivity of the f-MWCNTs was mainly attributed to the attached carboxylic acid groups introduced by the acid treatment.

Then an inkjet printing process was developed to fabricate thin films of a random f-MWCNTs network on flexible substrates. The post-printing annealing temperature was also studied regarding its influence on the conducting and sensing properties of printed f-MWCNTs.

A flexible humidity sensor based on backscatter modulation was demonstrated by integrating an f-MWCNTs resistor. It was further found that the parasitic capacitance between the electrodes of the f-MWCNTs resistor played a key role in the sensor response. The operating frequency range of the sensor was broadened up till 2 GHz by optimizing the electrode design, making the sensor suitable for ultra-high frequency (UHF) RFID application.

A printed and flexible time-coded RFID humidity sensor tag was also demonstrated by applying the f-MWCNTs. In addition, a TDR-based sensor design was proposed for monitoring multiple parameters simultaneously. The sensor was theoretically analyzed and verified by circuit simulation.

As the third construction method, a chipless RFID sensor tag based on inductor-capacitor (LC) resonators was presented for short-range identification and humidity monitoring applications. The tag utilized frequency-spectrum signature for both ID encoding and humidity sensing, providing several advantages including coding capacity, compact size, and immunity to noise and process variation. Moreover, paper, particularly ordinary packaging paper, was proposed to serve as humidity-sensing substrate for this sensor tag.

It was found that the commercial ultraviolet (UV)-coated packaging paper could readily be a cheaper and more robust substitute for inkjet paper in printed electronics. Printed metal conductors on the packaging paper exhibited not only comparable electrical performance to those on the inkjet paper, but also higher resistance to harsh environmental conditions. Moreover, it was demonstrated that paper substrates were highly sensitive to humidity, and the packaging paper exhibited the highest sensitivity over the relative humidity (RH) range from 20% to 70%. These results validated the possibility of directly printing the sensor tag on ordinary packages to make them intelligent at an ultra low cost. Furthermore, the mechanical flexibility of printed conductors on paper substrates was evaluated to provide guidance to the use of paper-carried electronics on non-flat surfaces.

It also needs to be mentioned that an analytical model of interdigital capacitance (IDC) was developed in this thesis to enable a fast and accurate estimation of the capacitance between interdigital electrodes (IDEs). IDEs are favored electrode geometries by sensor applications, and therefore were applied in the aforementioned sensor (tag) implementation. Design optimization of the sensor based on backscatter modulation was conducted with the help of the analytical model.

The rest of the thesis is organized as follows. Chapter 2 discusses the humidity-sensing materials. Humidity sensors and conventional electronic sensing materials are briefly discussed first. Following a short introduction of carbon nanotubes, the sensing properties and mechanism of the f-MWCNTs are discussed. The use of paper as humidity-sensing substrate are discussed at last.

Chapter 3 concerns the fabrication process. Inkjet printing technology is introduced first. Then the fabrication processes of the f-MWCNTs films by spray-coating and inkjet printing are described respectively, with emphasis on the latter. After that, the electrical performance and reliability of inkjet-printed metal conductors on paper substrates are discussed. The mechanical flexibility of the f-MWCNTs and the paper-carried metal conductors are also discussed respectively in this chapter.

Chapter 4 discusses the construction methods of RFID sensor tags. The existing RFID tag technologies are reviewed first. The chip-based RFID sensor solutions are then briefly introduced. After that, three construction methods of chipless RFID sensor humidity tags, together with the implemented sensors (tags), are discussed.

Chapter 5 summarizes the thesis and suggests the future work.

Chapter 2

Sensing Materials for Printed Humidity Sensors

Printable and flexible materials with excellent humidity-sensitivity are essential to building up printed RFID humidity sensor tags. In this chapter, two types of humidity-sensitive materials are presented. Multi-walled carbon nanotubes are suitable for resistive-type humidity sensor, whereas paper can be used as capacitive-type humidity-sensing material as well as printing substrate. The discussion refers to Papers I and II.

2.1 Introduction

Humidity measurements can be divided into three categories: dew point, absolute humidity and relative humidity (RH) [33]. Dew point is the temperature at which the water vapor in air begins to condense into liquid, a good indictor of the comfort level of the environment. Absolute humidity refers to the amount of water vapor in a unit volume of air, while RH, expressed as a percentage, refers to the ratio of the partial pressure of water vapor in an air-water mixture to the saturated pressure of water vapor at a given temperature. RH is a relative measurement, dependent on temperature as well as pressure of the vapor system; nevertheless, it is the most commonly used measure of humidity in daily life [33].

Based on their transduction principles, humidity sensors can be classified into different types such as resistive, capacitive, colorimetric and gravimetric [38–41]. Among these are the resistive and capacitive-type humidity sensors the most popular ones owing to their simple structure, low cost, adaptability to different types of circuits, ease of fabrication and miniaturization [42]. Resistive-type humidity sensors rely on the change in electrical resistance of a hygroscopic medium, and usually have good interchangeability and are cheaper to be manufactured than the capacitive-type sensors [43]. Capacitive-type humidity sensors are based on the dielectric change of an insulating medium, and their advantages include low power

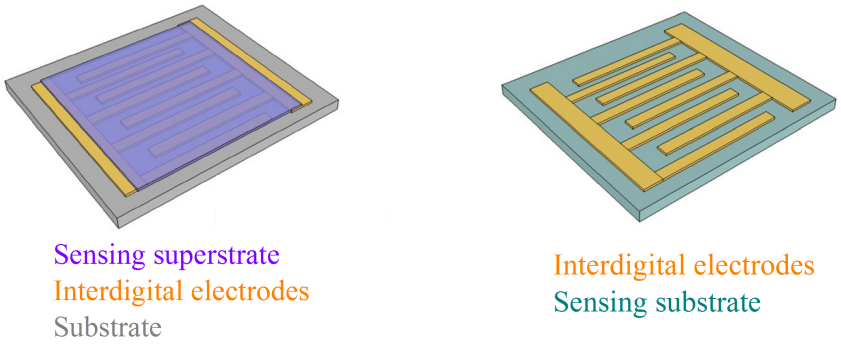

(a) (b)

Figure 2.1: Typical resistive or capacitive-type sensor layouts in a multi-layer structure where (a) a sensing material is deposited above the electrodes, (b) the substrate serves as sensing material.

consumption, linear response and operation over a wide RH range [39]. Both of them are commonly built up in a multi-layer structure, and thus favourable for printed and flexible sensors. One common approach is to print a sensing material above the electrodes which have been prepared on a substrate, and another possible approach is to directly use the substrate as sensing material, as illustrated in Fig. 2.1a and 2.1b respectively [44]. The comb-like interdigital electrodes (IDEs) in Fig. 2.1 are the most frequently used electrode geometries in sensor applications, because they provide a large contact area between ambient vapor and the sensing material, and thereby enable a fast response [45].

Conventional sensing materials for resistive or capacitive-type humidity sensors include oxide ceramics, polymers and polyelectrolytes [33]. Oxide ceramics and polymers can be used as either resistors or capacitors depending on their properties, while polyelectrolytes are mainly used for resistive-type sensors. Oxide ceramics offer advantages such as mechanical strength, stability, resistance to chemical attack, but they are rigid and require high processing temperature [38,42]. Flexible and low-cost polymers are good candidates for printed sensors, but they have several drawbacks like long-term drift, poor thermal stability and chemical stability [33, 46]. Polyelectrolytes are not stable at high humidity due to their solubility in water [47]. Carbon nanotubes (CNTs) have great potential for sensor applications including printed and flexible sensors, owing to their exceptional properties [48]. Section 2.2 will begin with a brief introduction of CNTs. Then functionalized multi-walled carbon nanotubes (f-MWCNTs) as promising resistive-type sensing material for printed humidity sensors will be discussed regarding their sensing performance and mechanism. Recently paper substrates are considered as cheap

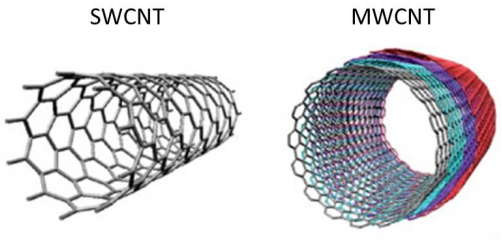

Figure 2.2: Molecular structure representatives of a SWCNT and a MWCNT. Figure adapted from [58].

and environmentally-friendly alternative to plastics in printed electronics. The hydroscopicity and porosity of paper lend itself to serving as highly sensitive substrate to humidity. Section 2.3 will first introduce the use of paper substrates in printed electronics. Then the sensing mechanism and performance of paper substrates will be discussed.

2.2 Multi-walled Carbon Nanotubes

2.2.1 Carbon Nanotubes for Sensor Applications

Carbon nanotubes (CNTs) are long seamless cylinders rolled up from a graphene sheet which is a single layer of carbon atoms in the form of a hexagonal honeycomb [49]. As shown in Fig. 2.2, single-walled carbon nanotubes (SWCNTs) are one cylindrical tube, while multi-walled carbon nanotubes (MWCNTs) consist of several concentric cylinders. Since being discovered by Iijima in the early 90s of the twentieth century, this quasi one-dimensional form of carbon has shown great promise for a wide variety of applications due to its unique structural properties, superior mechanical strength, high electrical conductivity, thermal and chemical stability [49–51]. For example, MWCNTs have a high aspect ratio (i.e. length to diameter) with diameter typically from 5 to 20 nm and length from less than 100 nm to several centimeters [49]. A Young′s modulus ranged from 270 to 950 GPa was obtained for the outmost layer of individual MWCNTs and a tensile strength of 100 GPa was attained for individual MWCNTs [52, 53]. The thermal conductivity of individual MWCNTs is more than 3000 W/(mK) at room temperature, and the phonon mean free path is around 500 nm [54]. MWCNTs can also carry large current of 10^9 to 10^{10} A/cm^2, and remain stable in air at temperatures up to 250 °C for two weeks [49, 55]. Along with these remarkable properties, the very large surface area-to-volume ratio of CNTs has prompted extensive research into the development of CNT-based sensors, including chemical, biological, and electromechanical sensors [48, 56, 57].

The development of CNT-based chemical sensors for detecting gases and vapors

is an active research area. Different types of CNT-based sensors using electronic transduction principle have been explored, including ionization sensors, capacitors, resistors and field effect transistors (FETs) [59]. Among these types are resistors and FETs the most commonly-used forms. CNT-based FET sensors focus on SWCNTs as they can be either semiconducting or metallic depending on their chirality, namely, the orientation of the graphene lattice with respect to the tube axis. MWCNTs are typically metallic and hence mostly applied as resistors or ionization sensors [49, 60]. Numerous studies have demonstrated that CNTs are sensitive to a large number of gas- and vapor-phase analytes [48], for example, ammonia (NH_3), nitrogen dioxide (NO_2), hydrogen (H_2), carbon monoxide (CO), oxygen (O_2), alcohol vapor and water vapor (H_2O). The CNT-based sensors possess many advantages over the existing technologies, including high sensitivity, fast response time, ultra compact size, low power consumption, room-temperature operation, mechanical flexibility and stretchability, and manufacturability by cost-effective printing technologies [60–62].

Despite the significant research achievements, commercialization of CNT-based sensors has not been achieved yet because there are still challenges that need to be addressed [59]. First of all, devices built on individual nanotubes suffer from low yield and low device-to-device reproducibility due to the lack of reliable methods of precisely controlling the position and orientation of individual nanotube, as well as of synthesizing nanotubes having identical electronic properties [63, 64]. Constructing devices based on two-dimensional network configuration of horizontally aligned or even randomly distributed CNTs is believed to be able to ease the fabrication and minimize the device variation as the device performance is defined by the collective properties of all the CNTs in the network [59, 64]. Poor selectivity is one major disadvantage of CNT-based gas and vapor sensors [60, 62–64]. Many approaches were proposed to overcome this problem, such as polymer coating [65], functionalization of CNT sidewalls with metal/metal oxide nanoparticles or organic molecules [66–68], and diversification of metal electrodes in CNT-based FETs [69]. The common principle behind these approaches is to employ an array of differently modified CNT-based sensors and then identify the specific molecule through pattern recognition [60]. Another practical concern regarding the sensor performance is the slow recovery commonly observed in CNT-based sensors caused by the strong bonding between the nanotubes and targeted molecules [64, 70]. Possible solutions include using ultraviolet (UV) light illumination [71], embedded heaters [72] and temporal reversed bias or gate voltage in the CNTFET configuration [73, 74].

2.2.2 Functionalized MWCNTs

Pristine CNTs have extremely poor solubility in most of the common solvents due to the strong van der Waals forces [75]. The very poor solubility of pristine CNTs in either water or organic solvents makes it difficult to practically process or engineer the material for potential applications with solution-based process techniques, such as printing techniques [58, 76]. Therefore two main surface modification approaches

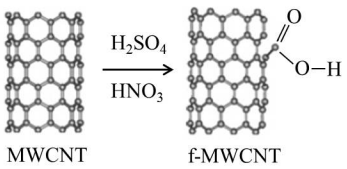

Figure 2.3: Schematic illustrating a wet chemical functionalization method with carboxylic acid groups. Figure adapted from [86].

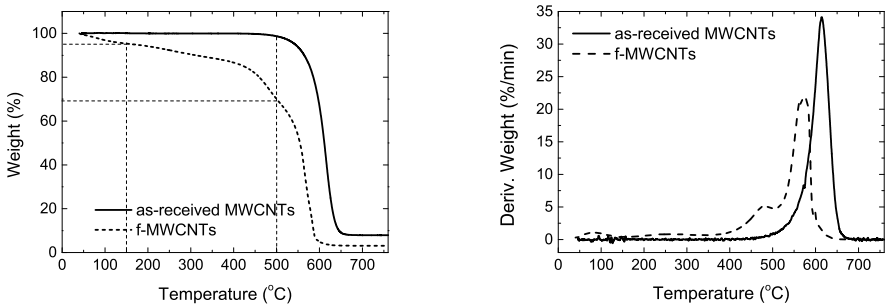

(a) (b)

Figure 2.4: (a) TGA and (b) DGA curves of as-received MWCNTs and f-MWCNTs under air atmosphere. The TGA figure adapted from Paper I.

were developed to overcome CNTs' intrinsic hydrophobic nature: non-covalent attachment of surfactant or polymer molecules [77, 78] and covalent attachment of functional groups [79]. The main advantage of the non-covalent approach is the conservation of the perfect structure of CNTs [80]. The covalent approach might affect the structural integrity of CNTs, but in turn, can tailor the properties of CNTs for specific applications [81]. Oxygen-containing groups, mainly carboxylic acid groups, are widely used as functional group. Their hydrophilicity facilitates good dispersibility of CNTs in polar solvents including water [82], and these groups can also serve as useful sites for further surface modification or functionalization [79]. The covalent attachment of the oxygen-containing groups at open ends and sidewalls of CNTs can be achieved either by wet chemical methods, photo-oxidation, oxygen plasma treatment, or gas phase treatment [83]. Among these methods, the wet chemical methods using different oxidizing acids or strong oxidants are the most popular due to their easy implementation in both laboratory and industry [84]. The oxidative treatment also purifies the as-produced CNTs by removing amorphous carbon and metallic impurities [85].

In this thesis work, the wet chemical oxidation method was employed. As shown

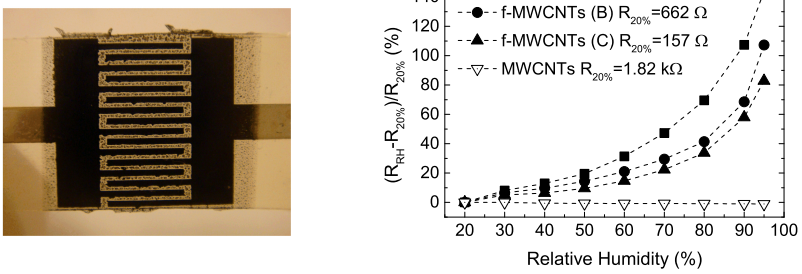

(a) (b)

Figure 2.5: (a) Photograph of a spray-coated f-MWCNTs resistor on printed IDEs on a PPE film, (b) resistance variation of three f-MWCNTs resistors and a MWCNTs resistor as a function of relative humidity at 25 °C. R_{RH} and $R_{20\%}$ denote the resistance measured at a specific RH and 20%, respectively. Figures adapted from Paper I.

in Fig. 2.3, high-purity MWCNTs (>90%) were functionalized with carboxylic acid groups (-COOH) by acid treatment: a suspension of the MWCNTs in a mixture of concentrated H_2SO_4 and HNO_3 in a 3:1 volume ratio was bath sonicated for 24 hours. The functionalized MWCNTs (f-MWCNTs) were then washed repeatedly to remove acid residues by ultracentrifugation. The collected f-MWCNTs were highly soluble in water and kept stable for a long time thanks to the attached carboxylic acid groups. The presence of carboxylic acid groups could also be inferred from the results of thermal gravimetric analysis (TGA) and derivative thermogravimetrical analysis (DGA) as shown in Fig. 2.4. The oxidization of the as-received MWCNTs started at around 500 °C, while the f-MWCNTs began to lose weight at a much lower temperature due to water desorption and decomposition of the carboxylic acid groups which happens between 150 to 500 °C [87]. In this thesis, it was found that the presence of the carboxylic acid groups was the main contributor to the significant humidity sensitivity of the f-MWCNTs through a comparative study with the as-received MWCNTs. More experimental results are given in the following section.

2.2.3 Resistive-type Sensing Properties and Mechanism

Sensing Properties

The humidity-sensing properties of a random f-MWCNTs network were characterized from f-MWCNTs-based resistors. The resistors were prepared by spray-coating the aqueous dispersion of f-MWCNTs onto printed IDEs on polyphenylene ether

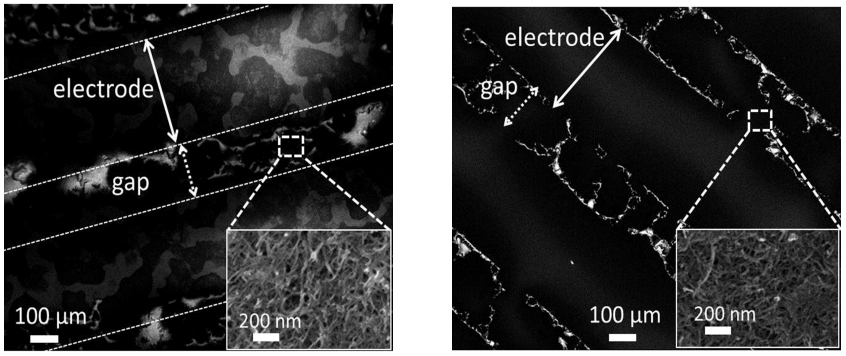

(a) (b)

Figure 2.6: HRSEM images of the spray-coated f-MWCNTs films on inkjet-printed IDEs of (a) the sample A and (b) sample C. Inset: enlarged images of the f-MWCNTs locally distributed as indicated in the corresponding samples. Figures adapted from Paper I.

(PPE) films, as shown in Fig. 2.5a. MWCNTs resistors were also prepared in the same way using the dispersion of MWCNTs in N-Methyl-2-pyrrolidone (NMP). Details of the spray-coating technique will be introduced in Chapter 3. The spraying duration could be adjusted to control the density and hence the resistance of the carbon nanotube network. Longer spraying duration leads to the formation of a denser network, resulting in a smaller resistance value. Fig. 2.5b shows the resistance variation of three f-MWCNTs resistors and a MWCNTs resistor as relative to their resistance at 20% RH as a function of relative humidity. The f-MWCNTs samples A, B and C were spray-coated for 18, 69 and 85 seconds, respectively.

All the f-MWCNTs resistors exhibited an exponentially increasing trend as the ambient humidity level was raised from 20% to 95% RH. In stark contrast, the resistance of the MWCNTs resistor was almost unchanged over the whole RH range. Moreover, it was observed that the larger resistance the f-MWCNTs resistor had at 20% RH, the higher sensitivity it exhibited to humidity. The high resolution scanning electron microscopy (HRSEM) images of the f-MWCNTs samples A and C are shown in Fig. 2.6a and 2.6b, respectively. As seen from the insets, the carbon nanotubes were randomly distributed, and the local densities of carbon nanotubes were high in both samples. However, the nanotubes did not fully cover the electrode area in the sample A, while a complete and compact film of the nanotubes was formed in the sample C. It would be simply assumed that more carbon nanotubes provide more surface area that could interact with water molecules and hence higher sensitivity. However, the above results suggest that this assumption becomes incorrect when the density of the nanotubes is high. Above a certain den-

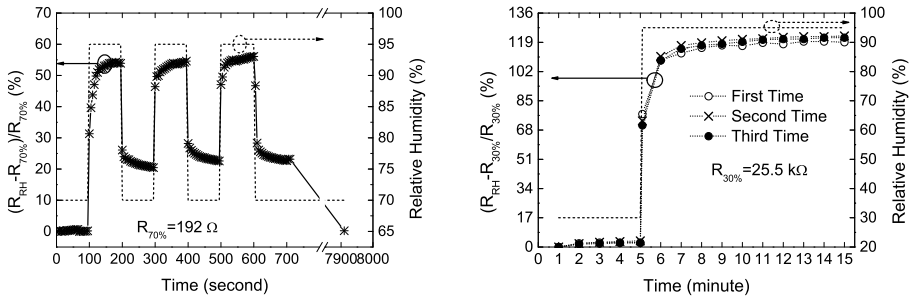

Figure 2.7: (a) Resistance variation of an f-MWCNTs resistor under dynamic cycles between 70% and 95% RH, (b) resistance variation of an f-MWCNTs resistor when the humidity level is changed from 30% to 95%RH measured three times, and the resistor was heated at 120 °C for 30 minutes before each measurement. The measurements were done at 25 °C. Figures adapted from Paper I.

sity level, the total exposed surface area would reduce when the nanotube network becomes even denser, and consequently, the humidity sensitivity of the nanotubes would decrease.

Fast response of the f-MWCNTs resistors towards moisture could be observed under a dynamic test. As shown in Fig. 2.7a, the resistor responded immediately to the rising of RH level, and the resistance reached 90% of its steady-state value at 95% RH within around 20 seconds. The resistor also responded quickly to the falling of the RH level, however, its resistance recovered only about 60% of its initial value at 70% RH within 100 seconds. Full recovery of the resistance took around 2 hours without external aid. This long recovery time indicates the reaction between the surface of carbon nanotube and water molecule is a strong chemisorption. Embedded heater is one possible and efficient solution to refresh the resistor. Although there is concern about sensor degradation induced by heating [60], the f-MWCNTs resistor showed reproducible response to the rising of RH level after being heated at 120 °C for 30 minutes for several times, as shown in Fig. 2.7b.

Sensing Mechanism

Although the humidity sensitivity of MWCNTs or MWCNTs-based composite have been observed by a few research groups [87–96], the sensing mechanism is still under debate. Among the reported works where acid-treated MWCNTs were used, several assumptions were proposed for the sensing mechanism, including the electron donation from water molecules to the p-type semiconducting MWCNTs [88, 90], the increase of tunneling barriers between the nanotube junctions due to water

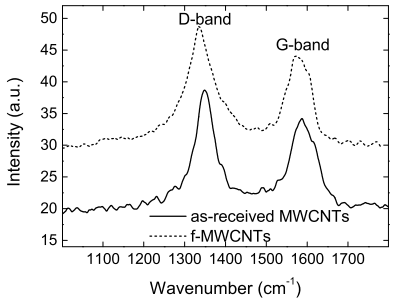

Figure 2.8: Raman spectra (514 nm) of as-received MWCNTs and f-MWCNTs. Figure adapted from Paper I.

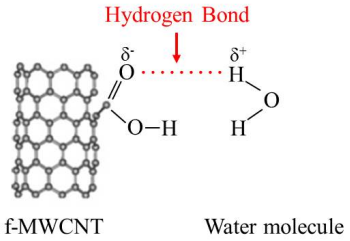

Figure 2.9: Schematic illustrating a hydrogen bond between the carboxylic acid group in the f-MWCNT and a water molecule.

absorption on the tube-to-tube interface [94, 95], the weak bonding between an H atom of water and a C atom on the nanotube surface [92, 96], and the hydrogen bonding between the polar water molecules with the oxygen-containing defects on the nanotube [87].

As seen from Fig. 2.5b, the MWCNTs and f-MWCNTs exhibited extremely different sensitivities to humidity. Therefore, the sensing mechanism of the f-MWCNTs was investigated through studying the difference between the f-MWCNTs and as-received MWCNTs.

Fig. 2.8 depicts the Raman spectra of the as-received MWCNTs and f-MWCNTs. The two peaks at around 1350 cm^{-1} and 1580 cm^{-1} are termed 'D-band' and 'G-band' respectively. The former originates from the defects on the carbon nanotubes and amorphous carbon in the material and the latter corresponds to the E2g vibrational mode of graphite [97]. Since no amorphous carbon was observed in the as-received MWCNTs according to the supplier, the intensity ratio of the 'D-band' and 'G-band' peaks basically indicates the density of defects in the material. It can be seen that both of the as-received and f-MWCNTs had a relatively high and similar density of defects. As previously discussed with Fig. 2.4, carboxylic acid

groups were present in the f-MWCNTs but not in the as-received MWCNTs. So the main difference between the the as-received and f-MWCNTs was not the density of defects, but the presence of carboxylic acid groups on the defect sites of the f-MWCNTs. Therefore, it is believed that the sensitivity of f-MWCNTs towards humidity was attributed to the hydrogen bonding between water molecules and the carboxylic acid groups on the nanotube surface as illustrated in Fig. 2.9. The hydrogen bonding reduced the hole carrier concentration in the f-MWCNTs and thus increased their resistivity. Such strong chemical absorption of water molecules also explains the long recovery time as discussed previously with Fig. 2.7a.

2.3 Paper Substrate

2.3.1 Viable Substrate for Printed Electronics

Since being invented in ancient China two thousand years ago, paper has been widely used as cheap, recyclable and flexible substrate in daily life [27]. Paper is also compatible with high-volume and high-throughput roll-to-roll (R2R) processing, and therefore considered as potential substrate for printed electronics [27, 98, 99]. There were many promising reports on electronic devices and systems fabricated on paper substrates ranging from transistors [100], batteries [101], antennas [102], to RFID tags [103], wireless sensor transmitters [104] and bio-patches [105]. Moreover, as paper is widely used as packaging material, directly printing functional devices on paper is very attractive for intelligent packaging applications because it would merge the manufacturing of electronics into conventional package production flow and thereby reduce processing steps and cost.

It is still challenging to print electronics on paper substrates because paper is comparatively rough, inhomogeneous and porous, although various coatings can be applied to adjust its surface properties [106]. Concerns about the stability and reliability of paper-carried electronics also exist due to the hygroscopic and absorptive nature of paper [107]. But on the other hand, the porous and absorptive properties of paper are advantages in some applications [27]. For example, sensors are a potential application field considering the large interfacial area of the porous paper. This thesis proposed to utilize paper substrates as humidity-sensing material. The sensing properties of paper substrates are discussed in the following section. The printing process and the electrical reliability of printed devices on paper substrates will be discussed in Chapter 3.

2.3.2 Capacitive-type Sensing Mechanism and Properties

Paper is an insulating material with a volume resistivity of 10^{10}-10^{14} Ω·cm [108]. When ambient humidity level goes up, the moisture content in paper increases as water molecules are absorbed to the hydroxyl groups of cellulose fibers of which paper is composed [27]. The dielectric constant of water is around 80 at 20 °C and one atmosphere [109], whereas that of dry paper is usually around 1.3-4 [24,27]. There-

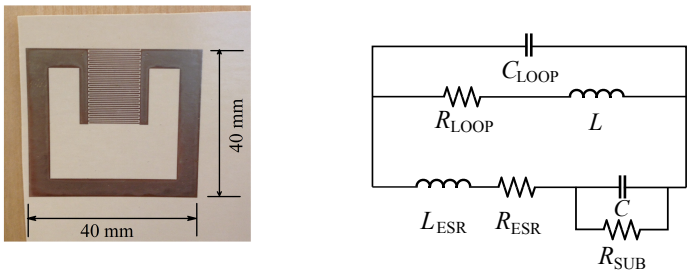

(a) (b)

Figure 2.10: (a) Photograph of a planar LC resonator printed on a paper substrate, and (b) equivalent circuit of the LC resonator. Figures adapted from Paper II.

fore, when the paper substrate absorbs more water molecules at higher humidity level, its dielectric constant would increase, making itself potential capacitive-type humidity-sensing material [110, 111].

In this thesis work, the capacitive humidity-sensing performance of paper substrates was investigated by inkjet printing a planar inductor-capacitor (LC) resonator on paper substrates as shown in Fig. 2.10a. The resonator consists of a square-shaped loop inductor and an interdigital capacitor (IDC). The equivalent circuit of the resonator is drawn in Fig. 2.10b, where L indicates the inductance of the loop, R_{LOOP} and C_{LOOP} are the parasitic resistance and capacitance in the loop, respectively, C indicates the capacitance of the IDC, R_{ESR} and L_{ESR} are the equivalent series resistance and inductance in the IDC, respectively, and R_{SUB} is the leakage resistance in the substrate between the electrodes of the IDC. Because the inductor has one turn only, C_{LOOP} between windings is much smaller than C, and then the resonant frequency, indicated by f_r, can be calculated by

$$f_{\mathrm{r}} = \frac{1}{2\pi\sqrt{(L + L_{\mathrm{ESR}})C}} \tag{2.1}$$

where C can be further calculated using an analytical model which was developed for printed IDCs on paper substrates. More detailed calculation of the capacitance C is referred to Paper VI. C increases as the dielectric constant of the paper substrate increases, and correspondingly, f_{r} decreases.

The experimental results agreed with the theory as shown in Fig. 2.11a. The detailed measurement setup will be described in Chapter 4. The resonant frequency was the frequency where the peak magnitude of the voltage reflection coefficient ΔS_{11} occurred. The resonant frequency of an LC resonator printed on a paper substrate shifted to the left as the ambient RH level increased. Meanwhile, the peak magnitude decreased as the humidity level increased, which could be explained by the decreased quality factor of the resonator. The quality factor decreased at higher humidity level partially due to the increase of the equivalent series resistance R_{ESR}

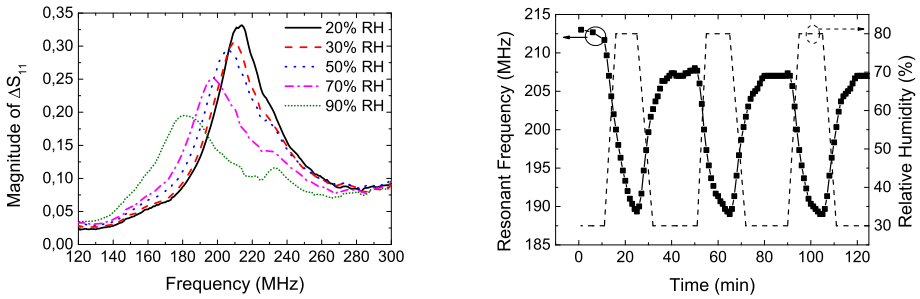

(a) (b)

Figure 2.11: (a) Measured magnitude of ΔS_{11} of an LC resonator as a function of frequency at different relative humidity levels, (b) measured resonant frequency of the LC resonator under dynamic cycles between 30% and 80% RH. The resonator was printed on a paper substrate from Printed Electronics Ltd. (PEL), and the measurements were done at 25 °C. Figures adapted from Paper II.

in the IDC. R_{ESR} is proportional to the loss tangent of the dielectric substrate which would increase when the paper absorbs more ion-containing water vapor [108, 112]. The decrease of quality factor was also attributed to the decrease of the parasitic resistance R_{SUB}. The resistivity of the paper substrate would decrease when the paper contains more moisture [108].

Fig. 2.11b shows the typical dynamic response of the LC resonator between 30% and 80% RH. The tested resonator was put in an environmental chamber. It took around 4 minutes for the humidity level in the chamber to change from 30% to 80% RH, and around 6 minutes to change back. Partially due to the long operation time of the chamber, the response time of the LC resonator was around 6 minutes. A hysteresis of 10.8% RH was observed when the humidity level was varied from 80% to 30% RH, which was caused by the formation of clusters of water molecules in the pores of paper [113]. The response time and the hysteresis can be improved by using a thinner substrate or an integrated heater [45,114]. Nevertheless, the presented sensor is sufficiently useful for environmental monitoring where the humidity changes gradually and slowly [44].

Moreover, substrate type strongly influences the sensor response. First of all, an LC resonator printed on a 200 μm-thick paper substrate showed much higher sensitivity, i.e. the variation ratio in resonant frequency (16.6%), than that printed on a 125 μm-thick polyimide (PI) substrate (2.6%) when the humidity level was increased from 20% to 90% RH. The different sensitivities mainly stem from the different water absorptive capacities of the substrates. The moisture content in the PI film is about 2.8% at 100% RH [115], while ordinary paper substrates could contain water up to 16% at 100% RH [27]. PI is often used as sensing substrate

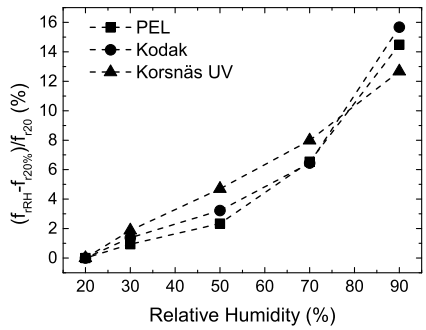

Figure 2.12: Variation of the measured resonant frequencies of three LC resonators as a function of relative humidity at 25 °C. The resonators were printed on two inkjet papers from PEL and Kodak, and a UV-coated packaging paper from Korsnäs, respectively. Figure adapted from Paper II.

in printed humidity sensors [44, 116]. This comparison result shows that paper is advantageous to humidity sensor applications considering its sensitivity.

Three paper substrates, including two inkjet papers and one UV-coated packaging paper, were also compared as shown in Fig. 2.12. The resonators printed on the two inkjet papers showed similar response. The resonator printed on the packaging paper exhibited the highest sensitivity among the three samples when the humidity level was below 70% RH but the lowest sensitivity when the humidity level exceeded 70% RH. This surprising result probably has relation to the water absorption capacity of the paper substrates. The cellulose fibers in the packaging paper might become almost saturated with water above 70% RH and hence could not absorb much more water as the inkjet papers did. Gravimetric analysis should be performed to determine the water contents of the paper substrates at different relative humidity levels. Nevertheless, the above results demonstrated the great potential of ordinary packaging paper for low-cost and flexible humidity sensor applications.

Chapter 3

Device Fabrication on Flexible Substrates

Printing technologies are considered as revolutionary and cost-effective approaches to manufacture electronic systems on flexible substrates. Inkjet printing was chosen as the main technique for device fabrication in this thesis owing to its unique features.

As introduced in the preceding chapter, f-MWCNTs and paper substrates are promising sensing materials for printed and flexible humidity sensors. The chapter begins with a short introduction of inkjet printing technology. Then thin film fabrication of f-MWCNTs by spray-coating and inkjet printing techniques will be discussed respectively with an emphasis on the latter technique. The metallization process on paper substrates using inkjet printing is also discussed. The discussion refers to Papers I, III, IV and V.

3.1 Introduction of Inkjet Printing Technology

Inkjet printing has become one of the major printing technologies used in the field of printed electronics thanks to its ability to precisely deposit picoliter volume of functional materials in liquid phase onto pre-defined area [117]. Another advantage of inkjet printing is its non-contact processing which allows easy handling of a wide variety of substrates – rigid boards, flexible thin foils, three-dimensional objects and so on [118].

There are two main inkjet printing technologies: continuous inkjet (CIJ) and drop-on-demand (DOD) inkjet [119]. In CIJ technology, a continuous stream of liquid ink is ejected out a small nozzle under pressure and individual droplets are formed via the Rayleigh instability. The droplets are variably charged as they form by holding the nozzle at an appropriate potential relative to ground. The charged droplets further pass through an electrical field and are directed to either land on the substrate, or fall into a collection gutter for recirculation. Fig. 3.1a illus-

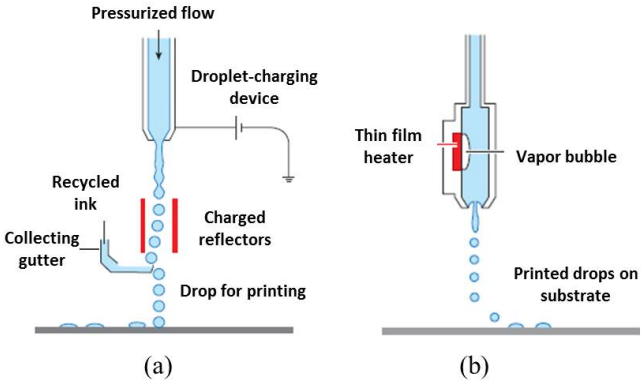

Figure 3.1: Schematic diagram of (a) a continuous inkjet printer and (b) a thermal drop-on-demand inkjet printer. Figures adapted from [119].

trates the working principle of the CIJ printing. The advantage of CIJ is speed. However, the printing resolution of CIJ is generally low and high maintenance is required [118]. Moreover, the recycling of the ink bears the risk of contamination, and hence potentially results in degraded printing performance and waste of material [119].

The DOD inkjet printing technology, where a drop of ink is only formed when it is needed, is more economical than the CIJ technology [119]. There are two dominant techniques to eject droplets on demand: thermal and piezoelectric. As illustrated in Fig. 3.1b, the thermal inkjet printers utilize a small thin-film heater in the printhead channel. The ink in immediate contact with the heater will be heated up rapidly above its boiling temperature once a current pulse is applied to the heater, creating a small vapor bubble and forcing ink droplets out of the nozzle. The piezoelectric inkjet printers utilize electromechanical actuation enabled by piezoelectric material. When an electrical field is applied, the piezoelectric material expands and contracts, expelling the ink out of the nozzle. This reverse piezoelectric effect can be used in four different ways: squeeze mode, bend mode, push mode and shear mode, as displayed in Fig. 3.2a-3.2d, respectively [120]. The squeeze mode uses a tube made of piezoelectric ceramics. The tube actuator is radially polarized and deformed to squeeze the ink out of the nozzle. In both the bend and push mode, an electric field is applied parallel to the polarization of piezoelectric ceramics, and an diaphragm is deformed to expel the ink. In contrast to these two modes, the electrical field is applied perpendicularly to the polarization of the ceramics in the shear mode. Xaar is one of pioneers in the shear-mode printhead design. The Xaar-type shear-mode printhead is illustrated in Fig. 3.2d. The applied field causes the diaphragms to flex in the middle. Such physical deformation at high frequency creates an acoustic wave in the channel and in turn forces the ink out of the nozzle.

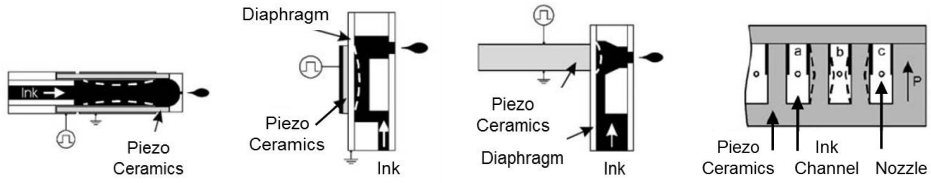

(a) (b) (c) (d)

Figure 3.2: Schematic illustrating the actuation principles of piezoelectric drop-on-demand inkjet printheads in (a) squeeze mode, (b) bend mode, (c) push mode, and (d) shear mode, respectively. Figures adapted from [120].

The shear-mode printheads consume much less power than the other three mode printheads because the coupling of electrical energy to mechanical deformation is very efficient in this mode [118].

Although the thermal printing systems are simple and cheap, the range of inks for the thermal inkjet printer is limited because the inks are in direct contact with the heater. The thermal inkjet inks must have a volatile component, and are mainly water-based. It is also difficult to control the water-based inks on the substrate due to the high surface tension of water [118]. With the piezoelectric actuation, a much wider variety of inks can be printed, and there is more freedom to develop inks with new properties and functions. Moreover, the piezoelectric printers allow more control on the drop size, shape and velocity [119].

The application of inkjet printing technology to printed electronics poses challenges in terms of ink formulation, choice of substrates and so on [121]. In general, ink properties need to be matched with the specific printer in use for a stable and reliable jetting of droplets out of the nozzles [121,122]. Viscosity and surface tension are two crucial parameters of the inks that influence the drop formation [122, 123]. The important role of these two parameters can be apprehended from the following dimensionless grouping of fluid properties. This dimensionless number is commonly used to analyze the mechanics of drop formation in the DOD printheads [124],

$$Z = \frac{\sqrt{\rho d \gamma}}{\eta} = Oh^{-1} \tag{3.1}$$

where ρ, γ and η are the density, surface tension and viscosity of the fluid respectively, and d is the characteristic length which is the nozzle diameter in this case. The Z number is the inverse of the Ohnesorge number (Oh) that describes the ratio of internal viscous dissipation to surface tension energy [125]. Fromm introduced the Z number and predicted that drop formation in DOD printing systems was only possible for $Z > 2$ [124]. Later this prediction was refined by Derby et al., summarizing that drop formation takes place in a controlled fashion in the range $1 < Z < 10$ for most commercial DOD printing systems [126]. The lower limit

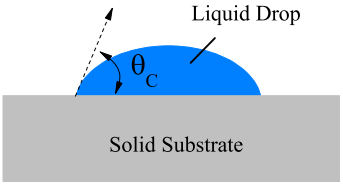

Figure 3.3: Illustration of the contact angle (θ_C) of a liquid drop on a solid substrate.

represents that the viscous dissipation dominates and a large pulse of pressure is required to break up the liquid. The upper limit represents that the surface tension forces dominate and lead to the formation of satellite droplets [117, 126]. A desktop shear-mode piezoelectric inkjet printer, Fujifilm Dimatix material printer (DMP2800 series), was used in the experiments in this thesis. Taking it as an example, it requires inks to have a viscosity of 10-12 cP and surface tension of 28-33 mN/m at jetting temperature [127]. Moreover, the inks should be stable without agglomeration, and should not dry out on the nozzle plate to avoid clogging the nozzles.

The substrate is also an important component of an inkjet system. The substrate properties must match the chosen ink for optimal print quality and functional performance. For non-permeable substrates, surface energy is a key factor which influences the wettability of an ink on a substrate [128]. Contact angles, as defined in Fig. 3.3, are commonly used to evaluate the wettability. In general, contact angles smaller than 90° indicate high wettability and high surface energy of the substrate as compared with the surface tension of the ink in use, while contact angles larger than 90° indicate low wettability and low surface energy of the substrate [129]. Typically, a small contact angle is preferred to obtain good wettability and good adhesion of an ink to a substrate [130]. Nevertheless, a large contact angle, which leads to the formation of small droplets, can be utilized to achieve high printing resolution [128]. When paper made of cellulose fibers is used as substrate, more parameters of the substrate come into play, including surface roughness, porosity, absorption rate and thermal stability [106]. Moreover, the properties of paper substrates can vary significantly depending on their structure, composition and coating technique [27]. Therefore, the choice of a suitable paper substrate must be carefully made.

3.2 Thin Film Fabrication of f-MWCNTs

3.2.1 Spray Coating of f-MWCNTs

Spray-coating is a simple and cheap technique to deposit materials in solution form and compatible with industrial R2R processes [131]. This coating technique does

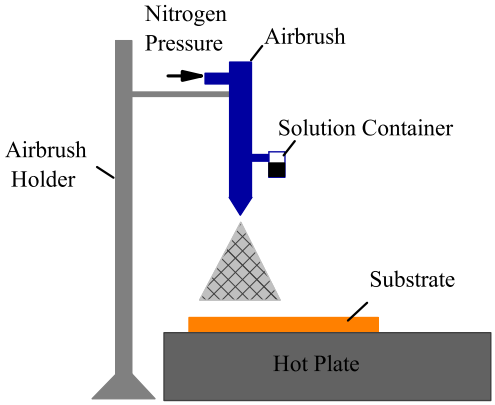

Figure 3.4: Illustration of a spray-coating setup using an airbrush.

not have strict requirements on the fluid properties, and can produce large-area, pinhole-free films with relatively uniform thickness, which makes it a good method to prepare thin-film samples for material characterization [132].

In this thesis work, spray-coating was employed to prepare the MWCNTs and f-MWCNTs resistors for material characterization. The spray-coating setup using a commercial airbrush is illustrated in Fig. 3.4. Nitrogen, working as carrier gas, brought a liquid solution of material from the container to the nozzle at the airbrush tip. The solution passed the nozzles and broke into small droplets which deposited on a substrate. The substrate was continuously heated on a hotplate in order to evaporate the solvent quickly and avoid material agglomeration. The substrate temperature, together with spraying duration and spraying distance, were optimized to obtain a homogeneous film. As mentioned in the previous chapter, the MWCNTs and f-MWCNTs resistors were formed by spray-coating the corresponding solution on printed IDEs. Different resistance values could be obtained by intentionally varying the total spraying duration for each sample. For example, the f-MWCNTs resistor samples A, B and C as shown in Fig. 2.5b were 5.16 kΩ, 662 Ω and 157 Ω at 20% RH respectively. They had the same electrode and were spray-coated for 18, 69 and 85 seconds, respectively. As seen from Fig. 2.6, a denser network and a more complete film of carbon nanotubes were formed on the electrode area of the sample C, which resulted in a smaller resistance value.

3.2.2 Inkjet Printing of f-MWCNTs

Although the spray-coating process is simple and results in relatively homogeneous films, it requires additional patterning steps and wastes considerable material on the patterning masks. Moreover, its batch-to-batch reproducibility of the f-MWCNTs resistors in terms of resistance does not meet commercialization standards. Recently, research work was performed to use inkjet printing as a cost-effective and accurately-controlled technique to deposit and pattern CNTs on various substrates for a broad range of applications, such as transparent electrodes, thin film transistors, sensors, and antennas [14, 133–137]. To obtain satisfactory patterns, three factors have to be carefully considered: (1) ink properties [138]; (2) substrate properties [139]; (3) process parameters, e.g., printing resolution and substrate temperature [140]. As compared to the latter two factors, the formulation of a stable CNT dispersion with suitable viscosity and surface tension is an essential starting point [134, 138]. Many CNT inks were prepared by attaching surfactants or polymers to improve the dispersibility of CNTs [134, 141–143]. These additives were also used to adjust the ink viscosity. However, direct electrical contact between nanotubes was prevented by the surfactants or polymers, increasing the resistance of printed CNTs films [132, 140]. To avoid adding any additive, water-dispersible CNTs functionalized by oxygen-containing groups were used for inkjet printing [133, 135, 140, 144]. The functionalization process, like the acid treatment described in Chapter 2, also cut the long nanotubes so that they would not clog the nozzles easily. Nevertheless, using water as ink solvent results in an unreliable jetting with piezoelectric inkjet printers [140,144], because water has a low viscosity of 0.89 cP, and a high surface tension of 72 mN/m at 25 °C [145,146]. Additionally, water forms a large contact angle on substrates with low surface energy, giving rise to bad wettability of the ink on such substrates [133]. For example, water forms a contact angle of 72° on an untreated PI foil (Kapton® HN, Dupont) [147]. Furthermore, inks with boiling point higher than 100 °C are usually preferred by the piezoelectric inkjet printers, otherwise they would dry out on the nozzles of the printhead quickly. Therefore, the solvent for the CNTs functionalized with oxygen-containing groups has to be carefully chosen to meet the requirements of the printer.

In this thesis work, aqueous ethylene glycol (EG) solution (99wt.% of EG) was used instead of water as solvent to formulate an f-MWCNTs ink with much improved jetting reliability. The EG was chosen as the main solvent because it has a viscosity of 16.1 cP and a surface tension of 48 mN/m at 25 °C [148]. In addition, the non-volatile nature of EG could help to keep the nozzles humectant and thereby prevent them from drying out and clogging. The f-MWCNTs dispersed well in the aqueous EG solution (0.4 mg/ml) and remained stable for several weeks and even longer. The viscosity of the formulated ink was measured to be 11.8 cP at 32 °C. The surface tension of the solvent is around 48.2 mN/m at 25 °C according to the data sheet of EG [148]. Thus the Z-number of the dispersion was estimated to be around 3. Although the surface tension of the ink was higher than the optimal

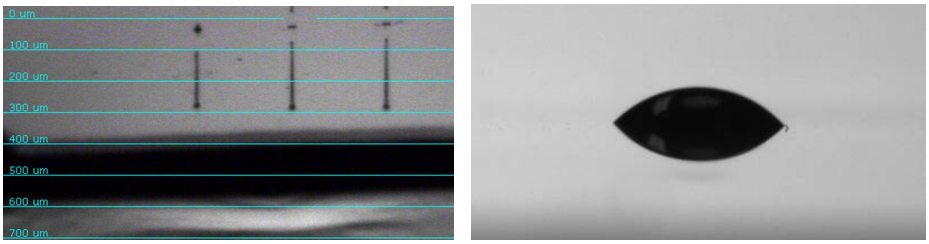

(a) (b)

Figure 3.5: (a) Droplet formation of an f-MWCNTs ink under a DMP inkjet printer, (b) contact angle measurement of the f-MWCNTs ink on untreated polyimide foil.

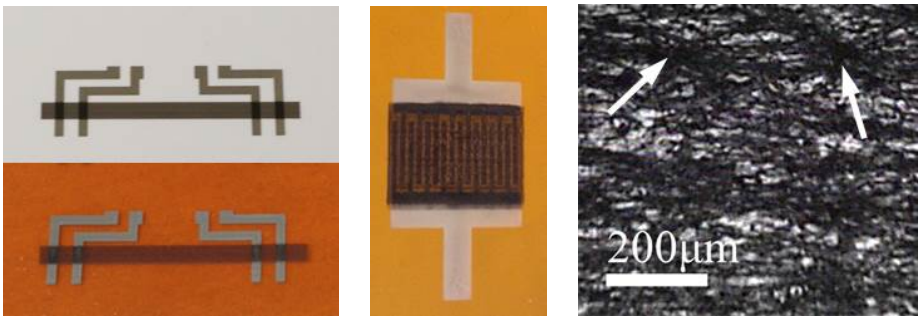

(a) (b) (c)

Figure 3.6: Photographs of (a) inkjet-printed f-MWCNTs films in the shape of strip on (upper) a paper substrate and (lower) a polyimide foil respectively, and (b) an inkjet-printed f-MWCNTs resistor on a polyimide foil. (c) Optical microscope photo of a 20-layer f-MWCNTs film inkjet-printed on a polyimide foil. Figures adapted from Paper III.

value required by the DMP printer, reliable and satellite-free jetting behavior was obtained at the expense of a lower jetting frequency of 2 kHz as seen from Fig. 3.5a. The contact angle of the ink on the untreated PI foil (Kapton® HN, Dupont) was about 45°, as shown in Fig. 3.5b.

Fig. 3.6a shows the photographs of the f-MWCNTs films in the shape of a strip which were inkjet-printed on paper and PI substrates, respectively. Fig. 3.6b shows the photograph of one f-MWCNTs resistor on PI. The resistor was formed by inkjet printing the f-MWCNTs on printed IDEs. Observing the f-MWCNTs films on PI more carefully under an optical microscope as shown in Fig. 3.6c, it can be seen that a random network of f-MWCNTs was formed, but there were some places where nanotubes accumulated, for instance, as indicated by the white arrows, prob-

ably due to the coffee-ring effect. The coffee-ring effect describes a phenomenon which commonly occurs in inkjet printing: when a colloidal droplet dries on a solid substrate, a ringlike deposit is formed along the perimeter of the droplet [149]. The solute particles tend to flow outward to the droplet edge because the solvent at the edge evaporates more quickly [150]. The coffee-ring effect was clearly observed from a microliter drop of the f-MWCNTs ink dried on a plastic substrate. It was also found that more nanotubes settled along the edge of a printed line when printing with one nozzle. The printed f-MWCNTs film on paper was more uniform than that on PI because the paper substrate absorbed the solvent immediately. The coffee-ring effect could be suppressed by optimizing the process parameters (e.g., substrate temperature) to minimize the drying flows [140], or modifying the solvent composition, for example, utilizing mixed solvents to introduce an inward Marangoni flow [149]. Nevertheless, it is worth mentioning that there was a perceptible improvement in the batch-to-batch reproducibility of the f-MWCNTs resistors using inkjet printing as compared with the resistors fabricated by spray-coating.

3.2.3 Effect of Annealing Temperature on f-MWCNTs Properties

Electrical performance

The electrical performance of inkjet-printed f-MWCNTs films was evaluated in terms of sheet resistance. Four-point probe measurement was applied to obtain accurate resistance. A typical four-point structure for resistance measurement is illustrated in Fig. 3.7a. A constant current was applied though the two outer probes, and the total resistance (R) of the tested line was obtained by measuring the voltage across the two inner probes. Contact resistance was eliminated by separating the current and voltage probes. The sheet resistance (R_S) of the tested line was then calculated by,

$$R_S = \frac{R}{L/W} \tag{3.2}$$

where L is the length and W is the width of the test line. A homemade printed circuit board (PCB)-based probing tool was employed to ensure repeatability and reliability of the measurement as shown in Fig. 3.7b and 3.7c. Spring contacts were used in the tool to guarantee good contact with all the four probes simultaneously.

The sheet resistances of printed f-MWCNTs films on a PI foil were characterized from the samples in the shape of a strip as shown in Fig. 3.6a. Fig. 3.8a shows the measured sheet resistances of three samples, overprinted for 10, 20, and 30 times, respectively, as a function of annealing temperature. As the annealing temperature was raised from 120 to 250 °C, the sheet resistances of all the samples decreased and appeared to level off gradually. It was probably because the contact gaps with the nanotubes and inter-tubes were reduced as the annealing process released the internal stress in the f-MWCNTs network [90]. It was also possibly related to the

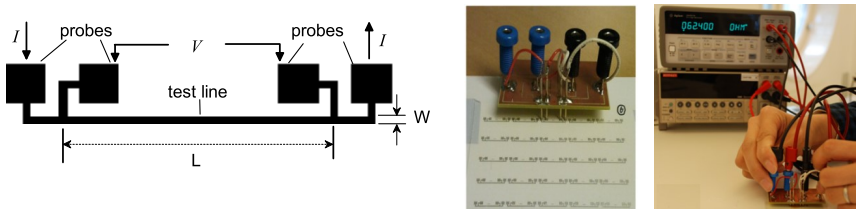

(a) (b) (c)

Figure 3.7: (a) Four-point structure for sheet resistance measurement, (b) homemade PCB-based probing tool, and (c) resistance measurement setup using the homemade probing tool.

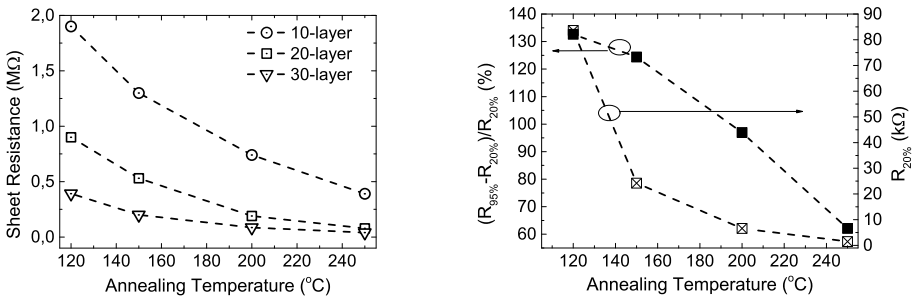

(a) (b)

Figure 3.8: (a) Sheet resistance of three f-MWCNTs strips inkjet-printed with 10, 20 and 30 layers, respectively, as a function of annealing temperature, (b) resistance of an inkjet-printed f-MWCNTs resistor measured at 20% RH and its resistance variation between 95% and 20% RH as a function of annealing temperature. Figures adapted from Paper III.

decomposition of carboxylic acid groups attached on the nanotube surface. Their decomposition occurred between 150 to 500 °C [87].

Humidity Sensitivity

The inkjet-printed f-MWCNTs resistors as shown in Fig. 3.6b were placed in an environmental chamber for humidity-sensitivity characterization. Fig. 3.8b illustrates the resistance variation of a sample relative to its resistance at 20% RH as a function of annealing temperature. The resistance measured at 20% RH is also plotted in the figure. It can be seen that the resistance variation between 20 and 95% RH, i.e. the humidity sensitivity, decreased as the annealing temperature was raised.

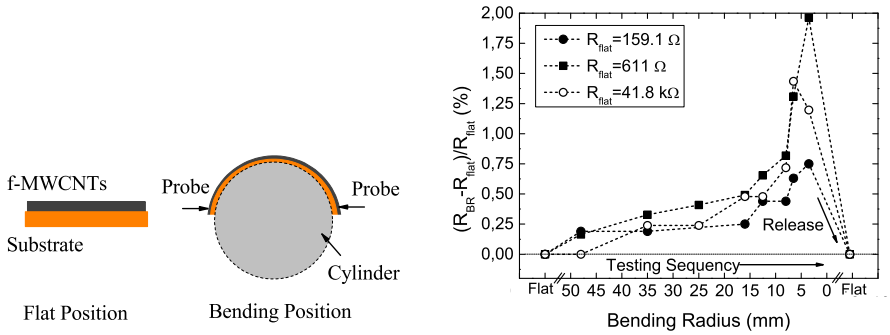

Figure 3.9: (a) Schematic illustration of the bending test setup with two-probe dc resistance measurement, (b) resistance variation of three f-MWCNTs resistors as a function of bending radius. R_{BR} and R_{flat} denote the resistance measured at one specific bending radius and when the resistor is flat before bending, respectively. Figures adapted from Paper I.

As discussed in the previous chapter, the excellent humidity-sensitivity of the f-MWCNTs was attributed to the presence of carboxylic acid groups. The reduced sensitivity was probably caused by the loss of the carboxylic acid groups at higher annealing temperature. This result suggests the maximum process temperature for the f-MWCNTs should be kept below the critical decomposition temperature of the carboxylic acid groups (150 °C) in order to retain their excellent humidity sensitivity.

3.2.4 Mechanical Flexibility Evaluation

One cycle of bending test was performed to the f-MWCNTs resistors on PPE films as illustrated in Fig. 3.9a. Tensile stress was produced in the f-MWCNTs film by placing the film facing upwards in the bending test. Fig. 3.9b depicts the resistance variation of three f-MWCNTs resistors as a function of bending radius. The bending radius was defined by the radius of the cylinder. The resistances of all the samples basically increased as the bending radius decreased. Nevertheless, the variation in resistance was still less than 2% even when the bending radius was as small as 3.5 mm, corresponding to around 1.4% strain in the nanotubes. Moreover, the resistances fully recovered to their initial values once the resistors were released from the bending.

Furthermore, the humidity sensitivity of the f-MWCNTs was barely affected by the bending as shown in Fig. 3.10, either with the f-MWCNTs film facing downward the cylinder or with the film facing upwards. The resistors were measured in three

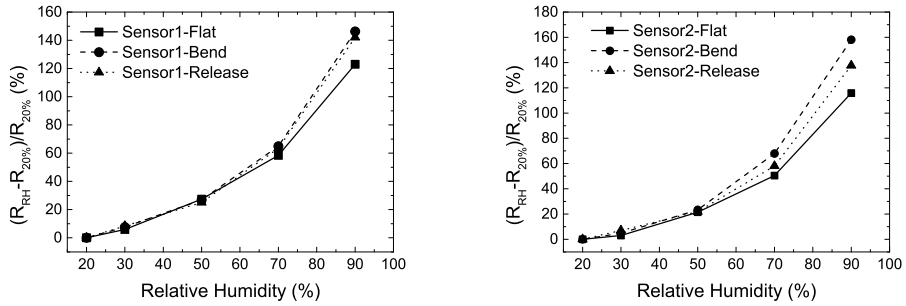

(a) (b)

Figure 3.10: Resistance variation of two f-MWCNTs resistors fabricated on a paper substrate as a function of relative humidity at 25 °C, (a) $R_{20\%}$ is 884 Ω for Sensor 1 and the bending radius is 10 mm with the f-MWCNTs film downwards facing the cylinder, (b) $R_{20\%}$ is 877 Ω for Sensor 2 and the bending radius is 20 mm with the f-MWCNTs film facing upwards. Figures adapted from Paper V.

status sequentially: flat, under bending, and released. The f-MWCNTs resistors used in this test were fabricated on a paper substrate. It has to be mentioned that the f-MWCNTs resistors fabricated on paper substrates showed less flexibility than those on PPE films. The resistance variation already reached 20% when the bending radius was 10 mm for the f-MWCNTs resistor on paper with the f-MWCNTs film facing upwards. As a matter of fact, it were not the f-MWCNTs, but the inkjet-printed electrodes on the paper substrate that limited the overall flexibility. The mechanical flexibility of inkjet-printed conductive structures on paper substrates will be discussed in detail in Section 3.3.4.

3.3 Inkjet-printed Metal Conductors on Paper Substrates

3.3.1 Silver Nanoparticle Inks and Thermal Sintering

Conductors such as electrodes, contacts and interconnections are indispensable components of electronic devices and systems. Direct writing of conductive structures by inkjet printing received great research attention. There are different types of conductive inks, mainly including conducting polymers, organometallic compounds, metal precursors and colloidal suspensions of metallic nanoparticles [151]. Conducting polymers have advantages of flexibility, low cost, ease of processability, but they are 1000 to 10000 times less conductive than the metallic inks [117]. For example, the conductivity of the polymer PEDOT:PSS is up to 1000 S/m [152]. Metallic inks are requested in applications where high conductivity ($>10^4$ S/m) is needed [153]. The organometallic compounds or metal precursors avoid risks of agglomeration

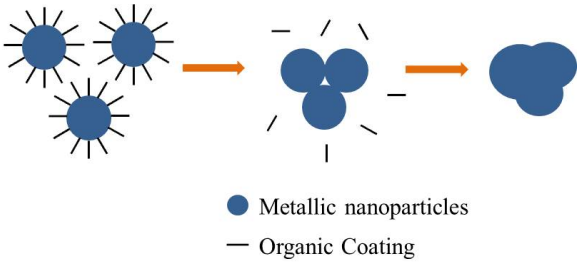

Figure 3.11: Illustration of a sintering process for metallic nanoparticle inks.

and nozzle clogging by being in the form of solution [151]. But these inks require additional thermal or chemical reduction to metallic species, and a relatively large amount of organic residues and other ionic contaminants often remain after the reduction, affecting the long-term reliability of the fabricated electronics [154]. The metal nanoparticle inks have shown the highest conductivity up to 50% of the bulk metal conductivity [155]. Moreover, when paper is used as substrate, the metal nanoparticle inks are advantageous owing to the limited penetration of the particles into the porous substrate [153]. Silver nanoparticle inks are widely used because of their high conductivity and thermal stability [123].

A sintering process is required for the printed metal nanoparticle inks to form highly conductive structures. The sintering process not only removes non-conductive organic coatings which stabilize the particles in the suspension, but also promotes the growth and coalescence of the particles [154, 156, 157], as illustrated in Fig. 3.11. The sintering step can be performed in various ways, for instance, oven sintering [155], electrical sintering [158], microwave sintering [156], chemical sintering [159, 160], or photonic sintering by means of flash, laser and other light sources [153, 161, 162]. Although the thermal sintering in an oven involves a longer sintering time than the other techniques, it is still the simplest and most reliable technique [155].

Low temperature sinterable inks are favored in printed electronics considering the low heat tolerance of most plastic and paper substrates. In this thesis work, silver nanoparticle ink (NPS-JL) from Harima Chemicals Inc. was chosen because of its low sintering temperature. According to the supplier, the recommended sintering condition is 120 to 150 °C for 1 hour. Fig. 3.12 shows the sheet resistances of inkjet-printed four-probe structures on an inkjet paper (PEL Nano P60 from Printed Electronics Ltd.) using the NPS-JL ink. Three sample groups were sintered at 100, 120 and 150 °C, respectively. The resistance decreased as the sintering temperature increased, with a significant reduction occurring from 120 to 150 °C. The optimal sintering temperature for this ink was found to be 145 °C, because the evaporation of the solvent as well as the decomposition of the organic coating mainly finished by this temperature as analyzed from TGA and Fourier transform infrared spectroscopy (FTIR) results of the ink [35].

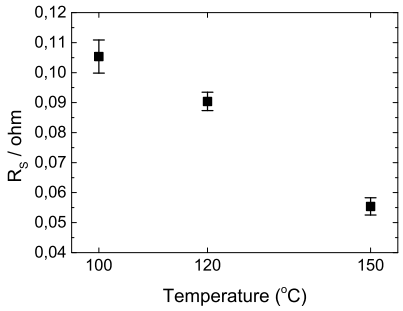

Figure 3.12: Sheet resistances of three groups of inkjet-printed four-probe structures on PEL inkjet paper which were sintered at 100, 120 and 150 °C for 1 hour, respectively. Each group includes 25 samples. Figure adapted from Paper V.

3.3.2 Influence of Paper Surface on Conductive Performance

Although paper has attracted great interest as cheap and green alternative substrate to plastics, concerns still exist regarding the conductive performance, reliability and mechanical flexibility of printed devices on paper substrates [106]. Mostly inkjet photo papers are researched on so far. They are, however, expensive and vulnerable to a harsh environment. Cheaper and more robust packaging paper offers attractive possibilities to printed electronics, particularly for intelligent packaging applications. By directly using packaging paper as substrate, the manufacturing of electronics can be merged into conventional package production flow and thereby reduce both processing steps and cost.

In this thesis work, six different commercial paper substrates were compared using the silver nanoparticle ink NPS-JL. The paper substrates were divided into two groups: inkjet paper and package paper. Three inkjet paper substrates were from Printed Electronics Ltd. (PEL), Kodak Ltd. and Felix Schoeller Group, respectively. The packaging paper substrates were provided by Korsnäs AB, including three types: UV-coated, Polyethylene (PE)-coated and clay-coated. Surface characteristics of the paper substrates strongly influence the morphologies of printed droplets and line structures on the substrate and hence the conductivity. Öhlund et al., concluded that surface roughness and porosity were the most crucial parameters of the paper substrates that influenced the electrical conductivity [106]. The pore size of the clay-coated packaging paper was so large that the nanoparticles penetrated the substrate, resulting in a dark and non-conductive pattern. Fig. 3.13 compares the sheet resistances measured from the other five paper substrates and shows their respective SEM pictures. The paper substrates were sintered at 100 °C in this experiment. The sheet resistance measurement was performed in the same way as introduced in Section 3.2.3. The printed droplets spread irregularly on the PE-coated packaging paper, and the formed pattern was not conductive probably

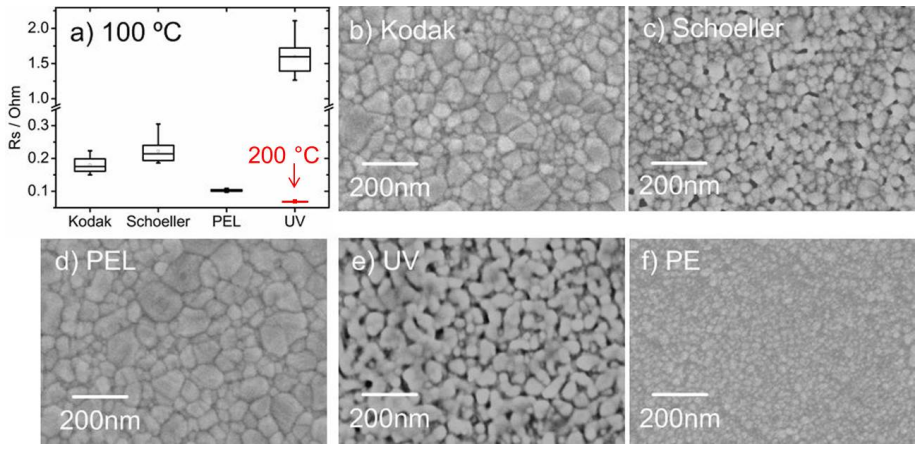

Figure 3.13: (a) Sheet resistance of inkjet-printed four-pint structures on different paper substrates. The SEM pictures of the printed structures on (b) Kodak, (c) Schoeller, (d) PEL, (e) UV, (f) PE, respectively. The printed structures on the PE-coated packaging paper were not conductive. Figure adapted from Paper IV.

because there was large gap between the particle grains as observed from its SEM picture. Although the sheet resistance obtained from the UV-coated packaging paper was about 10 times higher than that from the inkjet papers, this resistance value is acceptable to many applications. Moreover, when the UV-coated packaging paper was sintered at 200 °C, the sheet resistance was reduced to around 0.05 Ω/sq. This value is close to what was obtained from the PEL inkjet paper sintered at 150 °C as seen from Fig. 3.12. One of the advantages of the packaging paper is its heat resistance. Mostly inkjet papers cannot bear a sintering temperature above 150 °C [35], while the UV-coated packaging paper can stand up till 240 °C.

3.3.3 Reliability Evaluation under 85 °C/85% RH Aging Test

Paper swells or shrinks when its moisture content increases or decreases, and therefore, the reliability of printed conductors on paper substrates in a humid environment becomes an important practical concern, especially when they are to be applied for humidity sensors. The electrical reliability of inkjet-printed conductors on two types of paper substrates (PEL inkjet paper and Korsnäs UV-coated package paper) was evaluated by performing an aging test according to an industry standard [163]. The samples were stored in an environmental chamber with conditions set at 85 °C and 85% RH for 1008 hours in total. The high temperature was employed to accelerate the penetration of moisture through the substrate [163]. The samples were brought out of the chamber for sheet resistance measurement every week.

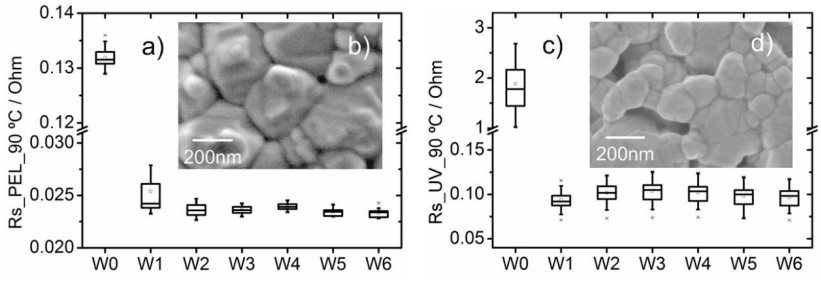

Figure 3.14: Sheet resistance variation in the 85 °C/85% RH aging test for inkjet-printed four-point structures on a) PEL inkjet paper with b) SEM picture after Week 6, and on c) UV-coated packaging paper with d) SEM picture after Week 6. Figures adapted from Paper IV.

Three sets of samples, which were sintered at 90, 120, and 150 °C respectively, were used in the aging test. Fig. 3.14 illustrates the sheet resistance variation of the samples sintered at 90 °C. The resistance variation for the samples sintered at 120 or 150 °C follows the same tendency as the samples sintered at 90 °C. It can be seen that the resistance substantially decreased after the first week and became quite stable afterwards for both paper substrates. Zapka et al. reported that silver nanoparticle inks could be chemically sintered at room temperature or slightly elevated temperatures by dissolving the ligands from the nanoparticles with salts [159]. In addition, Andersson et al. found that high moisture content in the coating polymer of the metal nanoparticles could facilitate the ion transportation from the paper coating to the ink, depending on the paper coating material and the polymer type [164]. Therefore, the decrease in resistance was probably caused by a chemical sintering effect which was triggered by the high humidity level. Moreover, it was observed that 4 out of 25 samples on PEL inkjet paper broke after Week 4, while only 1 out of 25 samples on UV-coated packaging paper showed high resistance after Week 5. The good reliability of the packaging paper in a harsh environment strengthens its potential as substrate for printed humidity sensors.

3.3.4 Mechanical Flexibility Evaluation

Bending tests were also performed to evaluate the mechanical flexibility of printed conductors on paper substrates as illustrated in Fig. 3.15. Tensile stress was applied to the conductor when the conductor was placed facing upwards in the Cond-UP setup, while compressive stress was applied when the conductor was placed facing downward the cylinder in the Cond-Down setup. The tested samples were one-layer conductive strips (1.3-cm wide and 2-cm long) inkjet-printed on PEL paper substrate using the NPS-JL ink.

Firstly, it was found that the flexibility of the printed conductors was related to

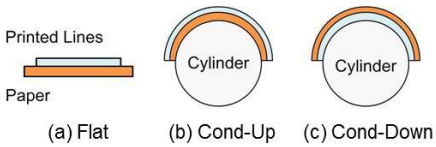

Figure 3.15: Schematic illustration of the bending test setup of printed conductive structures on PEL paper in (a) flat, (b) Cond-Up, and (c) Cond-Down position, respectively. Figures adapted from Paper V.

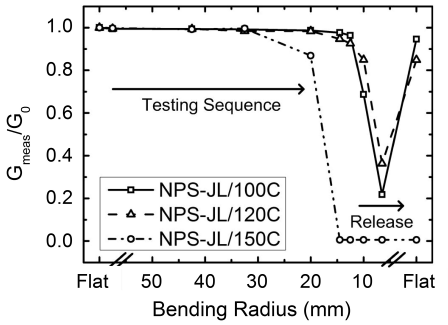

Figure 3.16: Conductance variation of printed conductors on PEL paper which were sintered at different temperatures. G_{meas} denotes the conductance measured at a specific bending radius and G_0 the initial conductance of the sample when it is flat before bending. G_0 of the samples sintered at 100, 120 and 150 °C is 0.60, 0.71 and 1.15 S, respectively. Figure adapted from Paper V.

the sintering temperature. As shown in Fig. 3.16, under one cycle of the Cond-Up bending test, the 100 °C samples withstood the bending radius down to 10 mm, and almost recovered their initial resistances once being released from bending, whereas the 150 °C samples showed considerable variation in conductance when the bending radius was 20 mm. The difference in flexibility was probably due to the oxidation or decomposition of the coating material on the paper substrate at higher sintering temperature.

It was also found that the printed conductors could stand smaller bending radius under compressive stress than under tensile stress as shown in Fig. 3.17a. Under the Cond-Up test, the conductance of the samples sintered at 100 °C remained almost stable till the bending radius of 20 mm. Then the conductance significantly reduced when the bending radius decreased to 10 mm, and half of the samples broke. Under the Cond-Down test, the conductance of the samples increased slightly as the bending radius decreased. However, all the samples withstood the bending radius down to 10 mm, and almost recovered their initial resistance once being released. As mentioned earlier, the f-MWCNTs resistors fabricated on paper substrates showed

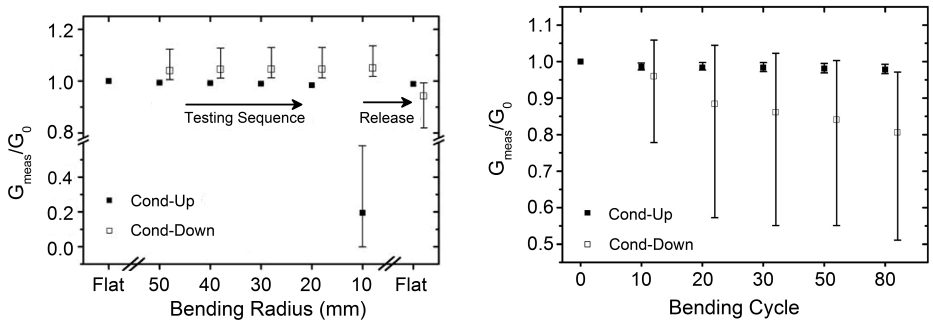

(a) (b)

Figure 3.17: Conductance variation of printed conductors on PEL paper substrate sintered at 100 °C (a) as a function of bending radius, and (b) as a function of bending cycles in the Cond-Up and Cond-Down setup, respectively. Bending radius is 20 mm. Each test group includes 8 samples. The mean G_0 is 0.62 S. Figures adapted from Paper V.

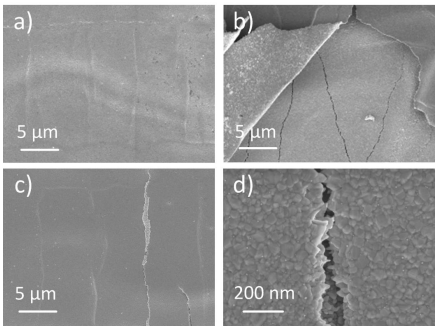

Figure 3.18: HRSEM pictures of printed conductors after being bent with a) Cond-Down, and b) Cond-Down with peeling-off surface metal layer, c) Cond-Up, and d) the enlarged image of the crack in (c). Figures adapted from Paper V.

reduced flexibility as compared with those on plastic films. It can be explained by the above observation that the printed conductors on PEL paper substrate could not bear the bending radius below 20 mm under the Cond-Up test.

An 80-times repeated bending test was also done to the printed conductors, and their conductance variations are shown in Fig. 3.17b. The bending radius was 20 mm in this experiment. The conductance was measured when the samples were released from bending. It can be seen that the conductance remained almost unchanged in the Cond-Up setup, while it gradually increased in the Cond-Down setup. The different flexibility between the two setups could be explained by

HRSEM as shown in Fig. 3.18. Under compressive stress, cracking started from the interface between the conductor and the paper substrate. The surface of the conductor formed ridges, but the electrical connection was still maintained here until the thorough rupture of the whole conductive layer. Under tensile stress, the cracking began at the surface of the conductive layer, and progressed through the whole conductive layer quickly.

Chapter 4

RFID Sensor and Integration

This chapter will first review the existing RFID tag technologies and the corresponding integration methods of sensing functions. Compared with the solutions based on a silicon-based chip, the printable chipless RFID sensor tags are very attractive to applications where tags of very low cost are required. Therefore, three construction methods of chipless RFID humidity sensor tags were investigated and implemented, based on backscatter modulation, time-domain reflectometry, and frequency-spectrum signature, respectively. The discussion refers to Papers I, II, VI, VII and VIII.

4.1 RFID Tag Technologies

An overview of the existing RFID tag technologies is prerequisite for exploring the RFID sensor solutions. An RFID system typically consists of three elements: tags, readers and a back-end database. The tags carry the ID information, and the readers can read the information from the tags. The information acquired by the readers is then passed to the database which is responsible for managing the data and related business transactions [165].

Based on their power sources, RFID tags can be classified into three types: active, semi-passive and passive tags [31]. Active tags have on-board power source, such as batteries, and periodically send the ID signals to an RFID reader and possibly to other tags as well. Semi-passive tags transmit the ID signals using the EM waves sent out by the reader, but still need a battery to power up the on-board or off-board circuitry. Passive tags rely only on the reader's radio energy to power up the tag, and transmit the ID signals in response to the interrogation signals sent by the reader. The choice of RFID tags depends on application requirements including performance, cost and other parameters. Active tags have the longest operation range and are more reliable, but are larger in size and more expensive ($15-$100) [166]. Passive tags have the shortest operation range, but are smaller, lighter, cheaper ($0.15-$5), battery-free and maintenance-free, thereby becoming

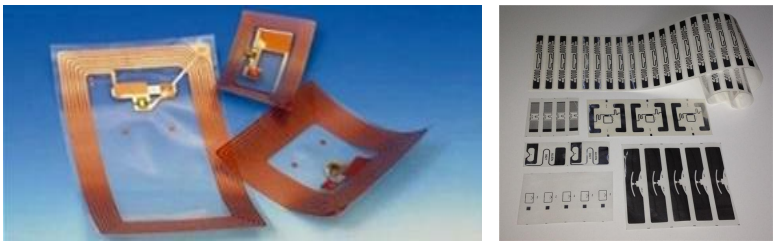

(a) (b)

Figure 4.1: Examples of IC-containing commercial passive RFID tags: (a) tags based on near-field coupling, courtesy to Texas Instruments Inc. [170], and (b) tags based on far-field coupling, courtesy to Alien Technology LLC. [171]

the most prevalent type in the market nowadays [165–167].

Commercial Passive RFID Tags

The majority of current commercial passive RFID tags contain at least an integrated circuit (IC) chip and an antenna as shown in Fig. 4.1. They are powered up by an EM field around the reader and transmit RF signals based on two coupling principles: reactive near-field coupling (inductive coupling) and radiative far-field coupling [31]. For the near-field tags, changing the load on the tag's coil antenna varies the current in the coil, and hence causes a small variation in the reader's antenna that is to be detected. These tags typically operate in the 125-135 kHz low frequency (LF) or in the 13.56 MHz high frequency (HF) band, and have a short operation range of less than 30 cm [168]. Nevertheless, the near-field RFID tags found application in where high security is demanded, and they are less prone to be interfered by the presence of metal or liquid [169]. The far-field coupling is employed for longer operation range (up to 10 m). By changing the loading impedance on the antenna, the amount of the reflected energy is varied and then detected by the reader. This technique is called backscatter modulation. The far-field RFID tags usually operate in the 860-960 MHz ultra-high frequency (UHF) band or in the 2.45 GHz microwave band.

A third type of commercial passive RFID tags does not contain any IC chip, using a completely different physical principle called surface acoustic wave (SAW) technology [31]. A SAW RFID tag, which typically operates at 2.45 GHz, comprises a piezoelectric substrate, an antenna, an interdigital transducer (IDT) and a set of code reflectors as shown in Fig. 4.2. The tag receives an interrogating radio-wave pulse through the antenna. The IDT converts the radio wave to a surface acoustic wave based on the piezoelectric effect. The SAW pulse propagates away from the IDT and passes through the set of reflectors, generating a uniquely encoded acoustic wave pulse train. The reflected pulses propagate back toward the

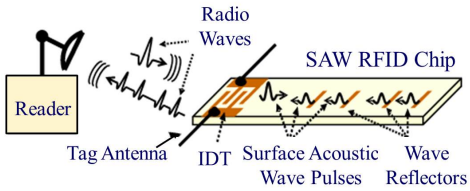

Figure 4.2: Illustration of SAW tag operation. Courtesy to RFSAW, Inc. [175]

IDT and get transmitted through the antenna back to the reader. The ID data is encoded based on the time delays produced by the reflectors, known as time position encoding or pulse position modulation [172]. The SAW RFID tags do not require direct-current (DC) power and hence consume less power than the above chip-based tags. They also have other advantages, such as long operation range (up to 15 m), high reliability in the presence of water and metal, or in a harsh environment (e.g., at a temperature up to 400 °C) [173]. However, the piezoelectric materials are expensive and require high temperature deposition or treatment for good crystal formation [174]. Moreover, the manufacturing process of the SAW devices involves complex nanometer lithography. As a result, the SAW RFID tags do not cost considerably less than the chip-based tags [169].

Emerging Printable Chipless RFID Technologies

During the past decade, great research efforts were made to develop printable chipless RFID tags which are expected to cost $0.01 and less [36, 176, 177]. Research work was carried out to develop low-cost RFID tags based on printed organic transistors. Such all-printed tags operating at 135 kHz and 13.56 MHz were reported [178, 179]. However, the electron mobility and integration density of printed transistors achieved so far are not sufficient for implementing faster and more complex circuitry [180]. More innovative chipless RFID technologies are emerging, falling into three main categories based on their encoding principles [177]:

- Backscatter modulation-based chipless RFID tags

  This type of chipless tag encodes the ID data by varying the phase information of the backscattered signals using reactive loading on the antenna, such as a short-circuit LC ladder [181], left-hand delay lines [182], and microstrip-based stub reflectors [183]. The encoded bit number is limited, but these tags have simple architectures, operate over narrowband and hence simplify the implementation of the RFID reader [177].

- Time domain reflectometry (TDR)-based chipless RFID tags

  Inspired by the working principle of the SAW tags, several TDR-based tags by means of transmission lines were proposed in view of printability. The ID

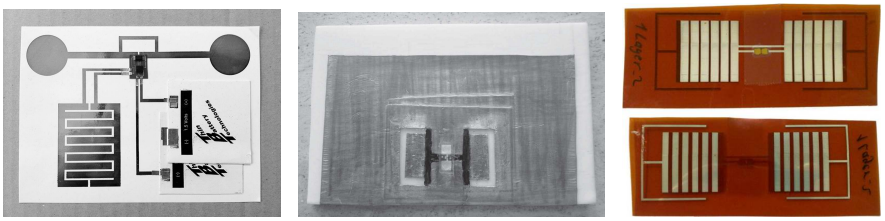

(a) (b) (c)

Figure 4.3: Examples of chip-based RFID sensor solutions: (a) an RFID tag integrating an external printed humidity sensor, (b) an RFID humidity sensor based on a sensitive polymer-loaded antenna, and (c) an inkjet-printed RFID humidity sensor tag using polyimide as sensing substrate. Figures adapted from [116, 196, 197], respectively.

data is encoded either using the delay time of the reflected pulses produced by transmission lines [184, 185] or using the presence or absence of a pulse at a predetermined time position produced by capacitors [103, 186]. These tags are interrogated by very short pulses which have an ultra-wideband spectrum (UWB), and hence require a high-speed and complex UWB transceiver as reader. The encoded bit number is also limited. Nevertheless, these tags offer a number of advantages such as longer reading range, lower power consumption, and built-in applicability for positioning applications [30, 177].

- Frequency spectrum signature-based chipless RFID tags

  This type of tags encodes the ID data in frequency domain by means of resonating structures, for example, capacitively-tuned microstrip dipoles [187], space-filling curves [188], C-like scatters [189,190], multiresonant dipoles [191], spiral resonators [192], split ring resonators [193], and inductive-capacitor (LC) resonators [194, 195]. The encoding is performed by either associating each bit of the ID with the presence or absence of a resonant peak at a predetermined frequency [192, 194], or by allocating a predetermined resonant frequency to each ID code [189, 195]. These tags require a wide frequency spectrum, but offer the advantages such as robustness, high coding capacity and miniaturization [177].

4.2 RFID Sensor Solutions

In accordance to the RFID tag technologies, the RFID sensor solutions can be generally divided into two groups: chip-based solutions and chipless solutions. The chip-based solutions include embedding a sensor in an RFID chip [198], integrating an external sensor to an RFID chip [164, 196, 199, 200], depositing a sensing layer

on an RFID tag antenna [197, 201], or on the coupling area between the antenna and the chip [202], and using a sensitive substrate for the RFID tag [116]. Several examples are shown in Fig. 4.3. The chip-based solutions have high coding capacity and comply with the EPC Gen2 standard. However, like the chip-containing RFID tags, the manufacturing, testing and assembling of the silicon IC chip limit the cost reduction of the sensor tags. Chipless solutions are more attractive for applications where the low cost of the tag is the primary concern. As pioneer of the chipless RFID tags, the SAW tags have built-in capability to measure temperature because the surface acoustic wave on the substrate is temperature-sensitive [203]. But as mentioned earlier, the SAW RFID tags require expensive piezoelectric materials and complex manufacturing processes. Their piezoelectric nature also impedes manufacturing of the SAW tags by printing techniques [192]. RFID sensor solutions based on printable chipless RFID encoding techniques are potentially much cheaper than the chip-based and the SAW RFID sensor tags. On the other hand, signal collision between nearby RFID tags is a more challenging problem for the tags without an IC chip [190], although several anti-collision techniques were proposed [204, 205]. Therefore, the chipless solutions show more promise of success in short-range identification and sensing applications where fewer tags are activated simultaneously.

In this thesis, three construction methods of printable chipless RFID sensor tags were investigated as follows:

By monitoring its backscattered power, a passive wireless sensor could be realized by loading a proper antenna with a resistive-type sensor [14, 206]. An RFID sensor tag could then be constructed by placing this sensor together with an chipless RFID tag which encodes ID in the phase of the backscattered signal or in the frequency spectrum [206, 207]. Note that the sensor and the RFID tag should work on orthogonal polarizations to avoid interfering with each other [207]. Utilizing the backscatter modulation, a flexible humidity sensor was demonstrated for UHF RFID applications in this thesis. Section 4.3 will first introduce the backscatter modulation principle. Then the humidity sensor and its design optimization will be presented and discussed.

A TDR-based chipless RFID sensor solution encodes the ID in the delay time of the reflected pulse introduced by transmission lines, and performs the sensing function though modulating the phase/amplitude of the reflected pulse by adding a capacitive/resistive-type sensor at the end of the transmission lines [208–210]. Based on this principle, a fully-printed RFID humidity sensor tag was demonstrated in this thesis. Such sensor tag is typically implemented to monitor one target at one time. In this thesis, a TDR-based sensor for monitoring multiple parameters was also proposed. Section 4.4 will first introduce the working principle of the time-coded chipless RFID sensor tag. Then the printed humidity sensor tag and the multi-parameter sensor design will be presented and discussed.

The third method encodes the ID data in the frequency domain using resonators or resonating structures, and performs the sensing function through measuring the resonant frequency variation of one additional resonator covered by sensing mate-

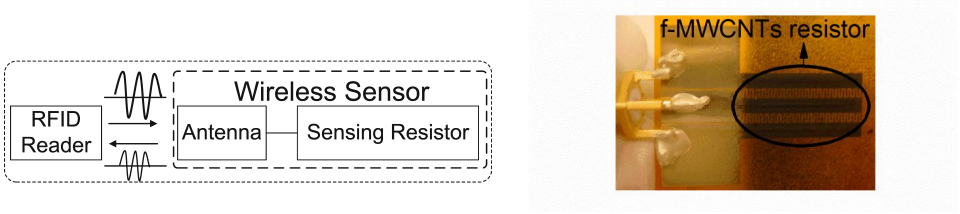

(a) (b)

Figure 4.4: (a) Block diagram of a passive wireless sensor based on backscatter modulation, (b) photograph of an f-MWCNTs resistor that is connected with a coplanar waveguide for characterization of the voltage reflection coefficient at high frequencies. Figures adapted from Paper I.

rial [206, 211]. The advantages of this method are coding capacity, miniaturization, adaptivity for multi-parameter monitoring and so on [190, 211]. As discussed above, chipless RFID sensor tags are more suitable for short-range monitoring applications. Therefore this thesis proposed a chipless RFID sensor tag operating wirelessly through near-field inductive coupling. Section 4.5 will first introduce the operation principle of this tag. Two detection methods are then introduced and compared. The sensor design optimization is also discussed.

4.3 Backscatter Modulation-based UHF Humidity Sensor

4.3.1 Sensor Operation Principle

Fig. 4.4a shows the block diagram of a passive wireless sensor based on backscatter modulation. The sensor is essentially an antenna loaded with a resistor which varies its own resistance with a targeted physical quantity. When the RFID reader sends a continuous EM wave signal to the sensor, the sensor will reflect back power which is termed as backscattered power. The backscattered power consists of two parts: 'structural-mode' scattering and 'antenna-mode' scattering [212]. The structural-mode scattering occurs owing to the current induced on the antenna, which is related to the structure, shape and material of the antenna and independent of its loading conditions [213, 214]. The antenna-mode scattering occurs due to the mismatch between the antenna impedance and the load impedance [212], thereby conveying the information of the sensing resistor. The backscattered power received by the reader, $P_{\text{reader-rx}}$, can be calculated by [14],

$$P_{\text{reader-rx}} = P_{\text{reader-tx}} G_{\text{r}}^2 G_{\text{s}}^2 \eta (\frac{\lambda}{4d})^4 \tag{4.1}$$

where $P_{\text{reader-tx}}$ is the power fed into the antenna of the RFID reader, G_{r} and G_{s} the gain of the reader antenna and the sensor antenna, respectively, η the

power refection coefficient, λ the wavelength, and d the distance between the reader and the sensor. The power reflection coefficient of the sensor (η) depends on the impedance mismatch between the antenna and the sensing resistor as given by [14],

$$\eta = |S_{11}|^2 = (\frac{Z_{\mathrm{L}} - Z_{\mathrm{A}}^*}{Z_{\mathrm{L}} + Z_{\mathrm{A}}})^2 \tag{4.2}$$

where S_{11} is the voltage reflection coefficient of the sensor antenna, Z_{A} is the impedance of the antenna, Z_{A}^* the complex conjugate of Z_{A}, and Z_{L} the impedance of the sensing resistor. Combining the above two equations, it is clear that when the load impedance on the antenna varies, the backscattered power changes correspondingly. It can be further derived from Eq. 4.2 that the load impedance (Z_{L}) is preferred to be comparable to the antenna impedance (Z_{A}) to obtain higher sensitivity, i.e., larger variation in the power reflection coefficient (η) corresponding to a certain change of Z_{L}. Since the resistive part of the antenna impedance is typically small to achieve lower power consumption and better radiation efficiency, the sensing resistor with high conductivity is favored by this wireless sensing principle.

Yang et al. proposed and demonstrated an ammonia sensor based on the backscatter modulation using printed SWCNTs [14]. However, their results were preliminary and only showed their sensor could indicate the presence of ammonia qualitatively. In addition, they did not perform measurement above 1 GHz.

In this thesis, a flexible humidity sensor based on an f-MWCNTs resistor was presented, and a wireless humidity sensor could be readily demonstrated by connecting the f-MWCNTs resistor to a printed UHF antenna. It was found that the parasitic capacitance between the resistor electrodes played a key role in the sensor response in terms of sensitivity and operating frequency range. By adjusting the parasitic capacitance, the sensor could measure the humidity level from 30% to 90% RH over the frequency range from 40 kHz to 2 GHz. As shown in Fig. 4.4b, a short coplanar waveguide (CPW) was used to connect the f-MWCNTs resistor to a vector network analyzer (VNA) for the voltage reflection coefficient measurement. According to Eq. 4.1-4.2, the magnitude of S_{11} can be used as a measure of the wireless sensor if all the other parameters in the equations are constant.

4.3.2 Sensor Structure Optimization and Performance

The frequency-dependent response (S_{11}) of the humidity sensor based on f-MWCNTs resistors was strongly affected by the electrode structure of the resistor as shown in Fig. 4.5. Two sensors with different resistor-electrodes were measured at 50%, 70%, and 90% RH, respectively. As illustrated in the insets, IDEs and flat parallel rectangular electrodes (REs) were used for the f-MWCNTs resistor in the two sensors, respectively. The magnitudes of S_{11} of both sensors responded similarly up to around 600 MHz. When the frequency was above 600 MHz, however, the magnitudes of S_{11} of the two sensors evolved differently. As seen from the real lines in Fig. 4.6a, the sensitivity, defined by the difference of ($|S_{11}|$) between 50% and 90% RH, started to decrease at 600 MHz for the sensor with IDEs. In stark

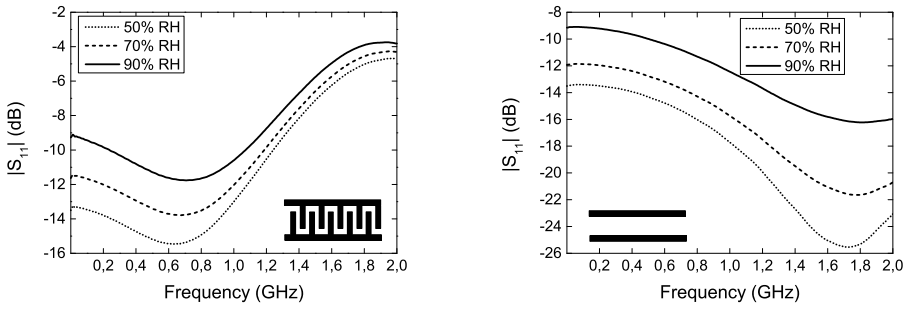

Figure 4.5: Measured voltage reflection coefficient ($|S_{11}|$) of the f-MWCNTs sensors with (a) IDEs and (b) REs as a function of frequency at 50%, 70%, and 90% RH at 25 °C. Inset: schematic electrode structure. Figures adapted from Paper I.

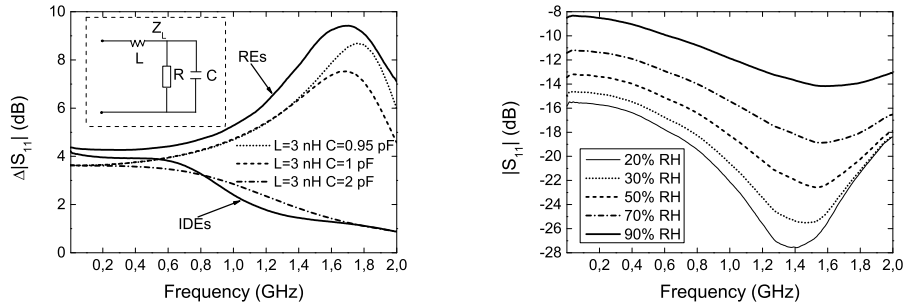

Figure 4.6: (a) $\Delta|S_{11}|$, defined as the difference of S_{11} between 50% and 90% RH in Fig. 4.5, as a function of frequency for the f-MWCNTs sensors with IDEs and REs configuration (real line), and the simulated results (dashed line) with different values of L and C based on the equivalent circuit of the f-MWCNT resistor. R was experimentally derived to be 78 Ω at 50% RH and 100 Ω at 90% RH from both sensors. Inset: equivalent circuit of the f-MWCNT resistor. (b) Measured voltage reflection coefficient ($|S_{11}|$) as a function of frequency for a new f-MWCNTs sensor with IDEs (which have the parasitic capacitance of 1.0 pF between the electrodes) at different relative humidity levels. Figures adapted from Paper I.

constrast, the sensitivity for the sensor with REs started to increase at 600 MHz and reached its maximum at around 1.8 GHz.

The dramatic influence of the resistor-electrode structure on the sensor response could be explained by the total complex impedance of the f-MWCNTs resistor. The equivalent circuit of the f-MWCNTs resistor is illustrated in the inset of Fig. 4.6a, where R is predominantly attributed to the resistance of f-MWCNTs, C represents mainly the parasitic capacitance between the resistor-electrodes, the inductance L comes from the metal electrodes, and Z_{L} represents the total complex impedance of the R, C, and L network. By simulating this network in Agilent Advanced Design System (ADS) with varied values of L and C, it was found that the significantly improved sensitivity of the sensor with REs over the sensor with IDEs was mainly attributed to the variation of the parasitic capacitanc C as shown by the dash lines in Fig. 4.6a. The parasitic capacitances between the IDEs and the REs was measured to be around 2.2 pF and 1.0 pF, respectively.

Another sensor with redesigned IDEs was fabricated. The dimensional structures of the new IDEs were designed to have a capacitance of 1.0 pF between the electrodes using the analytical model of IDEs as presented in Paper VI. As seen from Fig. 4.6b, the magnitude of S_{11} of the new sensor responded similarly to that obtained from the sensor with REs (Fig. 4.5b), which confirms the key role of the parasitic capacitance between the electrodes on the sensitivity. The small difference in the responses between these two sensors probably arose from a slightly larger inductance in the IDEs. Additional measurements at lower RH levels showed that this sensor could detect the humidity level from 30% to 90% RH over the frequency range from 40 kHz to 2 GHz, and from 20% to 90% RH over the frequency range from 40 kHz to around 1.6 GHz.

4.4 TDR-based Chipless RFID Humidity Sensor Tag

4.4.1 Tag Operation Principle

Fig. 4.7a shows the block diagram of an RFID sensor tag based on TDR. The sensor is composed of an UWB antenna, transmission lines and a sensing resistor. As mentioned previously, an UWB pulse with very short time duration is used as interrogating signal for such TDR-based tags. The operation scheme of the tag is illustrated in Fig. 4.7b. Once being interrogated, the tag would first scatter back a pulse owing to the structural-mode scattering. After certain time, another pulse would be reflected back owing to the antenna mode scattering. The time delay between the two reflected pulses is introduced by the transmission lines as given by,

$$\Delta t = \frac{2l}{\nu} \tag{4.3}$$

where l is the length of the transmission lines, and ν is the velocity of propagation of the pulse along the transmission lines. The length of the transmission lines is varied to encode the ID in the time delay (Δt). This chipless RFID technique based TDR was proposed by Ramos et al. in [215]. It can be seen that the interrogating

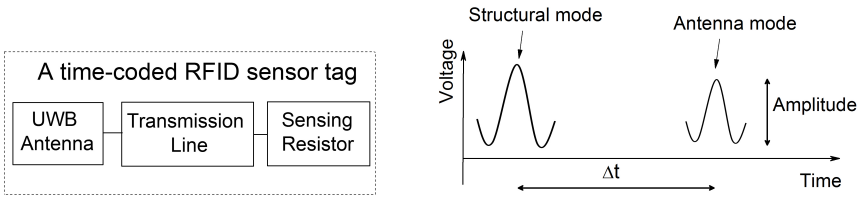

(a) (b)

Figure 4.7: (a) Block diagram of a time-coded RFID sensor tag based on TDR, and (b) operation scheme of the tag. Fig. (b) adapted from [209].

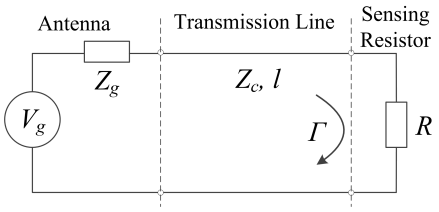

Figure 4.8: Equivalent circuit of the time-coded RFID sensor tag excluding the structural-mode scattering effect. Γ denotes the voltage reflection coefficient due to impedance mismatch between the resistor and transmission lines.

signal should be such a short pulse that the two reflected pulses do not overlap. The antenna-mode pulse occurs due to the impedance mismatching between the sensing resistor and the transmission lines. Excluding the structural model scattering, the tag could be modeled using an equivalent circuit as drawn in Fig. 4.8, where the tag antenna is modeled as a voltage generator $V_{\mathrm{g}}(t)$ with internal impedance Z_{g} in the receiving mode. Z_{C} indicates the characteristic impedance of the transmission lines, and R the resistance of the sensing resistor. The voltage waveform of the reflected antenna-mode pulse can be given approximately by [216],

$$V_{\mathrm{ref}} = \frac{Z_{\mathrm{C}}}{Z_{\mathrm{C}} + Z_{\mathrm{g}}} \frac{R - Z_{\mathrm{C}}}{R + Z_{\mathrm{C}}} V_{\mathrm{g}}(t - \frac{2l}{\nu}) e^{-2i\alpha l} \tag{4.4}$$

where α is the attenuation constant in the transmission line. As the UWB pulse takes up a very wide frequency spectrum, the attenuation constant at the center frequency of the pulse could be used in Eq. 4.4 for approximation. Then the energy of the reflected pulse can be calculated by,

$$E_{\mathrm{ref}} = (\frac{Z_{\mathrm{C}}}{Z_{\mathrm{C}} + Z_{\mathrm{g}}})^2 (\frac{R - Z_{\mathrm{C}}}{R + Z_{\mathrm{C}}})^2 e^{-4i\alpha l} \int_{\frac{2l}{\nu}}^{\frac{2l}{\nu}+T} \frac{V_{\mathrm{g}}^2(t - \frac{2l}{\nu})}{Z_{\mathrm{g}}} dt \tag{4.5}$$

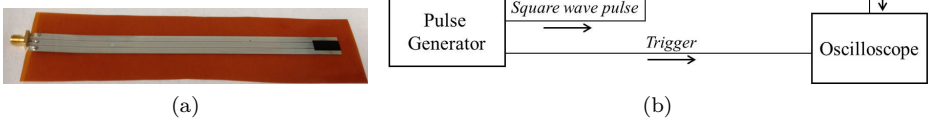

(a) (b)

Figure 4.9: (a) A fully inkjet-printed TDR-based humidity RFID sensor tag on polyimide foil without integration of the UWB antenna, and (b) block diagram of the measurement setup for the tag.

where T is the time duration of this short pulse. The time delay (Δt) as Eq. 4.3 gives should be longer than the pulse duration (T) to avoid overlapping between the structural-mode pulse and the antenna-mode pulse in the time domain.

Like the backscattered power, the transmitted energy by the reflected pulses decays with distance by 20 dB/decade as Eq. 4.1 indicates. Thus the pulse energy or amplitude received by the reader depends on the reading distance. Girbau et al. presented a time-code UWB chipless RFID sensor system for temperature monitoring by integrating a stand-alone flat chip temperature sensor [209]. They pointed out that the structural-mode pulse could serve as a reference to the antenna-mode pulse, since it is independent of the sensing resistor, and therefore, the ratio of these two pulses could be used as an actual measure of the sensor to remove the influence of the reading distance [209].

Employing this tag principle, a fully-printed flexible RFID sensor tag for humidity monitoring was demonstrated in this thesis. This study focused on the characterization of the humidity-sensing performance was focused. In addition, a multi-parameter sensor based on TDR was proposed and theoretically analyzed.

4.4.2 A Printed Humidity RFID Sensor Tag based on TDR

Fig. 4.9a shows the inkjet-printed sensor tag consisting of a CPW and an f-MWCNTs resistor. CPW was chosen as transmission line because: 1) its uniplanar structure requires only single-side printing process, and 2) it is easy to change its characteristic impedance by adjusting the ratio of the width of the center signal conductor and the gap between signal and ground conductors. The UWB antenna was not implemented at the moment, so the characteristic impedance of the CPW was designed to be 50 Ω to match that of the measurement equipment. The dimensions of the CPW were calculated using the Line Calculation tool in ADS based on the printing process parameters obtained from experiments. The center signal conductor of the

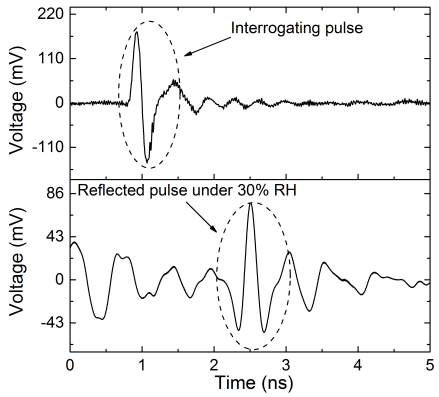

Figure 4.10: Time-domain voltage waveform of the interrogating pulse and reflected pulse from the sensor under 30% RH.

CPW was 4044 μm wide, and the gap between the conductors was 120 μm wide. The length of the CPW was set to be 16.5 cm to produce a 1.3-ns delay between the structural-mode and the antenna-mode pulse. The CPW, together with electrodes for the resistor, was printed at 1270 dpi resolution on a 125-μm thick PI foil (Kapton® HN, Dupont) using an alcohol-based silver nanoparticle ink (CCI-300, Cabot Corp.). The printed pattern was then sintered in an oven at 300 °C for 30 minutes. The sintered metal layer was about 0.5 μm thick and its conductivity was around 2×10^7 S/m. Then f-MWCNTs were printed on the electrodes to form a humidity-sensing resistor at the end of the CPW. It should be noted that the resistance variation range of the f-MWCNTs resistor should be kept either below 50 Ω or above it to ensure a one-to-one response between RH and pulse energy for this demonstrator as seen from Eq. 4.5. A surface mount device (SMD) coaxial connector was assembled to the sample for sensitivity measurement in the setup as illustrated in Fig. 4.9b. As mentioned in Chapter 2, the PI foil itself was often used as humidity-sensing substrate, making it not the ideal substrate for this sensor tag. Because the Cabot ink requires high sintering temperature to provide sufficient conductivity for this application, PI was used for its high heat tolerance. By using a low-temperature-sinterable ink, e.g., the NPS-JL, the sensor tag could be demonstrated on other substrates which are not sensitive to humidity.

Fig. 4.10 depicts the interrogating pulse, and the antenna-mode reflected pulse measured when the tag was placed under 30% RH. The time duration and the center frequency of the interrogating pulse were around 0.7 ns and 2 GHz, respectively, and the 10-dB bandwidth of the pulse was larger than 500 MHz. It can be seen that the voltage waveform of the reflected pulse at 30% RH was not exactly in the same shape as the interrogating pulse. The ringing occurring in the interrogating

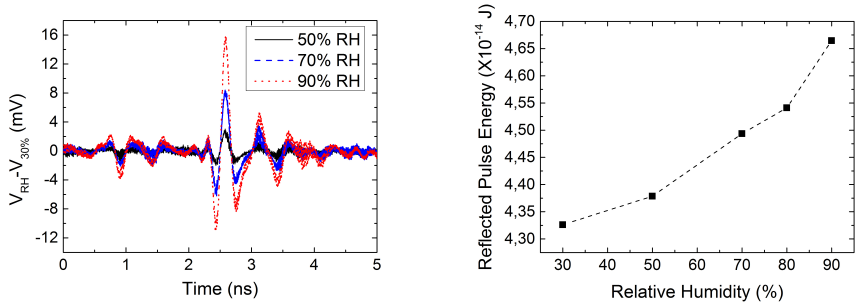

(a) (b)

Figure 4.11: (a) Variation in time-domain voltage waveform of the reflected pulse from the sensor under 50%, 70% and 90% RH, respectively, as relative to the reflected pulse under 30% RH. V_{RH} and $V_{30\%}$ denote the voltage waveform measured at a specific RH and 30%, respectively, (b) energy of the reflected pulse as a function of relative humidity.

pulse also became more severe in the reflected pulse. In Fig. 4.8 and Eq. 4.4-4.5, the sensing resistor was treated as merely resistive for simplicity in the theoretical analysis. In fact, there was parasitic capacitance and inductance in the f-MWCNTs resistor as discussed previously. The parasitics caused the shape of the reflected pulse to be different from that of the interrogating pulse [216]. Another important reason for the different waveforms was the imperfect impedance matching in the measurement setup. To clearly show the variation in the reflected pulses between different relative humidity levels, the waveform measured at 30% RH was subtracted from the waveforms measured at the other humidity levels, as shown in Fig. 4.11a. The pulse amplitude increased as the humidity level increased. Then the reflected pulse energy was calculated by integrating the original voltage waveform over the time duration of the pulse. Fig. 4.11b shows that the pulse energy increases with the relative humidity level monotonously.

4.4.3 A Multi-parameter Sensor Design

Fig. 4.12a shows the block diagram of a multi-parameter wireless sensor based on TDR, and the operation scheme of the sensor is illustrated in Fig. 4.12b. The sensor is composed of an UWB antenna, pairs of transmission lines and sensing resistors. Each sensing resistor is supposed to be sensitive to a specific target. When the reader sends out an interrogating pulse, the sensor would first scatter back a pulse owing to the structural-mode scattering, and then reflect back several pulses depending on the number of the sensing resistors owing to the antenna-mode scattering. By properly setting the lengths of the transmission lines, the reflected pulses

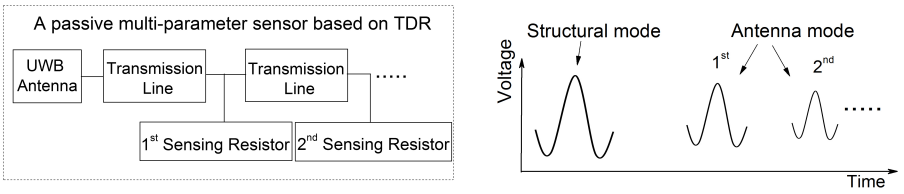

(a) (b)

Figure 4.12: (a) Block diagram of a TDR-based wireless sensor for monitoring multiple parameters simultaneously, and (b) operation scheme of the wireless sensor. Figures adapted from Paper VIII.

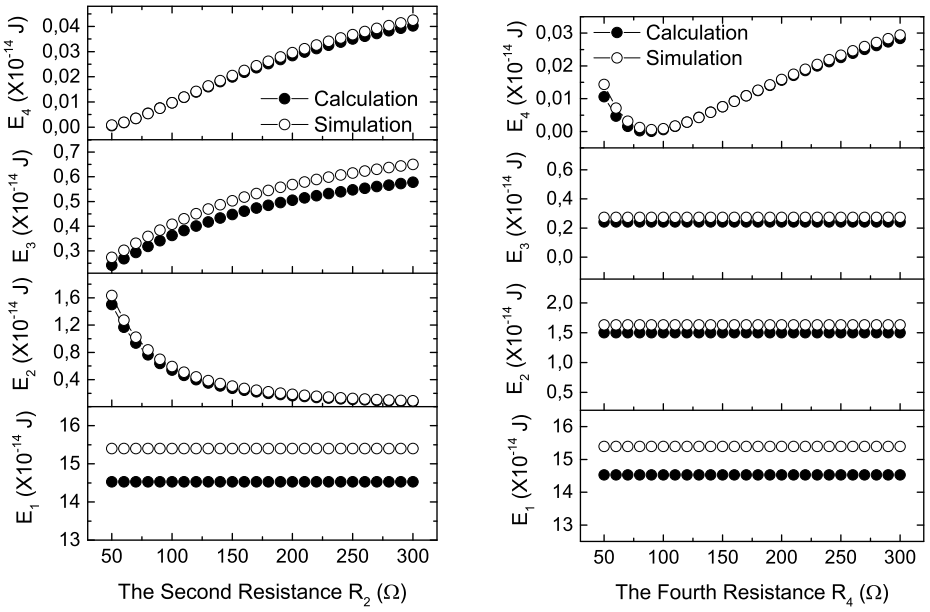

(a) (b)

Figure 4.13: Dependence of the energies of the four reflected pulses on (a) the second resistance R_2 when R_1=R_3=50 Ω and R_4=100 Ω, and on (b) the fourth resistance R_4 when R_1=R_2=R_3=50 Ω. R_1, R_2, R_3 and R_4 denote the four resistances in order and E_1, E_2, E_3 and E_4 the energies of the four reflected pulses in order. Figures adapted from Paper VIII.

are discrete in the time domain. Thus the reader could receive each reflected pulse individually, and then process out the resistances of all the sensing resistors. An algorithm for analyzing the pulse energies of the sensor with an arbitrary number (N) of resistors was introduced and verified by circuit simulation in ADS. In summary, the first resistance could be calculated out from the energy of the first pulse, and the i-th resistance could be calculated out from the energy of i-th reflected pulse and the preceding i-1 resistances ($2 \leq i \leq N$). More details of the algorithm are referred to Paper VIII.

However, the implementation of this multi-parameter sensor is challenging. The major difficulty is that the voltage amplitude of the reflected pulses decreases significantly due to the signal attenuation along the transmission lines and the signal loss caused by the impedance mismatching. As seen from Fig. 4.11a, the voltage amplitude of the first reflected pulse was less than half of the interrogating pulse. A sensor with four pairs of CPW and sensing resistors was simulated in ADS. The detailed parameters used in the simulation are referred to Paper VIII. Two conditions were simulated and also calculated using the proposed algorithm. As shown in Fig. 4.13, the simulation and the calculation agreed well. It can be seen, however, the pulse energy decreased nearly 1000 times from the first pulse to the fourth pulse. On top of that, it would be even more difficult to detect the variation of the pulse energy caused by the sensing resistors.

4.5 Chipless RFID Humidity Sensor Tag Based on Inductive Coupling

4.5.1 Tag Operation Principle

The chipless RFID sensor tag is composed of two planar LC resonators whose layout is shown in Fig. 4.14a. The two resonators take up separate resonant frequency bands to serve their own purposes as illustrated in Fig. 4.14b. One resonator encodes the ID data utilizing frequency-spectrum signature (RFID resonator). Its resonant frequency is varied to represent different ID codes by connecting/disconnecting certain interdigital fingers to/from the IDEs. This RFID encoding technique was previously proposed by our group, and a chipless RFID tag was realized on a paper substrate by inkjet printing [195]. However, paper is not an appropriate substrate for the RFID resonator as the ambient humidity influences the resonant frequency as discussed in Chapter 2. Thus the RFID resonator needs to be printed on a substrate with low moisture absorption, such as polyethylene terephthalate (PET). As shown in Table 4.1, the humidity variation did not affect the resonant frequency of an LC resonator printed on PET. The other resonator is used for sensing the ambient humidity level (sensor resonator). This sensor resonator is printed on a paper substrate, and its resonant frequency would decrease as the ambient relative humidity level increases as shown in Table 4.1.

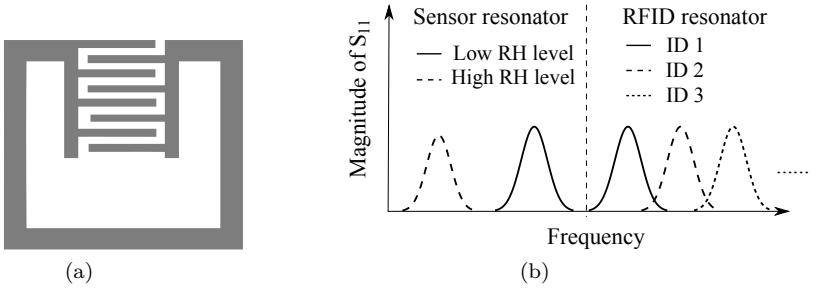

Figure 4.14: (a) Schematic layout of a planar LC resonator, and (b) operation principle of the chipless RFID humidity sensor based on frequency-spectrum signature. Figures adapted from Paper II.

Table 4.1: Comparison of an LC resonator printed on different substrates

Substrate (thickness)	Resonant frequency at 20%RH	Resonant frequency at 90%RH	Frequency variation ratio (%)
PET (125 μm)	142 MHz	142 MHz	0%
PI (125 μm)	161 MHz	157 MHz	2.5%
PEL (200 μm)	157 MHz	131 MHz	16.6%

4.5.2 Tag Detection Methods

Two detection methods were compared: one-antenna setup and two-antenna setup. In the one-antenna setup, a single-turn loop antenna was connected to a VNA as reader antenna, and the voltage reflection coefficient was measured and calculated to remove the background noise as given by,

$$|\Delta S_{11}| = \sqrt{(S'_{11} - S_{11}) \times (S'_{11} - S_{11})^*} \tag{4.6}$$

where S'_{11} is measured with the presence of the tag, S_{11} without the presence of the tag, and the symbol of '$*$' denotes a conjugate operation. In the two-antenna setup, two single-turn loop antennas were connected to the two ports of the VNA respectively, and the tag was placed in the middle. Then the forward voltage gain was measured and calculated as given by,

$$|\Delta S_{21}| = \sqrt{(S'_{21} - S_{21}) \times (S'_{21} - S_{21})^*} \tag{4.7}$$

where S'_{21} is measured with the presence of the tag, S_{21} without the presence of the tag. The reading distance in the two-antenna setup was defined as the distance between the tag and one of the antennas.

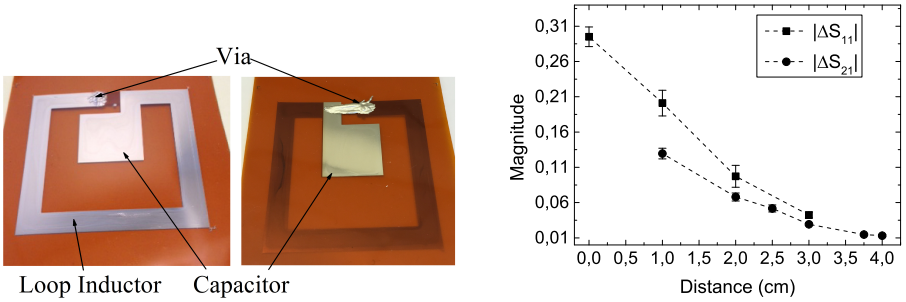

Figure 4.15: (a) Photographs of an inkjet-printed LC resonator which is composed of a square-shaped loop inductor and a parallel-plate capacitor from (left) top and (right) back. (b) Measured resonance amplitudes of an inkjet-printed LC resonator at different reading distances in both one-antenna and two-antenna setups. Six LC resonator samples with the same design were tested in each setup. Figures adapted from Paper VII.

The comparison of the detection methods was performed to inkjet-printed LC resonators which were composed of a square-shaped loop inductor and a parallel-plate capacitor as shown in Fig. 4.15a. Six samples with the same design were printed on PI foils with a silver nanoparticle ink (SunTronic EMD 5603, Sun Chemical Corp.) using a binary Xaar126 printhead with 50 pl drop volume. The printhead was inclined to print at 360 dpi resolution. The printed patterns were sintered at 250 °C for 1 hour. Then a through-substrate via was manually drilled and filled with electrically conductive epoxy to connect one end of the inductor to the other plate electrode of the capacitor on the backside of the substrate. The swept frequency range used in the measurement was from 20 kHz to 400 MHz.

The resonant frequencies obtained from the two setups were the same, while the peak amplitudes were quite different as shown in Fig. 4.15b. In both setups, the peak amplitude decreased as the reading distance increased. The decreasing speed of $|\Delta S_{21}|$ was slightly slower than that of $|\Delta S_{11}|$. As a result, the maximum reading distance of the tag in the two-antenna setup was marginally longer (around 4 cm) than that in the one-antenna setup (around 3 cm). On the other hand, $|\Delta S_{11}|$ was larger than $|\Delta S_{21}|$ within its readable distance. In addition, the size of the objects that the tags are to be attached on is limited in the two-antenna setup. Therefore, the one-antenna method is advantageous considering its larger response signal and setup simplicity, and thus chosen for the measurement of the chipless RFID humidity sensor tag. The inkjet-printed LC resonators on paper substrates showed good batch-to-batch reproducibility in terms of their resonant frequencies. The details of the reproducibility study are referred to Paper II.

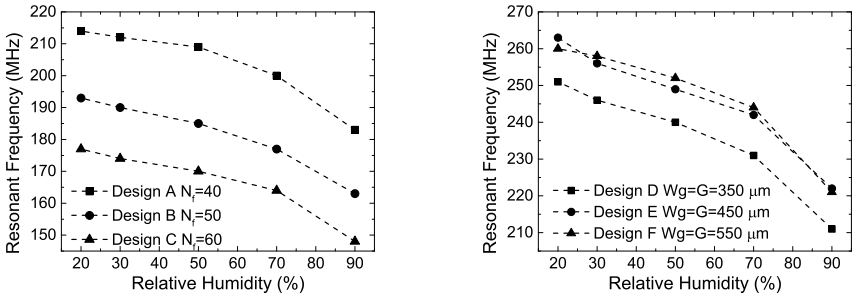

(a) (b)

Figure 4.16: Resonant frequencies of (a) the resonators with Designs A, B, C, respectively and (b) of the resonators with Designs D, E, F, respectively, at different relative humidity levels at 25 °C. All the samples were printed on PEL inkjet paper. Figures adapted from Paper II.

4.5.3 Sensor Performance and Structure Optimization

The sensing properties of the LC resonators printed on paper substrates were already discussed in detail in Chapter 2. When applying the resonators in remote monitoring, the decrease of their peak amplitude with high RH level, as shown in Fig. 2.11a, should be taken into consideration when determining the maximum reading distance of the sensor tag.

The sensitivity of the sensor resonator stems from the capacitance variation of the IDC. The influence of the IDC dimensions on the sensitivity was studied in this thesis. Fig. 4.16 shows the measured resonant frequencies of six sensor resonators with different dimensional designs. The dimensions and the response data of the resonators were listed in Table 4.2, where N_f denotes the number of fingers of the IDC, W_g the finger width and g the space between the fingers. The sensitivity, S, in the table is defined as below,

$$S = \frac{f_{\mathrm{r}90\%} - f_{\mathrm{r}20\%}}{f_{\mathrm{r}20\%}} \times 100\% \tag{4.8}$$

where the percentage subscript of f_r denotes the humidity level where it was measured at. All the samples showed a similar decreasing trend as the humidity level increased, with the largest reduction in frequency occurring between 70% and 90%RH. As seen from Table 4.2, the humidity sensitivity (S) increased as the finger number (N_f) of the IDC increased, and also increased as the spatial wavelength of the IDC (defined as $2(W_\mathrm{g} + g)$) decreased. The variation trend of the frequency agreed with what the analytical model of the IDCs predicted. But the influence of the spatial wavelength on the sensitivity was not as significant as the analytical

Table 4.2: Comparison of Different Design Dimensions of IDCs

Design	Dimensions	$f_{r20\%}$	$f_{r90\%}$	S (%)
Group 1				
A	N_f=40	214 MHz	183 MHz	14.5%
B	N_f=50	193 MHz	163 MHz	15.5%
C	N_f=60	177 MHz	148 MHz	16.4%
Group 2				
D	W_g=g=350 μm	251 MHz	211 MHz	15.9%
E	W_g=g=450 μm	263 MHz	222 MHz	15.6%
F	W_g=g=550 μm	260 MHz	221 MHz	15.0%

model predicted. As previously discussed in Chapter 2, the sensitivity was much more influenced by the water absorptive capacity of the substrate, equivalently, the variation ratio of the dielectric constant of the substrate, as seen from Table 4.1.

Chapter 5

Summary and Future Outlook

5.1 Thesis Summary

RFID sensor technology is a key enabler for the Internet of Things (IoT). Low cost, lightweight and flexibility are three requirements for the RFID sensor tag to provide ubiquitous intelligence in many application fields, for instance, intelligent packaging. This thesis explored printable chipless RFID sensor technologies as promising candidates to fulfill the above requirements. Multidisciplinary research was carried out covering material science, printing technology, and radio frequency engineering.

Multi-walled carbon nanotubes (MWCNTs) were studied as potential resistive-type sensing material for printable, flexible and high-performance humidity sensors. In contrast to as-received MWCNTs, MWCNTs functionalized using acid treatment (f-MWCNTs) exhibited significant sensitivity and fast response to the change of relative humidity (RH) level. The obtained resistance variation was up to 140% between 20% and 95% RH depending on the network density of the f-MWCNTs. The response time of the f-MWCNTs towards the increase of RH was less than 20 seconds. The f-MWCNTs also responded immediately to the decrease of RH. However, full recovery (i.e., full water desorption) of the f-MWCNTs unassisted from high RH to low RH would take around 2 hours. The major difference between the as-received and acid-treated MWCNTs was the presence of carboxylic acid groups in the f-MWCNTs identified by Raman and TGA characterization. Thus it is believed that hydrogen bonding between water molecules and the carboxylic acid groups was the main contributor to the significant increase in resistance of the f-MWCNTs at higher RH level. Such strong chemical water absorption in turn caused the long recovery time of the f-MWCNTs. The f-MWCNTs also demonstrated superior mechanical flexibility. The largest resistance variation of the f-MWCNTs resistors under tensile stress was less than 2% when the bending radius was as small as 3.5 mm. Additionally, their humidity sensitivity was almost insusceptible to either applied tensile stress or compressive stress.

Spray-coating was firstly employed to fabricate relatively uniform f-MWCNTs

films for material characterization. Later, an inkjet printing process was developed to fabricate thin films of the f-MWCNTs at a more controllable and cost-effective way. Using ethylene glycol as the main solvent, a stable f-MWCNTs ink was formulated, and reliable jetting behavior was obtained using a Fujifilm Dimatix piezoelectric inkjet printer. The printed films were more homogeneous than the spray-coated ones, although accumulation of nanotubes was still observed in some places. It was observed that both sheet resistance and humidity-sensitivity of the f-MWCNTs films decreased when the films were annealed at higher temperatures. The degraded humidity-sensitivity could be explained by the decomposition of the carboxylic acid groups starting at 150 °C, suggesting it is best to keep the process temperature of the f-MWCNTs below 150 °C.

A flexible humidity sensor based on backscatter modulation was demonstrated by applying the f-MWCNTs. The backscattered power from the sensor was modulated by the resistance of the f-MWCNTs resistor, i.e. the ambient humidity level. It was found that the parasitic capacitance in the f-MWCNTs resistor strongly affected the sensor response, particularly, the operating frequency range. The sensor was then optimized by adjusting the parasitic capacitance, thereby being capable of distinguishing from 30% to 90% RH over the frequency range from 40 kHz to 2 GHz. With the integration of a proper antenna, this sensor could be used together with a chipless RFID tag based on either backscatter modulation or frequency-spectrum signature to construct a complete chipless RFID sensor tag.

A printed and flexible chipless RFID humidity sensor tag based on time-domain reflectometry (TDR) was also demonstrated by applying the f-MWCNTs. This tag encoded ID in the delay time between the structural-mode and the antenna-mode scattering pulse. The humidity sensing was performed by monitoring the antenna-mode pulse, as the pulse amplitude (or energy) was modulated by the resistance of the f-MWCNTs. The sensor tag could measure the humidity change from 30% to 90% RH. In addition, a multi-parameter sensor based on TDR was proposed. The sensor concept was proven by theoretical analysis and circuit simulation. However, implementation challenges exist mainly due to the considerable loss of signal strength caused by long transmission lines and impedance mismatch.

Compared with the above two chipless RFID sensor principles, the frequency-spectrum signature principle has many advantages such as high coding capacity, compact size, immunity to noise, insusceptibility to process variation, and adaptivity to multi-parameter monitoring. Therefore, a printed chipless RFID humidity sensor tag based on LC resonators was proposed for short-range identification and sensing applications. The tag encoded the ID and sensor information in the resonant frequency of an LC resonator respectively. Moreover, paper was proposed to serve as sensing substrate, which would merge the manufacturing of the tag into the production of traditional packages.

Besides the commonly-used inkjet (photo) paper, commercial packaging papers of lower cost and more robustness were also studied. Firstly, it was found that the print quality and the electrical performance of inkjet-printed metal conductors strongly depended on the surface properties of the paper substrate. Among three

types of packaging paper, only the UV-coated one showed the potential for printed electronics. In fact, the sheet resistance obtained from the UV-coated packaging paper was about 10 times higher than that from the inkjet papers when the papers were all sintered at 100 °C. However, as the packaging paper was more resistant to heat, the printed metal conductors thereon could be sintered at up to 200 °C so that their sheet resistance was substantially reduced to 0.05 Ω/sq. This resistance value was close to what was obtained from the PEL inkjet paper sintered at 150 °C. Moreover, the printed conductors on the UV-coated packaging paper were more reliable than those on the inkjet paper when they were exposed to harsh environmental conditions for 6 weeks. Furthermore, the mechanical flexibility of paper substrates was evaluated. The results suggested the bending radius of the inkjet-printed conductors on the paper substrate should be kept below 10 mm under compressive stress or below 20 mm under tensile stress.

Regarding the sensing performance, LC resonators printed on paper substrates showed a very high sensitivity in terms of resonant frequency variation up to 16.6% between 20% and 90% RH. The LC resonator on the UV-coated packaging paper exhibited even higher sensitivity than those on the inkjet papers over the humidity range from 20% to 70% RH, showing the great potential of the ordinary packaging paper for cheap and flexible humidity sensor applications. The response time of the LC resonators on paper substrates was around 6 minutes, partially due to the slow response (around 4 to 6 minutes) of the environmental chamber used in the test. It also took a long time for the paper substrates to desorb all the water molecules. In spite of their long recovery time, the paper-based and the f-MWCNTs-based humidity sensors as presented in this thesis could find applications where the humidity level changes gradually and slowly, such as environmental monitoring. In applications where faster recovery time is required, an embedded heater or other solutions should be considered.

5.2 Future work

Some potential future work is suggested as follows,

- The f-MWCNTs ink formulation is not yet ideal for the Dimatix inkjet printer as its surface tension is still higher than the optimal value. Other solvents with lower surface tension could be tested. In addition, the coffee-ring effect was observed in the printed f-MWCNTs films. It would be expected that a more homogeneous film of the f-MWNCTs would exhibit even higher sensitivity and better reproducibility. One way to improve the film uniformity is to increase the substrate temperature [140]. Another way is to use two mixed solvents with different surface tension and boiling points, which induces an inward Marangoni flow [149]. The combination of the above two methods is worth investigating.

- Considerable signal attenuation along the inkjet-printed transmission lines leads to challenging implementation of the TDR-based multi-parameter sensor. It would also impose limits on the coding capacity of the time-coded RFID sensor tag. Besides the intrinsically limited conductivity, the low thickness of inkjet-printed metal conductors is another main reason for the signal attenuation. One solution is to overprint the transmission lines for many times [98], which is however not economical for many applications. An economical solution is to employ the printing method using variable thickness. In this method, the transmission lines are printed in a fashion that only the area where highest current density occurs is thickened [217]. Moreover, Shao et al. applied a linear-tapering microstrip line to compensate the accumulated resistance along the line [103]. This tapering technique is also worth investigating for the sensor tag implementation.

- PET and paper substrate were used for the RFID resonator and sensor resonator respectively. The separate production of the two resonators would inevitably increase the cost and process steps. It is desired that the RFID resonator can be directly fabricated on paper substrates but without being interfered by the fluctuations of ambient humidity level. One potential solution is to print a humidity-insensitive dielectric layer below the interdigital capacitor area to shield the influence of the paper on the resonant frequency of the RFID resonator.

Bibliography

[1] L. Atzori, A. Iera, and G. Morabito, "The Internet of Things: A survey," *Computer Networks*, vol. 54, pp. 2787–2805, Oct 2010.

[2] G. Kortuem, F. Kawsar, D. Fitton, and V. Sundramoorthy, "Smart objects as building blocks for the Internet of things," *IEEE Internet Computing*, vol. 14, pp. 44–51, Jan 2010.

[3] J. Ma, L. Yang, B. Apduhan, R. Huang, L. Barolli, M. Takizawa, and T. Shih, "A walkthrough from smart spaces to smart hyperspaces towards a smart world with ubiquitous intelligence," in *Proceedings of 11th International Conference on Parallel and Distributed Systems, vol I*, pp. 370–376, Jul 2005.

[4] S. Jankowski, "The sectors where the Internet of Things really matters." https://hbr.org/2014/10/the-sectors-where-the-internet-of-things-really-matters, 2014. (Last accessed: 2015-03-11).

[5] P. Bulter, "Smart packaging - intelligent packaging for food, beverage, pharmaceuticals and household products," *Materials World*, vol. 9, pp. 11–13, Mar 2001.

[6] A. L. Brody, B. Bugusu, J. H. Han, C. K. Sand, and T. H. Mchugh, "Innovative food packaging solutions," *Journal of Food Science*, vol. 73, pp. R107–R116, Oct 2008.

[7] K. Yam, P. Takhistov, and J. Miltz, "Intelligent packaging: Concepts and applications," *Journal of Food Science*, vol. 70, pp. R1–R10, Jan-Feb 2005.

[8] "The advanced packaging solutions market value for 2017 is projected to be nearly $44.3 billion." http://www.bccresearch.com/pressroom/fod/advanced-packaging-solutions-market-value-projected-nearly-$44.3-billion-2017. (Last accessed: 2015-03-11).

[9] "Active, Controlled, and Intelligent Packaging for Foods and Beverages." http://www.bccresearch.com/market-research/food-and-beverage/food-beverage-packaging-fod038c.html. (Last accessed: 2015-03-11).

[10] "Active & Intelligent Packaging." http://www.marketresearch.com/Freedonia-Group-Inc-v1247/Active-Intelligent-Packaging-7979079/. (Last accessed: 2015-03-11).

[11] Y. Zhan, Y. Mei, and L. Zheng, "Materials capability and device performance in flexible electronics for the Internet of Things," *Journal of Materials Chemistry C*, vol. 2, pp. 1220–1232, Feb 2014.

[12] L.-R. Zheng, M. B. Nejad, S. Rodriguez, L. Zhang, C. Chen, and H. Tenhunen, "System-on-flexible-substrates: Electronics for future smart-intelligent world," in *Proceedingsof 2006 Conference on High Density Microsystem Design and Packaging and Component Failure Analysis (HDP '06)*, pp. 233–240, Jun 2006.

[13] F. P. Wieringa, G. T. van Heck, P. Rensing, M. M. Koetse, S. S. Kalisingh, and H. Schoo, "Systems in foil - Opening new perspectives in medical technology," in *4th European Conference of The International Federation for Medical and Biological Engineering*, vol. 22, pp. 2292–2295, Nov 2009.

[14] L. Yang, R. Zhang, D. Staiculescu, C. P. Wong, and M. M. Tentzeris, "A novel conformal RFID-enabled module utilizing inkjet-printed antennas and carbon nanotubes for gas-detection applications," *IEEE Antennas and Wireless Propagation Letters*, vol. 8, pp. 653–656, May 2009.

[15] G. Yang, J. Chen, L. Xie, J. Mao, H. Tenhunen, and L.-R. Zheng, "A hybrid low power biopatch for body surface potential measurement," *IEEE Journal of Biomedical and Health Informatics*, vol. 17, pp. 591–599, May 2013.

[16] H. Z. Raghu Das, "Smart packaging comes to market: brand enhancement with electronics 2013-2023," tech. rep., IDTechEx, 2013.

[17] C. E. Realini and B. Marcos, "Active and intelligent packaging systems for a modern society," *Meat Science*, vol. 98, pp. 404–419, Nov 2014.

[18] M. Vanderroost, P. Ragaert, F. Devlieghere, and B. De Meulenaer, "Intelligent food packaging: The next generation," *Trends in Food Science & Technology*, vol. 39, pp. 47–62, Sep 2014.

[19] P. Heljo, C. Schmidt, R. Klengel, H. Majumdar, and D. Lupo, "Electrical and thermal analysis of frequency dependent filamentary switching in printed rectifying diodes," *Organic Electronics*, vol. 20, pp. 69 – 75, May 2015.

[20] H. Sirringhaus, T. Kawase, R. Friend, T. Shimoda, M. Inbasekaran, W. Wu, and E. Woo, "High-resolution inkjet printing of all-polymer transistor circuits," *Science*, vol. 290, pp. 2123–2126, Dec 2000.

[21] P. Andersson, D. Nilsson, P. Svensson, M. Chen, A. Malmström, T. Remonen, T. Kugler, and M. Berggren, "Active matrix displays based on all-organic electrochemical smart pixels printed on paper," *Advanced Materials*, vol. 14, pp. 1460–1464, Oct 2002.

[22] A. M. Gaikwad, G. L. Whiting, D. A. Steingart, and A. C. Arias, "Highly flexible, printed alkaline batteries based on mesh-embedded electrodes," *Advanced Materials*, vol. 23, pp. 3251–3255, Aug 2011.

[23] J.-A. Jeong, J. Lee, H. Kim, H.-K. Kim, and S.-I. Na, "Ink-jet printed transparent electrode using nano-size indium tin oxide particles for organic photovoltaics," *Solar Energy Materials and Solar Cells*, vol. 94, pp. 1840–1844, Oct 2010.

[24] Y. Amin, Q. Chen, H. Tenhunen, and L.-R. Zheng, "Evolutionary versatile printable RFID antennas for "green" electronics," *Jouranl of Electromagnetic Waves and Applications*, vol. 26, pp. 264–273, Apr 2012.

[25] V. Dua, S. P. Surwade, S. Ammu, S. R. Agnihotra, S. Jain, K. E. Roberts, S. Park, R. S. Ruoff, and S. K. Manohar, "All-organic vapor sensor using inkjet-printed reduced graphene oxide," *Angewandte Chemie-International Edition*, vol. 49, pp. 2154–2157, Mar 2010.

[26] M. Hambsch, K. Reuter, M. Stanel, G. Schmidt, H. Kempa, U. Füegmann, U. Hahn, and A. C. Hüebler, "Uniformity of fully gravure printed organic field-effect transistors," *Materials Science and Engineering B-Advanced Functional Solid-state Materials*, vol. 170, pp. 93–98, Jun 2010.

[27] D. Tobjörk and R. Österbacka, "Paper electronics," *Advanced Materials*, vol. 23, pp. 1935–1961, May 2011.

[28] "Aersol Jet Technology." http://www.optomec.com/additive-manufacturing/printed-electronics/aerosol-jet-technology/. (Last accessed: 2015-03-11).

[29] T. S. Lopez, D. C. Ranasinghe, M. Harrison, and D. McFarlane, "Adding sense to the Internet of Things," *Personal and Ubiquitous Computing*, vol. 16, pp. 291–308, Mar 2012.

[30] Z. Zou, Q. Chen, I. Uysal, and L. Zheng, "Radio frequency identification enabled wireless sensing for intelligent food logistics," *Philosophical Transactions of Thee Royal Soceity A-Mathematical Physical and Engineering Sciences*, vol. 372, Jun 2014.

[31] V. Chawla and D. S. Ha, "An overview of passive RFID," *IEEE Communications Magazine*, vol. 45, pp. 11–17, Sep 2007.

[32] D. Restuccia, U. G. Spizzirri, O. I. Parisi, G. Cirillo, M. Curcio, F. Iemma, F. Puoci, G. Vinci, and N. Picci, "New EU regulation aspects and global market of active and intelligent packaging for food industry applications," *Food Control*, vol. 21, pp. 1425–1435, Nov 2010.

[33] Z. Chen and C. Lu, "Humidity sensors: A review of materials and mechanisms," *Sensor Letters*, vol. 3, pp. 274–295, Dec 2005.

[34] D. Bridgeman, J. Corral, A. Quach, X. Xian, and E. Forzani, "Colorimetric humidity sensor based on liquid composite materials for the monitoring of food and pharmaceuticals," *Langmuir*, vol. 30, pp. 10785–10791, Sep 2014.

[35] M. Mäntysalo, L. Xie, F. Jonsson, Y. Feng, A. L. Cabezas, and L.-R. Zheng, "System integration of smart packages using printed electronics," in *2012 IEEE 62nd Electronic Components and Technology Conference (ECTC)*, pp. 997–1002, May-Jun 2012.

[36] P. H. Raghu Das, "Printed and chipless RFID forecasts, technologies & players 2009-2019," tech. rep., IDTechEx, 2010.

[37] M. Singh, H. M. Haverinen, P. Dhagat, and G. E. Jabbour, "Inkjet printing-Process and its applications," *Advanced Materials*, vol. 22, pp. 673–685, Feb 2010.

[38] P.-G. Su and C.-S. Wang, "Novel flexible resistive-type humidity sensor," *Sensors and Actuators B-Chemical*, vol. 123, pp. 1071–1076, May 2007.

[39] P. Harrey, B. Ramsey, P. Evans, and D. Harrison, "Capacitive-type humidity sensors fabricated using the offset lithographic printing process," *Sensors and Actuators B-Chemical*, vol. 87, pp. 226–232, Dec 2002.

[40] J. Huang, C.-a. Tao, Q. An, C. Lin, X. Li, D. Xu, Y. Wu, X. Li, D. Shen, and G. Li, "Visual indication of enviromental humidity by using poly(ionic liquid) photonic crystals," *Chemical Communications*, vol. 46, pp. 4103–4105, May 2010.

[41] F. Pascal-Delannoy, B. Sorli, and A. Boyer, "Quartz Crystal Microbalance (QCM) used as humidity sensor," *Sensors and Actuators A-Physical*, vol. 84, pp. 285–291, Sep 2000.

[42] H. Farahani, R. Wagiran, and M. N. Hamidon, "Humidity sensors principle, mechanism, and fabrication technologies: A comprehensive review," *Sensors*, vol. 14, pp. 7881–7939, May 2014.

[43] D. Roveti and K. Soleyn, "A review of humidity sensors," *Measurement Control*, vol. 193, pp. 105–110, 1999.

[44] A. Rivadeneyra, J. Fernández-Salmerón, M. Agudo, J. A. López-Villanueva, L. Fermin Capitan-Vallvey, and A. J. Palma, "Design and characterization of a low thermal drift capacitive humidity sensor by inkjet-printing," *Sensors and Actuators B-Chemical*, vol. 195, pp. 123–131, May 2014.

[45] Z. Rittersma, "Recent achievements in miniaturised humidity sensors - a review of transduction techniques," *Sensors and Actuators A-Physical*, vol. 96, pp. 196–210, Feb 2002.

[46] B. M. Kulwick, "Humidity sensors," *Journal of the American Chemical Society*, vol. 74, pp. 697–708, Apr 1991.

[47] A. S. G. Reddy, B. B. Narakathu, M. Z. Atashbar, M. Rebros, E. Rebrosova, B. J. Bazuin, M. K. Joyce, P. D. Fleming, and A. Pekarovicova, "Printed capacitive based humidity sensors on flexible substrates," *Sensor Letters*, vol. 9, pp. 869–871, Apr 2011.

[48] D. R. Kauffman and A. Star, "Carbon nanotube gas and vapor sensors," *Angewandte Chemie-International Edition*, vol. 47, pp. 6550–6570, Aug 2008.

[49] M. F. L. De Volder, S. H. Tawfick, R. H. Baughman, and A. J. Hart, "Carbon nanotubes: Present and future commercial applications," *Science*, vol. 339, pp. 535–539, Feb 2013.

[50] S. Iijima, "Helical microtubules of graphitic carbon," *Nature*, vol. 354, pp. 56–58, Nov 1991.

[51] M. D. R. Saito, G. Dresselhaus, *Physical properties of carbon nanotubes.* Imperial College Press, 1998.

[52] M. F. Yu, O Lourie, M. J. Dyer, K Moloni, T. F. Kelly, R. S. Ruoff, "Strength and breaking mechanism of multiwalled carbon nanotubes under tensile load," *Science*, vol. 287, pp. 637–640, Jan 2000.

[53] B. Peng, M. Locascio, P. Zapol, S. Li, S. L. Mielke, G. C. Schatz, and H. D. Espinosa, "Measurements of near-ultimate strength for multiwalled carbon nanotubes and irradiation-induced crosslinking improvements," *Nature Nanotechnology*, vol. 3, pp. 626–631, Oct 2008.

[54] P. Kim, L. Shi, A. Majumdar, and P. McEuen, "Thermal transport measurements of individual multiwalled nanotubes," *Physical Review Letters*, vol. 87, Nov 2001.

[55] B. Wei, R. Vajtai, and P. Ajayan, "Reliability and current carrying capacity of carbon nanotubes," *Applied Physics Letters*, vol. 79, pp. 1172–1174, Aug 2001.

[56] B. L. Allen, P. D. Kichambare, and A. Star, "Carbon nanotube field-effect-transistor-based biosensors," *Advanced Materials*, vol. 19, pp. 1439–1451, Jun 2007.

[57] B. Mahar, C. Laslau, R. Yip, and Y. Sun, "Development of carbon nanotube-based sensors - A review," *IEEE Sensors Journal*, vol. 7, pp. 266–284, Jan-Feb 2007.

[58] Y. Zhang, Y. Bai, and B. Yan, "Functionalized carbon nanotubes for potential medicinal applications," *Drug Discovery Today*, vol. 15, pp. 428–435, Jun 2010.

[59] D. W. H. Fam, A. Palaniappan, A. I. Y. Tok, B. Liedberg, and S. M. Moochhala, "A review on technological aspects influencing commercialization of carbon nanotube sensors," *Sensors and Actuators B-Chemical*, vol. 157, pp. 1–7, Sep 2011.

[60] P. Bondavalli, P. Legagneux, and D. Pribat, "Carbon nanotubes based transistors as gas sensors: State of the art and critical review," *Sensors and Actuators B-Chemical*, vol. 140, pp. 304–318, Jun 2009.

[61] B. Hu, W. Chen, and J. Zhou, "High performance flexible sensor based on inorganic nanomaterials," *Sensors and Actuators B-Chemical*, vol. 176, pp. 522–533, Jan 2013.

[62] E. Llobet, "Gas sensors using carbon nanomaterials: A review," *Sensors and Actuators B-Chemical*, vol. 179, pp. 32–45, Mar 2013.

[63] E. S. Snow, F. K. Perkins, and J. A. Robinson, "Chemical vapor detection using single-walled carbon nanotubes," *Chemical Society Reviews*, vol. 35, pp. 790–798, May 2006.

[64] Q. Cao and J. A. Rogers, "Ultrathin films of single-walled carbon nanotubes for electronics and sensors: A review of fundamental and applied aspects," *Advanced Materials*, vol. 21, pp. 29–53, Jan 2009.

[65] Q. Pengfei, O. Vermesh, M. Grecu, A. Javey, O. Wang, H. Dai, S. Peng, and K. Cho, "Toward large arrays of multiplex functionalized carbon nanotube sensors for highly sensitive and selective molecular detection," *Nano Letters*, vol. 3, pp. 347–351, Mar 2003.

[66] J. Kong, M. Chapline, and H. Dai, "Functionalized carbon nanotubes for molecular hydrogen sensors," *Advanced Materials*, vol. 13, pp. 1384–1386, Sep 2001.

[67] R. Leghrib, R. Pavelko, A. Felten, A. Vasiliev, C. Cané, I. Gracia, J.-J. Pireaux, and E. Llobet, "Gas sensors based on multiwall carbon nanotubes decorated with tin oxide nanoclusters," *Sensors and Actuators B-Chemical*, vol. 145, pp. 411–416, Mar 2010.

[68] C. Staii and A. Johnson, "DNA-decorated carbon nanotubes for chemical sensing," *Nano Letters*, vol. 5, pp. 1774–1778, Sep 2005.

[69] P. Bondavalli, P. Legagneux, D. Pribat, A. Balan, and S. Nazeer, "Gas fingerprinting using carbon nanotubes transistor arrays," *Journal of Experimental Nanoscience*, vol. 3, no. 4, pp. 347–356, 2008.

[70] A. Goldoni, L. Petaccia, S. Lizzit, and R. Larciprete, "Sensing gases with carbon nanotubes: a review of the actual situation," *Journal of Physics-Condensed Matter*, vol. 22, Jan 2010.

[71] J. Li, Y. Lu, Q. Ye, M. Cinke, J. Han, and M. Meyyappan, "Carbon nanotube sensors for gas and organic vapor detection," *Nano Letters*, vol. 3, pp. 929–933, Jul 2003.

[72] J. Li, Y. Lu, Q. Ye, L. Delzeit, and M. Meyyappan, "A gas sensor array using carbon nanotubes and microfabrication technology," *Electrochemical and Solid State Letters*, vol. 8, no. 11, pp. H100–H102, 2005.

[73] J. Novak, E. Snow, E. Houser, D. Park, J. Stepnowski, and R. McGill, "Nerve agent detection using networks of single-walled carbon nanotubes," *Applied Physics Letters*, vol. 83, pp. 4026–4028, Nov 2003.

[74] Y. W. Chang, J. S. Oh, S. H. Yoo, H. H. Choi, and K.-H. Yoo, "Electrically refreshable carbon-nanotube-based gas sensors," *Nanotechnology*, vol. 18, Oct 2007.

[75] C. Barner-Kowollik, ed., *Handbook of RAFT Polymerization*. WILEY-VCH, 2008.

[76] Y. Sun, K. Fu, Y. Lin, and W. Huang, "Functionalized carbon nanotubes: Properties and applications," *Accounts of Chemical Resarch*, vol. 35, pp. 1096–1104, Dec 2002.

[77] J. Yu, N. Grossiord, C. E. Koning, and J. Loos, "Controlling the dispersion of multi-wall carbon nanotubes in aqueous surfactant solution," *Carbon*, vol. 45, pp. 618–623, Mar 2007.

[78] A. L. Cabezas, Y. Feng, L.-R. Zheng, and Z.-B. Zhang, "Thermal ageing of electrical conductivity in carbon nanotube/polyaniline composite films," *Carbon*, vol. 59, pp. 270–277, Aug 2013.

[79] K. Balasubramanian and M. Burghard, "Chemically functionalized carbon nanotubes," *Small*, vol. 1, pp. 180–192, Feb 2005.

[80] A. Eitan, K. Jiang, D. Dukes, R. Andrews, and L. Schadler, "Surface modification of multiwalled carbon nanotubes: Toward the tailoring of the interface in polymer composites," *Chemstry of Materials*, vol. 15, pp. 3198–3201, Aug 2003.

[81] S. Banerjee, T. Hemraj-Benny, and S. Wong, "Covalent surface chemistry of single-walled carbon nanotubes," *Advanced Materials*, vol. 17, pp. 17–29, Jan 2005.

[82] J. Liu, A. Rinzler, H. Dai, J. Hafner, R. Bradley, P. Boul, A. Lu, T. Iverson, K. Shelimov, C. Huffman, F. Rodriguez-Macias, Y. Shon, T. Lee, D. Colbert, and R. Smalley, "Fullerene pipes," *Science*, vol. 280, pp. 1253–1256, May 1998.

[83] V. Datsyuk, M. Kalyva, K. Papagelis, J. Parthenios, D. Tasis, A. Siokou, I. Kallitsis, and C. Galiotis, "Chemical oxidation of multiwalled carbon nanotubes," *Carbon*, vol. 46, pp. 833–840, May 2008.

[84] K. A. Wepasnick, B. A. Smith, K. E. Schrote, H. K. Wilson, S. R. Diegelmann, and D. H. Fairbrother, "Surface and structural characterization of multi-walled carbon nanotubes following different oxidative treatments," *Carbon*, vol. 49, pp. 24–36, Jan 2011.

[85] M. Martínez, M. Callejas, A. Benito, M. Cochet, T. Seeger, A. Anson, J. Schreiber, C. Gordon, C. Marhic, O. Chauvet, and W. Maser, "Modifications of single-wall carbon nanotubes upon oxidative purification treatments," *Nanotechnology*, vol. 14, pp. 691–695, Jul 2003.

[86] K. Balasubramanian and M. Burghard, "Electrochemically functionalized carbon nanotubes for device applications," *Journal of Materials Chemistry*, vol. 18, no. 26, pp. 3071–3083, 2008.

[87] P. C. P. Watts, N. Mureau, Z. Tang, Y. Miyajima, J. D. Carey, and S. R. P. Silva, "The importance of oxygen-containing defects on carbon nanotubes for the detection of polar and non-polar vapours through hydrogen bond formation," *Nanotechnology*, vol. 18, May 2007.

[88] X. Huang, Y. Sun, L. Wang, F. Meng, and J. Liu, "Carboxylation multi-walled carbon nanotubes modified with LiClO4 for water vapour detection," *Nanotechnology*, vol. 15, pp. 1284–1288, Sep 2004.

[89] P.-G. Su and C.-S. Wang, "In situ synthesized composite thin films of MWCNTs/PMMA doped with KOH as a resistive humidity sensor," *Sensors and Actuators B-Chemical*, vol. 124, pp. 303–308, Jun 2007.

[90] L. Liu, X. Ye, K. Wu, R. Han, Z. Zhou, and T. Cui, "Humidity sensitivity of multi-walled carbon nanotube networks deposited by dielectrophoresis," *Sensors*, vol. 9, pp. 1714–1721, Mar 2009.

[91] K.-P. Yoo, L.-T. Lim, N.-K. Min, M. J. Lee, C. J. Lee, and C.-W. Park, "Novel resistive-type humidity sensor based on multiwall carbon nanotube/polyimide composite films," *Sensors and Actuators B-Chemical*, vol. 145, pp. 120–125, Mar 2010.

[92] C. L. Cao, C. G. Hu, L. Fang, S. X. Wang, Y. S. Tian, and C. Y. Pan, "Humidity sensor based on multi-walled carbon nanotube thin films," *Journal of Nanomaterials*, 2011.

[93] Q.-Y. Tang, Y. C. Chan, and K. Zhang, "Fast response resistive humidity sensitivity of polyimide/multiwall carbon nanotube composite films," *Sensors and Actuators B-Chemical*, vol. 152, pp. 99–106, Feb 2011.

[94] L. Liu, X. Ye, K. Wu, Z. Zhou, D. Lee, and T. Cui, "Humidity sensitivity of carbon nanotube and poly (dimethyldiallylammonium chloride) composite films," *IEEE Sensors Journal*, vol. 9, pp. 1308–1314, Oct 2009.

[95] J. T. H. Tsai, C.-C. Lu, and J. G. Li, "Fabrication of humidity sensors by multi-walled carbon nanotubes," *Journal of Experimental Nanoscience*, vol. 5, no. 4, pp. 302–309, 2010.

[96] H. Yu, T. Cao, L. Zhou, E. Gu, D. Yu, and D. Jiang, "Layer-by-layer assembly and humidity sensitive behavior of poly(ethyleneimine)/multiwall carbon nanotube composite films," *Sensors and Actuators B-Chemical*, vol. 119, pp. 512–515, Dec 2006.

[97] M. Xu, Z. Sun, Q. Chen, and B. K. Tay, "Effect of chemical oxidation on the gas sensing properties of multi-walled carbon nanotubes," *Internal Journal of Nanotechnology*, vol. 6, no. 7-8, pp. 735–744, 2009.

[98] L. Yang, A. Rida, R. Vyas, and M. M. Tentzeris, "RFID tag and RF structures on a paper substrate using inkjet-printing technology," *IEEE Transactions on Microwave Theory and Techniques*, vol. 55, pp. 2894–2901, Dec 2007.

[99] F. Eder, H. Klauk, M. Halik, U. Zschieschang, G. Schmid, and C. Dehm, "Organic electronics on paper," *Applied Physics Letters*, vol. 84, pp. 2673–2675, Apr 2004.

[100] R. Bollström, A. Määttänen, D. Tobjörk, P. Ihalainen, N. Kaihovirta, R. Österbacka, J. Peltonen, and M. Toivakka, "A multilayer coated fiber-based substrate suitable for printed functionality," *Organic Electronics*, vol. 10, pp. 1020–1023, Aug 2009.

[101] A. Mihranyan, L. Nyholm, A. E. G. Bennett, and M. Stromme, "Novel high specific surface area conducting paper material composed of polypyrrole and Cladophora cellulose," *Journal of Physical Chemistry B*, vol. 112, pp. 12249–12255, Oct 2008.

[102] Y. Amin, Q. Chen, H. Tenhunen, and L.-R. Zheng, "Performance-optimized quadrate bowtie RFID antennas for cost-effective and eco-friendly industrial applications," *Progress in Electromagnetics Research Letters*, vol. 126, pp. 49–64, 2012.

[103] B. Shao, Q. Chen, Y. Amin, D. Mendoza, R. Liu, and L.-R. Zheng, "An ultra-low-cost RFID tag with 1.67 Gbps data rate by ink-jet printing on paper substrate," in *IEEE Asian Solid State Circuits Conference (A-SSCC) 2010*, pp. 1–4, Nov 2010.

[104] V. Lakafosis, A. Rida, R. Vyas, L. Yang, S. Nikolaou, and M. Tentzeris, "Progress towards the first wireless sensor networks consisting of inkjet-printed, paper-based RFID-enabled sensor tags," *Proceedings of the IEEE*, vol. 98, pp. 1601–1609, Sep 2010.

[105] G. Yang, L. Xie, M. Mantysalo, J. Chen, H. Tenhunen, and L.-R. Zheng, "Bio-patch design and implementation based on a low-power system-on-chip and paper-based inkjet printing technology," *IEEE Transactions on Information Technology in Biomedicine*, vol. 16, pp. 1043–1050, Nov 2012.

[106] T. Öhlund, J. Örtegren, S. Forsberg, and H.-E. Nilsson, "Paper surfaces for metal nanoparticle inkjet printing," *Applied Surface Science*, vol. 259, pp. 731–739, Oct 2012.

[107] P. A. Larsson, M. Gimåker, and L. Wågberg, "The influence of periodate oxidation on the moisture sorptivity and dimensional stability of paper," *Cellulose*, vol. 15, pp. 837–847, Dec 2008.

[108] S. Simula and K. Niskanen, "Electrical properties of viscose-kraft fibre mixtures," *Nordic Pulp & Paper Research Journal*, vol. 14, pp. 243–246, Sep 1999.

[109] M. Uematsu and E. Franck, "Static dieletric-constant of water and steam," *Journal of Physical and Chemical Reference Data*, vol. 9, no. 4, pp. 1291–1306, 1980.

[110] E. L. Tan, W. N. Ng, R. Shao, B. D. Pereles, and K. G. Ong, "A wireless, passive sensor for quantifying packaged food quality," *Sensors*, vol. 7, pp. 1747–1756, Sep 2007.

[111] M. Mraović, T. Muck, M. Pivar, J. Trontelj, and A. Pleteršek, "Humidity sensors printed on recycled paper and ardboard," *Sensors*, vol. 14, pp. 13628–13643, Aug 2014.

[112] W.A. Davis and K. Agarwal, ed., *Radio Frequency Circuit Design*. John Wiley and Sons, 2001.

[113] Y. Sakai, Y. Sadaoka, and M. Matsuguchi, "Humidity sensors based on polymer thin films," *Sensors and Actuators B-Chemical*, vol. 35, pp. 85–90, Sep 1996.

[114] R. Igreja and C. Dias, "Dielectric response of interdigital chemocapacitors: The role of the sensitive layer thickness," *Sensors and Actuators B-Chemical*, vol. 115, pp. 69–78, May 2006.

[115] DuPont, *Summary of Properties for Kapton ®Polyimide Films*, 2012.

[116] J. Virtanen, L. Ukkonen, T. Björninen, A. Z. Elsherbeni, and L. Sydäsnheimo, "Inkjet-printed humidity sensor for passive UHF RFID systems," *IEEE Transactions on Instrumentation and Measurement*, vol. 60, pp. 2768–2777, Aug 2011.

[117] E. Tekin, P. J. Smith, and U. S. Schubert, "Inkjet printing as a deposition and patterning tool for polymers and inorganic particles," *Soft Matter*, vol. 4, no. 4, pp. 703–713, 2008.

[118] *Industrial Inkjet For Dummies, Xaar Special Edition*. Wiley Publishing Inc., 2010.

[119] B. Derby, "Inkjet printing of functional and structural materials: Fluid property requirements, feature stability, and resolution," in *Annual Review of Materials Resarch*, vol. 40, pp. 395–414, 2010.

[120] J. Brünahl and A. Grishin, "Piezoelectric shear mode drop-on-demand inkjet actuator," *Sensors and Actuators A-Physical*, vol. 101, pp. 371–382, Oct 2002.

[121] H. Sirringhaus and T. Shimoda, "Inkjet printing of functional materials," *MRS Bulletin*, vol. 28, pp. 802–803, Nov 2003.

[122] P. Calvert, "Inkjet printing for materials and devices," *Chemstry of Materials*, vol. 13, pp. 3299–3305, Oct 2001.

[123] H. Lee, K. Chou, and K. Huang, "Inkjet printing of nanosized silver colloids," *Nanotechnology*, vol. 16, pp. 2436–2441, Oct 2005.

[124] J. E. Fromm, "Numerical calculation of the fluid dynamics of drop-on-demand jets," *IBM Journal of Research and Development*, vol. 28, pp. 322–333, May 1984.

[125] "Ohnesorge Number," in *Encyclopedia of Microfluidics and Nanofluidics* (Li, Dongqing, ed.), pp. 1513–1513, Springer US, 2008.

[126] K. A. M. Seerden, N. Reis, J. R. G. Evans, P. S. Grant, J. W. Halloran and B. Derby, "Ink-jet printing of wax-based alumina suspensions," *Journal of the American Ceramic Society*, vol. 84, pp. 2514–2520, Nov 2001.

[127] FUJIFILM Dimatix, Inc., Santa Clara, CA, *Dimatix Materials Printer DMP-2800 Series User Manual*, 2007.

[128] K.-Y. Shin, S.-H. Lee, and J. H. Oh, "Solvent and substrate effects on inkjet-printed dots and lines of silver nanoparticle colloids," *Journal of Micromechanics and Microengineering*, vol. 21, Apr 2011.

[129] Y. Yuan and T. R. Lee, *Surface Science Techniques*, vol. 51, ch. Contact Angle and Wetting Properties, pp. 3–34. Springer-Verlag Berlin Heidelberg, 2013.

[130] S.-H. Lee, K.-Y. Shin, J. Y. Hwang, K. T. Kang, and H. S. Kang, "Silver inkjet printing with control of surface energy and substrate temperature," *Journal of Micromechanics and Microengineering*, vol. 18, Jul 2008.

[131] D. Vak, S.-S. Kim, J. Jo, S.-H. Oh, S.-I. Na, J. Kim, and D.-Y. Kim, "Fabrication of organic bulk heterojunction solar cells by a spray deposition method for low-cost power generation," *Applied Physics Letters*, vol. 91, Aug 2007.

[132] A. L.Cabezas, *Nanofribrillar materials for organic and printable electronics*. PhD thesis, KTH Royal Institute of Technology, 2013.

[133] K. Kordás, T. Mustonen, G. Tóth, H. Jantunen, M. Lajunen, C. Soldano, S. Talapatra, S. Kar, R. Vajtai, and P. M. Ajayan, "Inkjet printing of electrically conductive patterns of carbon nanotubes," *Small*, vol. 2, pp. 1021–1025, Aug 2006.

[134] W. R. Small and M. i. h. Panhuis, "Inkjet printing of transparent, electrically conducting single-waited carbon-nanotube composites," *Small*, vol. 3, pp. 1500–1503, Sep 2007.

[135] Y.-I. Lee, S. Kim, K.-J. Lee, N. V. Myung, and Y.-H. Choa, "Inkjet printed transparent conductive films using water-dispersible single-walled carbon nanotubes treated by UV/ozone irradiation," *Thin Solid Films*, vol. 536, pp. 160–165, Jun 2013.

[136] J. Li, T. Unander, A. L. Cabezas, B. Shao, Z. Liu, Y. Feng, E. B. Forsberg, Z.-B. Zhang, I. Jõgi, X. Gao, M. Boman, L.-R. Zheng, M. Östling, H.-E. Nilsson, and S.-L. Zhang, "Ink-jet printed thin-film transistors with carbon nanotube channels shaped in long strips," *Journal of Applied Physics*, vol. 109, Apr 2011.

[137] T. A. Elwi, H. M. Al-Rizzo, D. G. Rucker, E. Dervishi, Z. Li, and A. S. Biris, "Multi-walled carbon nanotube-based RF antennas," *Nanotechnology*, vol. 21, Jan 2010.

[138] A. R. Hopkins, D. C. Straw, and K. C. Spurrell, "Influence of surface chemistry on inkjet printed carbon nanotube films," *Thin Solid Films*, vol. 520, pp. 1541–1545, Dec 2011.

[139] A. Denneulin, J. Bras, A. Blayo, and C. Neuman, "Substrate pre-treatment of flexible material for printed electronics with carbon nanotube based ink," *Applied Surface Science*, vol. 257, pp. 3645–3651, Feb 2011.

[140] T. Wang, M. A. Roberts, I. A. Kinloch, and B. Derby, "Inkjet printed carbon nanotube networks: the influence of drop spacing and drying on electrical properties," *Journal of Physics D-Applied Physics*, vol. 45, Aug 2012.

[141] Z. Fan, T. Wei, G. Luo, and F. Wei, "Fabrication and characterization of multi-walled carbon nanotubes-based ink," *Journal of Materials Science*, vol. 40, pp. 5075–5077, Sep 2005.

[142] M. in het Panhuis, A. Heurtematte, W. R. Small and V. N. Paunov, "Inkjet printed water sensitive transparent films from natural gum-carbon nanotube composites," *Soft Matter*, vol. 3, no. 7, pp. 840–843, 2007.

[143] M. F. Mabrook, C. Pearson, A. S. Jombert, D. A. Zeze, and M. C. Petty, "The morphology, electrical conductivity and vapour sensing ability of inkjet-printed thin films of single-wall carbon nanotubes," *Carbon*, vol. 47, pp. 752–757, Mar 2009.

[144] A. Denneulin, J. Bras, F. Carcone, C. Neuman, and A. Blayo, "Impact of ink formulation on carbon nanotube network organization within inkjet printed conductive films," *Carbon*, vol. 49, pp. 2603 – 2614, Jul 2011.

[145] J. Kestin, H. E. Khalifa, H. Sookiazian and W. A. Wakeham, "Viscosity of liquid water in the range -8 °C to 150 °C," *Journal of Physical and Chemical Reference Data*, vol. 7, no. 3, pp. 941–948, 1978.

[146] N.B. Vargftik, B.N. Volkov, and L.D. Voljak, "International tables of the surface tension of water," *Journal of Physical and Chemical Reference Data*, vol. 12, no. 3, pp. 871–820, 1983.

[147] S.-J. Cho, T. Nguyen, and J.-H. Boo, "Polyimide surface modification by using microwave plasma for adhesion enhancement of Cu electroless plating," *Journal of Nanoscience and Nanotechnology*, vol. 11, pp. 5328–5333, Jun 2011.

[148] The MEGlobal Group of Companies, *Ethylene Glycol Product Guide*, 2008.

[149] J. Park and J. Moon, "Control of colloidal particle deposit patterns within picoliter droplets ejected by ink-jet printing," *Langmuir*, vol. 22, pp. 3506–3513, Apr 2006.

[150] R. Deegan, O. Bakajin, T. Dupont, G. Huber, S. Nagel, and T. Witten, "Capillary flow as the cause of ring stains from dried liquid drops," *Nature*, vol. 389, pp. 827–829, Oct 1997.

[151] G. Cummins and M. P. Y. Desmulliez, "Inkjet printing of conductive materials: a review," *Circuit World*, vol. 38, no. 4, pp. 193–213, 2012.

[152] "Conductive Polymer." http://www.heraeus-clevios.com/en/conductivepolymers/pedot-pss-conductive-polymers.aspx. (Last accessed: 2015-03-11).

[153] D. Tobjörk, H. Aarnio, P. Pulkkinen, R. Bollström, A. Määttänen, P. Ihalainen, T. Mäkelä, J. Peltonen, M. Toivakka, H. Tenhu, and R. Österbacka, "IR-sintering of ink-jet printed metal-nanoparticles on paper," *Thin Solid Films*, vol. 520, pp. 2949–2955, Jan 2012.

[154] A. Scandurra, G. F. Indelli, N. G. Spartà, F. Galliano, S. Ravesi, and S. Pignataro, "Low-temperature sintered conductive silver patterns obtained by inkjet printing for plastic electronics," *Surface and Interface analylsis*, vol. 42, pp. 1163–1167, Jun-Jul 2010.

[155] E. Halonen, T. Viiru, K. Östman, A. L. Cabezas, and M. Mäntysalo, "Oven sintering process optimization for inkjet-printed Ag nanoparticle ink," *IEEE Transactions on Components Packaging and Manufacturing Technology*, vol. 3, pp. 350–356, Feb 2013.

[156] J. Perelaer, M. Klokkenburg, C. E. Hendriks, and U. S. Schubert, "Microwave flash sintering of inkjet-printed silver tracks on polymer substrates," *Advanced Materials*, vol. 21, pp. 4830–4834, Dec 2009.

[157] J. Niittynen, R. Abbel, M. Mäntysalo, J. Perelaer, U. S. Schubert, and D. Lupo, "Alternative sintering methods compared to conventional thermal sintering for inkjet printed silver nanoparticle ink," *Thin Solid Films*, vol. 556, pp. 452 – 459, Apr 2014.

[158] M. L. Allen, M. Aronniemi, T. Mattila, A. Alastalo, K. Ojanperä, M. Suhonen, and H. Seppä, "Electrical sintering of nanoparticle structures," *Nanotechnology*, vol. 19, Apr 2008.

[159] W. Zapka, W. Voit, C. Loderer, and P. Lang, "Low temperature chemical post-treatment of inkjet printed nano-particle silver inks," in *Proceedings of NIP24: International Conference on Digital Printing Technologies and Digital Fabrication 2008*, pp. 906–911, Sep 2008.

[160] M. Allen, J. Leppäniemi, M. Vilkman, A. Alastalo, and T. Mattila, "Substrate-facilitated nanoparticle sintering and component interconnection procedure," *Nanotechnology*, vol. 21, Nov 2010.

[161] J. Yun, K. Cho, B. Park, H. C. Kang, B.-K. Ju, and S. Kim, "Optical heating of ink-jet printable Ag and Ag-Cu nanoparticles," *Japanese Journal of Applied Physics*, vol. 47, pp. 5070–5075, Jun 2008. 20th International Microprocesses and Nanotechnology Conference, Kyoto, Japan, Nov 05-08, 2007.

[162] J. S. Kang, J. Ryu, H. S. Kim, and H. T. Hahn, "Sintering of inkjet-printed silver nanoparticles at room temperature using intense pulsed light," *Journal of Electronic Materials*, vol. 40, pp. 2268–2277, Nov 2011.

[163] JEDEC Solid State Technology Association, Arlington, *JEDEC Standard. Steady-state temperature humidity bias life test. JESD22-A101B*, 2009.

[164] H. Andersson, A. Manuilskiy, T. Unander, C. Lidenmark, S. Forsberg, and H.-E. Nilsson, "Inkjet printed silver nanoparticle humidity sensor with memory effect on paper," *IEEE Sensors Journal*, vol. 12, Jun 2012.

[165] John R. Vacca, *Computer and Information Security Handbook*. Morgan Kaufmann, second edition ed., 2013.

[166] "Active RFID vs. Passive RFID." http://atlasrfid.com/auto-id-education/active-vs-passive-rfid/. (Last accessed: 2015-03-11).

[167] C. Roberts, "Radio frequency identification (RFID)," *Computers & Security*, vol. 25, pp. 18–26, Feb 2006.

[168] P. Kumar, H. W. Reinitz, J. Simunovic, K. P. Sandeep, and P. D. Franzon, "Overview of RFID technology and its applications in the food industry," *Journal of Food Science*, vol. 74, pp. R101–R106, Oct 2009.

[169] B. Shao, *Fully printed chipless RFID tags towards item-level tracking applications*. PhD thesis, KTH Royal Institute of Technology, 2014.

[170] "Texas Intruments - HF Tags/Inlays/Transponders." http://www.fastrfid.com/hf_tags_texas_instruments.html. (Last accessed: 2015-03-11).

[171] "Alien Higgs3 and Higgs4 Inlay Portfolio (All Alien Inlays)." http://www.rfidconnect.com/ProductDetails.aspx?id=9e95ea50-342d-4a55-adf3-9dac5a99cd7e. (Last accessed: 2015-03-11).

[172] S. Härmä, and V. P. Plessky, *Surface acoustic wave RFID tags*, ch. 8, pp. 145–158. I-Tech Education and Publishing, 2009.

[173] "Surface Acoustic Wave Radio Frequency Identification." http://tentacletech.com/rfid. (Last accessed: 2015-03-11).

[174] B. Bhushan and H. Fuchs, ed., *Applied Scanning Probe Methods VII: Biomimetics and Industrial Applications*. Springer, 2007.

[175] RFSAW Inc., "SAW RFID Tags." http://www.rfsaw.com/Pages/default.aspx. (Last accessed: 2015-03-11).

[176] S. Mukherjee, "Antennas for chipless tags based on remote measurement of complex impedance," in *IEEE European Microwave Conference (EUMC) 2008*, pp. 71–74, Oct 2008.

[177] S. Preradovic and N. Karmakar, "Chipless RFID: bar code of the future," *IEEE Microwave Magazine*, vol. 11, pp. 87–97, Dec 2010.

[178] V. Subramanian, P. Chang, J. Lee, S. Molesa, and S. Volkman, "Printed organic transistors for ultra-low-cost RFID applications," *IEEE Transactions on Components and Packaging Technologies*, vol. 28, pp. 742–747, Dec 2005.

[179] M. Jung, J. Kim, J. Noh, N. Lim, C. Lim, G. Lee, J. Kim, H. Kang, K. Jung, A. Leonard, J. Tour, and G. Cho, "All-printed and roll-to-roll-printable 13.56-MHz-operated 1-bit RF tag on plastic foils," *IEEE Transactions on Electron Devices*, vol. 57, pp. 571–580, Mar 2010.

[180] I. S. Miodrag Bolic, David Simplot-Ryl, ed., *RFID Systems: Research Trends and Challenges*. John Wiley and Sons, Jul 2010.

[181] S. Mukherjee, "Chipless radio frequency identification by remote measurement of complex impedance," in *IEEE European Microwave Conference (EUMC) 2007*, pp. 1007–1010, Oct 2007.

[182] C. Mandel, M. Schübler, M. Maasch, and R. Jakoby, "A novel passive phase modulator based on LH delay lines for chipless microwave RFID applications," in *IEEE MTT-S International Microwave Workshop on Wireless Sensing, Local Positioning, and RFID, 2009 (IMWS 2009)* , pp. 1–4, Sep 2009.

[183] I. Balbin and N. Karmakar, "Phase-encoded chipless RFID transponder for large-scale low-cost applications," *IEEE Microwave and Wireless Components Letters*, vol. 19, pp. 509–511, Aug 2009.

[184] A. Chamarti and K. Varahramyan, "Transmission delay line based ID generation circuit for RFID applications," *IEEE Microwave and Wireless Components Letters*, vol. 16, pp. 588–590, Nov 2006.

[185] J. Vemagiri, A. Chamarti, M. Agarwal, and K. Varahramyan, "Transmission line delay-based radio frequency identification (RFID) tag," *Microwave and Optical Technology Letters*, vol. 49, pp. 1900–1904, Aug 2007.

[186] L. Zheng, S. Rodriguez, L. Zhang, B. Shao, L.-R. Zheng, "Design and implementation of a fully reconfigurable chipless RFID tag using inkjet printing technology," in *Proceedings of 2008 IEEE International Symposium on Circuits and Systems*, pp. 1524–1527, 2008.

[187] I. Jalaly and I. Robertson, "Capacitively-tuned split microstrip resonators for RFID barcodes," in *IEEE European Microwave Conference (EuMC) 2005* , vol. 2, pp. 4 pp.–, Oct 2005.

[188] J. McVay, A. Hoorfar, and N. Engheta, "Space-filling curve RFID tags," in *IEEE Radio and Wireless Symposium 2006*, pp. 199–202, Jan 2006.

[189] A. Vena, E. Perret, and S. Tedjini, "RFID chipless tag based on multiple phase shifters," in *2011 IEEE MTT-S International Microwave Symposium Digest (MTT)*, pp. 1–4, Jun 2011.

[190] A. Vena, E. Perret, S. Tedjini, G. Tourtollet, A. Delattre, F. Garet, and Y. Boutant, "Design of chipless RFID tags printed on paper by flexography," *IEEE Transactions on Antennas and Propagation*, vol. 61, pp. 5868–5877, Dec 2013.

[191] I. Balbin and N. Karmakar, "Novel chipless RFID tag for conveyor belt tracking using multi-resonant dipole antenna," in *IEEE European Microwave Conference (EuMC) 2009*, pp. 1109–1112, Sep-Oct 2009.

[192] S. Preradovic, I. Balbin, N. Karmakar, and G. Swiegers, "Multiresonator-Based Chipless RFID System for Low-Cost Item Tracking," *IEEE Transactions on Microwave Theory and Techniques*, vol. 57, pp. 1411–1419, May 2009.

[193] H.-S. Jang, W.-G. Lim, K.-S. Oh, S.-M. Moon, and J.-W. Yu, "Design of lowsost chipless system using printable chipless tag with electromagnetic code," *IEEE Microwave and Wireless Components Letters*, vol. 20, pp. 640–642, Nov 2010.

[194] B. Shao, Q. Chen, R. Liu, and L.-R. Zheng, "Design of fully printable and configurable chipless RFID tag on flexible substrate," *Microwave and Optical Technology Letters*, vol. 54, pp. 226–230, Jan 2012.

[195] B. Shao, Y. Amin, Q. Chen, R. Liu, and L.-R. Zheng, "Directly printed packaging-paper-based chipless RFID tag with coplanar LC resonator," *IEEE Antennas and Wireless Propagation Letters*, vol. 12, pp. 325–328, 2013.

[196] T. Unander, J. Sidén, and H.-E. Nilsson, "Designing of RFID-based sensor solution for packaging surveillance applications," *IEEE Sensors Journal*, vol. 11, pp. 3009–3018, Nov 2011.

[197] S. Manzari, C. Occhiuzzi, S. Nawale, A. Catini, C. Di Natale, and G. Marrocco, "Humidity sensing by polymer-loaded UHF RFID antennas," *IEEE Sensors Journal*, vol. 12, pp. 2851–2858, Sep 2012.

[198] J. Yin, J. Yi, M. Law, Y. Ling, M. C. Lee, K. P. Ng, B. Gao, H. Luong, A. Bermak, M. Chan, W.-H. Ki, C. ying Tsui, and M. Yuen, "A system-on-chip EPC Gen-2 passive UHF RFID tag with embedded temperature sensor," *IEEE Journal of Solid-State Circuits*, vol. 45, pp. 2404–2420, Nov 2010.

[199] L. Catarinucci, R. Colella, and L. Tarricone, "Enhanced UHF RFID sensor-tag," *IEEE Microwave and Wireless Components Letters*, vol. 23, pp. 49–51, Jan 2013.

[200] B. S. Cook, J. R. Cooper, and M. M. Tentzeris, "An inkjet-printed microfluidic RFID-enabled platform for wireless lab-on-chip applications," *IEEE Transactions on Microwave Theory and Techniques*, vol. 61, pp. 4714–4723, Dec 2013.

[201] R. A. Potyrallo and W. G. Morris, "Multianalyte chemical identification and quantitation using a single radio frequency identification sensor," *Analytical Chemistry*, vol. 79, pp. 45–51, Jan 2007.

[202] C. Occhiuzzi, A. Rida, G. Marrocco, and M. Tentzeris, "RFID passive gas sensor integrating carbon nanotubes," *IEEE Transactions on Microwave Theory and Techniques*, vol. 59, pp. 2674–2684, Oct 2011.

[203] A. Kang, C. Zhang, X. Ji, T. Han, R. Li, and X. Li, "SAW-RFID enabled temperature sensor," *Sensors and Actuators A-Physical*, vol. 201, pp. 105–113, Oct 2013.

[204] C. Hartmann, P. Hartmann, P. Brown, J. Bellamy, L. Claiborne, and W. Bonner, "Anti-collision methods for global SAW RFID tag systems," in *2004 IEEE Ultrasonics Symposium*, vol. 1-3, pp. 805–808, 2004.

[205] R.-E. Azim and N. Karmakar, "A collision avoidance methodology for chipless RFID tags," in *2011 Asia-Pacific Microwave Conference Proceedings (APMC)*, pp. 1514–1517, Dec 2011.

[206] A. Vena, E. Perret, S. Tedjini, D. Kaddour, A. Potie, and T. Barron, "A compact chipless RFID tag with environment sensing capability," in *2012 IEEE MTT-S International Microwave Symposium Digest (MTT)*, pp. 1–3, Jun 2012.

[207] A. Vena, L. Sydänheimo, M. Tentzeris, and L. Ukkonen, "A fully inkjet-printed wireless and chipless sensor for CO_2 and temperature detection," *IEEE Sensors Journal*, vol. 15, pp. 89–99, Jan 2015.

[208] S. Shrestha, M. Balachandran, M. Agarwal, V. V. Phoha, and K. Varahramyan, "A chipless RFID sensor system for cyber centric monitoring applications," *IEEE Transactions on Microwave Theory and Techniques*, vol. 57, pp. 1303–1309, May 2009.

[209] D. Girbau, A. Ramos, A. Lázaro, S. Rima, and R. Villarino, "Passive wireless temperature sensor based on time-coded UWB chipless RFID tags," *IEEE Transactions on Microwave Theory and Techniques*, vol. 60, pp. 3623–3632, Nov 2012.

[210] R. S. Nair, E. Perret, S. Tedjini, and T. Baron, "A group-delay-based chipless RFID humidity tag sensor using silicon nanowires," *IEEE Antennas and Wireless Propagation Letters*, vol. 12, pp. 729–732, 2013.

[211] E. M. Amin, M. S. Bhuiyan, N. C. Karmakar, and B. Winther-Jensen, "Development of a low cost printable chipless RFID humidity sensor," *IEEE Sensors Journal*, vol. 14, pp. 140–149, Jan 2014.

[212] P. V. Nikitin and K. V. S. Rao, "Theory and measurement of backscattering from RFID tags," *IEEE Antennas and Wireless Propagation Letters*, vol. 48, pp. 212–218, Dec 2006.

[213] W.-T. Wang, Y. Liu, S.-X. Gong, Y.-J. Zhang, and X. Wang, "Calculation of antenna mode scattering based on methods of moments," *Progress in Electromagnetics Research Letters*, vol. 15, pp. 117–126, 2010.

[214] D. Dardari, F. Guidi, C. Roblin, and A. Sibille, "Ultra-wide bandwidth backscatter modulation: processing schemes and performance," *EURASIP Journal of Wireless Communications and Networking*, vol. 2011:47, Jul 2011.

[215] A. Ramos, A. Lazaro, D. Girbau, and R. Villarino, "Time-domain measurement of time-coded UWB chipless RFID tags," *Progress in Electromagnetics Research - PIER*, vol. 116, pp. 313–331, 2011.

[216] R. E. Collin, *Foundations for Microwave Engineering*. IEEE Presss Series on Electromagnetic Wave Theory, John Wiley and Sons, 2001.

[217] Y. Feng, M. Müeller, J. Liebeskind, Q. Chen, L.-R. Zheng, W. Schimidt, W. Zapka, "Characterization of inkjet printed coplanar waveguides for flexible electronics," in *Proceedings of Digital Fabrication 2011*, pp. 454–457, Oct 2011.